Study of the Influence of the Plasma Torch in a Plasma Arc Melting Furnace

by

Helen Holst

A thesis submitted to the Faculty of Engineering of the University of Birmingham, for the degree of Master of Science by Research

Interdisciplinary Research Centre in
Materials for High Performance Applications
University of Birmingham
Birmingham, B15 2TT
England
30th September 2014

Synopsis

Plasma arc melting, PAM, is used to melt and refine titanium, a reactive alloy often used in the aerospace industry. This thesis looks at the effect of the properties of a plasma torch within PAM, focusing on its use as a mechanism for inputting energy to the ingot. Previous research has failed to address the relationship between a plasma torch and titanium during a refining process; choosing to focus on the two separately e.g. the use of plasma in welding or refining using Vacuum Arc Remelting, VAR. Different aspects of the plasma torch in PAM have been examined. In particular how much thermal and electrical energy is inputted and lost from the torch, and how the effect this has on the energy flow in the ingot being melted. To do this number of experiments were carried out measuring the energy outputs: visual methods (examining the growth of melt pools); voltage measurements to quantify energy flow in the ingot; and thermocouples attempting to measure the radiation energy given off by the plasma. This work provides an insight into the effect of the plasma, by highlighting and quantifying a number of factors that influence the efficiency of the torch.

Acknowledgements

Most of all I would like to thank my supervisor Dr Mark Ward for his consistent help, support and sharing of knowledge. In addition I would like to thank my industrial supervisors and contacts at TIMET, Nicholas Winter, Matthew Thomas, Roger Thomas and Ashish Patel, who have always been there to offer support and feedback on the work.

For the practical help I would like to acknowledge Tim Perry at the University of Birmingham for his help with the button furnace and unending patience during countless repeats. As well as Richard Welch and the team of technicians at TIMET, without which none of the plasma experiments would have been possible. Finally it is necessary to recognise help from my fellow students and research fellows who were always willing to pass on knowledge they had learnt.

Table of Contents

List of Figures

List of Tables

List of Symbols

Symbol	Description	Unit
α	Thermal Expansion Coefficient	K^{-1}
a	Melt Pool Radius	m^2
A	Area	m^2
A_c	Area of Cold surface	m^2
A_H	Area of Hot Surface	m^2
A_L	Area of Liquid	m^2
A_P	Area of Plume	m^2
A_T	Area of the Target	m^2
$\underline{B}$	Magnetic Field	T (NA^{-1})
c	Calculated Melt Pool Area	m^2
C	Constants for the Target	
Cp	Specific Heat Capacity	$Jkg^{-1}K^{-1}$
dr	Change in radius	m
dT/dt	Rate of change of temperature	Ks^{-1}
ΔT	Change in Temperature	K
ε_c	Emissivity of the Cold Object	
ε_F	Emissivity of the Furnace	
ε_H	Emissivity of the Hot Object	
ε_{SK}	Emissivity of the skull	
ε_P	Emissivity of the plume	
ε_T	Emissivity of the target	
E	Voltage gradient vertically along the plasma arc	Vm^{-1}
E_{INPUT}	Energy input to the melt pool	J
%EL	Room Temperature Ductility (Percentage Elongation)	%
EPUL	Energy per Unit Length	Jmm^{-1}
$\underline{F}$	Lorentz Force	Nm^{-3}
$F_{A\rightarrow B}$	View Factor between object A and B	
$F_{F\rightarrow T}$	Radiation View Factor between the Furnace and the Target	
η	Torch Efficiency	%
η_R	Radiation Efficiency	%
H	Height of Plume	m
h	Depth of Melt Pool	m
I	Torch current	A
J	Current Density	Am^{-2}
$\underline{J}$	Current Density Vector	Am^{-2}
K	Thermal Conductivity	$Wm^{-1}K^{-1}$
k_E	Turbulent Kinetic Energy	J
K_E	Mean Kinetic Energy	J

L_a	Arc Length	m
L_{Re}	Length through which the fluid flows	m
ℓ	Depth	m
m	Mass	kg
m_t	Mass of Thermocouple	Kg\A
P	Torch power	W
P_o	Net Power received by the Work Piece	W
P_r	Radiation Power per unit length	Wm^{-1}
P_R	Radiation Power	W
P_{rd}	Radiation Power Density	Wm^{-2}
Q	Rate of Heat Energy Transfer	W
Q'	Heat Flux	Wm^{-2}
r, r_1, r_2	Radii	m
r_p	Radius of Plume	m
ρ_e	Electrical Resistivity	Ωm
ρ	Density	Kgm^{-3}
ρ_{RT}	Thermal Resistivity	$W^{-1}mK$
R	Resistance	Ω
Re	Reynolds Number	KW^{-1}
R_{LHE}	Thermal resistance between liquid and hearth	KW^{-1}
R_{LSk}	Thermal Resistance between liquid and skull	KW^{-1}
R_{SKL}	Thermal Resistance between skull and liquid	KW^{-1}
R_{PL}	Thermal Resistance between plume and liquid	KW^{-1}
R_T	Thermal Resistance	KW^{-1}
σ	Stephan-Boltzmann constant	s
t	Time	s
T	Temperature	K
T_A	Temperature of object A	K
T_{Atmos}	Temperature of the atmosphere	K
T_B	Temperature of object B	K
T_C	Temperature a relatively low temperature object	K
T_F	Temperature of the Furnace	K
T_H	Temperature a relatively high temperature object	K
T_h	Temperature of the heavy particles in plasma	K
T_{HE}	Temperature of the Hearth	K
T_L	Liquid Temperature	K
T_{liq}	Liquidus Temperature	K
T_m	Melting Temperature	K
T_0	Starting Temperature	K
T_P	Temperature of Plume	K
T_S	Solid Temperature	K
T_{SK}	Temperature of the skull	K
T_{sol}	Solidus Temperature	Pas^{-1}

υ	Viscosity	$kgm^{-1}s^{-1}$
v	Mean velocity in respect to fluid	ms^{-1}
V	Voltage	V
V_a	Arc Voltage	V
Vf	Fall Voltage at the anode and cathode	V
Vol	Volume of the Melt Pool	m^3
x	Measurement of Distance	m
X	Cross Product	m^2
x_{dt}	Distance between the target and front of the tube	m
X	Corrected Melt Pool Area	A
y	Difference in Current (Expected - Actual)	

1) Introduction

Over the years, air transport is being used less as a luxury and more as a commodity. The number of people flying has increased dramatically [3] (airbus forecasts a further 109% increase on passenger aircraft alone over the next 30 years [4]) forcing the aerospace industry to produce larger and more efficient planes. However there have been some obstacles to this expansion along the way that have attracted particular media interest [5]. One of note for this thesis is the Sioux City disaster that can be linked to a defect in the fan containment ring [5]. It is the removal of such defects, amongst others, that has provided a constant drive to produce clean, homogeneous aerospace materials at a reasonable price. In response to this, titanium producers such as TIMET have heavily invested time and money into optimising processing techniques, such as PAM (Plasma Arc Melting). TIMET has worked alongside the aerospace industry for many years, stating that an integral reason for its founding as a titanium manufacture, was to support the Military's drive to produce high performance materials [6].

1.1 Background of Refining

Research into PAM has died down in the last 10 years and other processes, such as Vacuum Arc Remelting (VAR), are being used more commonly. For example, in 2005 the US produced 80% of its ingots by VAR [7]. This is despite cold hearth processes being considered cheaper than VAR (due to its advantages in the recycling of scrap and because the electrode is formed in situ so no prior processing is required [7]) and better at maintaining a constant alloy composition (due to lower pressures in the furnace, which decease evaporation of elements and segregation).

VAR is favoured as it is qualified for use in aerospace applications (an expensive process that can take 5-10 years). Therefore to close this gap, industry has made moves towards qualifying PAM by increasing the understanding of the process. Once this has been achieved, it is expected there will be an increased demand for PAM refined materials. In the meantime, PAM ingots can be used as a feedstock for VAR. Additionally, with more sensitive alloy compositions being required, there is a final economical driving force for the optimization of PAM.

1.2 Materials

For manufacturing there is space for a competitor to the commonly used Nickel Based super alloys used in the high temperature parts or components of aircraft engines. Gamma titanium aluminides, γ-TiAl, have for years been regarded as a worthy intermetallic replacement, with comparable properties but a lower density allowing weight reduction and thus financial savings. Although the pros and cons of this material will be discussed in more detail in the main section of this work, it is necessary to note at this stage that processing of γ-TiAl can be difficult, but it is thought that PAM could overcome some of the problems encountered. However, introducing new techniques and materials into such a safety critical market is difficult. In 1991 M.I.Boulos [8] stated that 'in order for plasma to make significant commercial inroads it must have significant, demonstrable, metallurgical and/or cost advantages over existing technology.'

1.3 Properties of PAM

The research in this thesis concentrates on the Plasma Arc Cold Hearth as a method of refining titanium alloys. PAM is a method used to decrease the number (below 1 per $5x10^5$kg) and size of inclusions whilst improving the homogeneity of the alloy. The aim

of this process is therefore to result in materials that have uniform properties and low probabilities of initiating cracks.

1.3.1 Furnace

The plasma arc furnace is made up of two main parts, the hearth and the crucible, shown in Figure 1.1 and Figure 5.4. These are contained in an inert atmosphere, which can be argon, helium or a mixture of both (dependent on the market price at any given time). The oxygen content is maintained at a level of <10 ppm to ensure low oxygen levels in the final ingot. Unlike in VAR, feedstock for the furnace is prepared in situ. The amount of each element needed to make up the feedstock is dispensed, weighed according to the composition specified by the customer (using a combination of scrap and master alloy). This feedstock can then be formed into compacts for ease of melting or melted in the hearth.

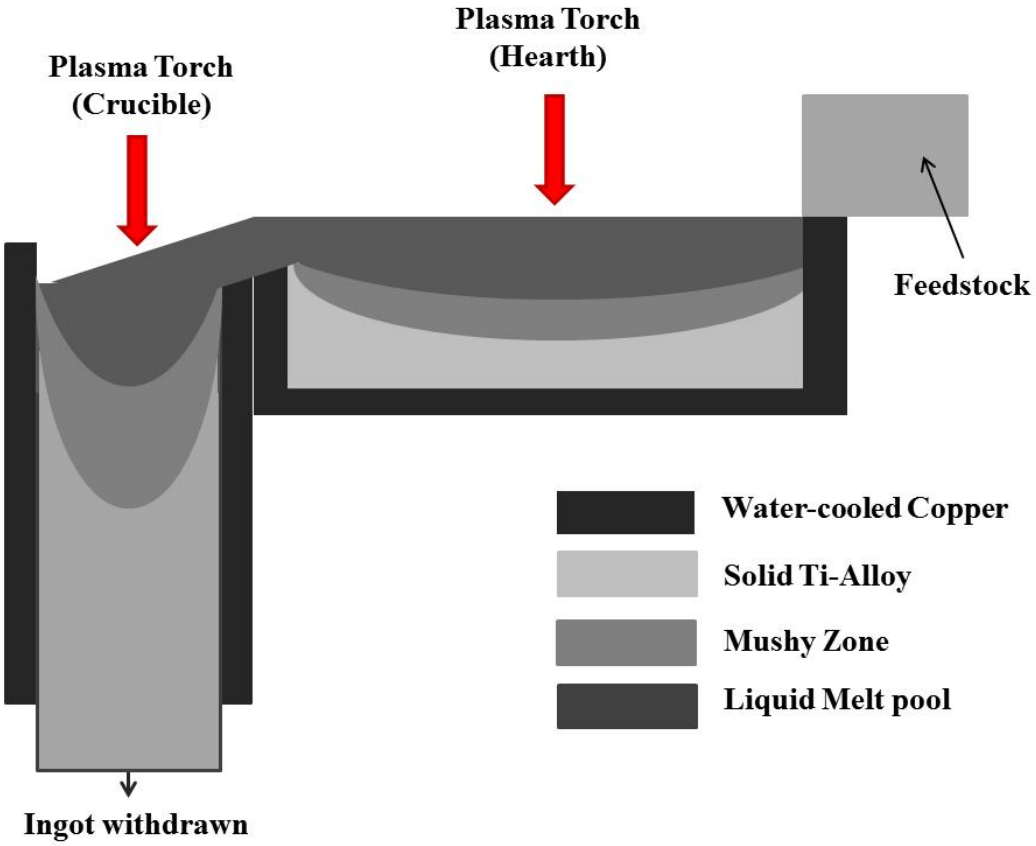

Figure 1.1: Schematic of a typical, single hearth, PAM set-up

1.3.2 Hearth

Once the feedstock has been pushed into the hearth, the torch parameters (e.g. Torch Current, Gas Flow Rate and Arc Length) are set and applied. Once the liquidus temperature is reached locally, a melt pool starts to form. Due to the superheat under the torch, melt pools grow radially outward from the torch centre. The hearth is made out of copper (for its high thermal conductivity) and is water-cooled. This ensures that a solid skull of the titanium alloy is maintained, separating the high temperature liquid from the hearth [9]. Within the melt pool, in both the hearth and crucible, multiple processes occur, (e.g. fluid flow, dissolution of inclusions) and the consequence of these can be seen in the homogeneity and number of inclusions. The heath torch is moved in a set pattern, to ensure all the metal is liquid before it flows into the crucible.

1.3.3 Crucible

Within the copper cooled crucible the liquid metal is solidified and is withdrawn to form ingots (commonly cylindrical in shape). The crucible has a secondary torch, identical to the hearth torch, placed at the top of the crucible to maintain a melt pool and ensure the centre of the ingot does not fully solidify before it is withdrawn. The main variables at this stage are the torch parameters (discussed in detail later) and the withdrawal rate.

1.3.4 Residence Time

For any refining process, one of the main aims is to ensure that the inclusions in the melt pool have sufficient time to be removed. For PAM this is done by controlling the residence time and temperature of the inclusions in the hearth. These depend on the volume of liquid metal, its temperature distribution and the nature of the velocity of the flow. Ideally, a large percentage of the feedstock will be above the liquidus temperature. This decreases the

residence time needed for the inclusions to melt and therefore provides economic savings by decreasing the melt time.

For this reason the methods of studying PAM, with reference to the residence time, were explored here with examples of how experiments and numerical models can be used to analyse the process. The aim was to investigate the potential advantages and limitations of certain techniques, such as visual and sensor trials used to evaluate the different aspects of refining in the PAM hearth. It should be noted that the work here focuses on the hearth, although processes in the crucible will be touched upon for comparison and completeness.

1.4 Example Melt

There are only a few companies that manufacture PAM furnaces, resulting in limited number of designs. However, a plasma furnace has a number of operating variables, and it is these variables that are normally optimized to improve ingot quality further once the furnace has been installed. An example of this is how the PAM furnace was run at the IRC in the University of Birmingham. As mentioned, due to the reactive nature of titanium an inert atmosphere is used in the furnace. This is achieved by evacuating the furnace to a pressure <4 Pa and back filling it with argon to a pressure of 110 kPa. As maintaining the atmosphere is important during this process, the chamber leak rate is monitored and any leaks must be dealt with immediately. Like any process that relies on a controlled atmosphere, this can lead to delays or ingots that do not meet specification, so good maintenance of equipment is vital.

The next step in a melt is to form a ‘skull’ of the alloy being melted between the liquid metal and the copper hearth. One skull can be used for the production of multiple ingots of the same alloy. In this case the hearth is cuboid in shape, with inside dimensions that are approximately 25x20x20 mm and walls 20 mm thick. Both the hearth and crucible torches are moved by hydraulics and can therefore be slow, this can result in sections of the

feedstock solidifying after being melted whilst the torch is being moved. Once a compact is melted, half of the liquid metal is allowed to spill over into the crucible before the other half is melted further, to ensure enough residence time is given. During a full melt, over 24 compacts are processed in order to create a final ingot of satisfactory size. Therefore a single melt can take somewhere between 4 and 6 hours.

1.5 Differences between Furnace Designs

The relatively small furnace discussed above (approximately 1m in diameter producing ingots of up to 70kg) will be used for the melt pool experiments described here. However, in most cases industry makes ingots of a higher weight (7-9 tonnes). Larger scale melts can vary from that described in a few ways. One example is the use of multiple hearths. These increase the residence time of the liquid and allow for a more continuous process to be achieved, as multiple feedstock can be melted at one time. The dimensions of the hearth can vary for different furnaces, both in terms of size and shape, and this can have an effect on the heat and fluid flow within the hearth.

The torch power is also varied depending on the amount of feedstock that needs to be melted in each batch. The torch power for the experiments described in this thesis was 100 kW (200 V and 500A). However, depending on the torch used, it can vary from 75 kW to 3000 kW [10]. Multiple torches are used in some furnaces to increase the input power. A few sources suggest that in the early 1990s a typical set-up would consist of four torches, which can be used with a combined power of 2-3MW[11, 12].

2) Literature Review

2.1 Heat transfer in a plasma furnace

For this work the area that lies within the plasma torch and skull, highlighted by the dotted black line in Figure 2.1, is of most importance. There are a number of heat transfer processes that occur in this region. The ultimate aim of a plasma furnace is for as much thermal energy to remain in the skull and melt pool as possible, producing a melt pool with an adequate size and temperature.

The power input for a furnace in general is limited only by how much power can be safely removed from the hearth/crucible by water cooling. Due to this, smaller furnaces have to use lower torch powers, whilst still effectively removing inclusions. Therefore the residence time must be balanced with the torch power.

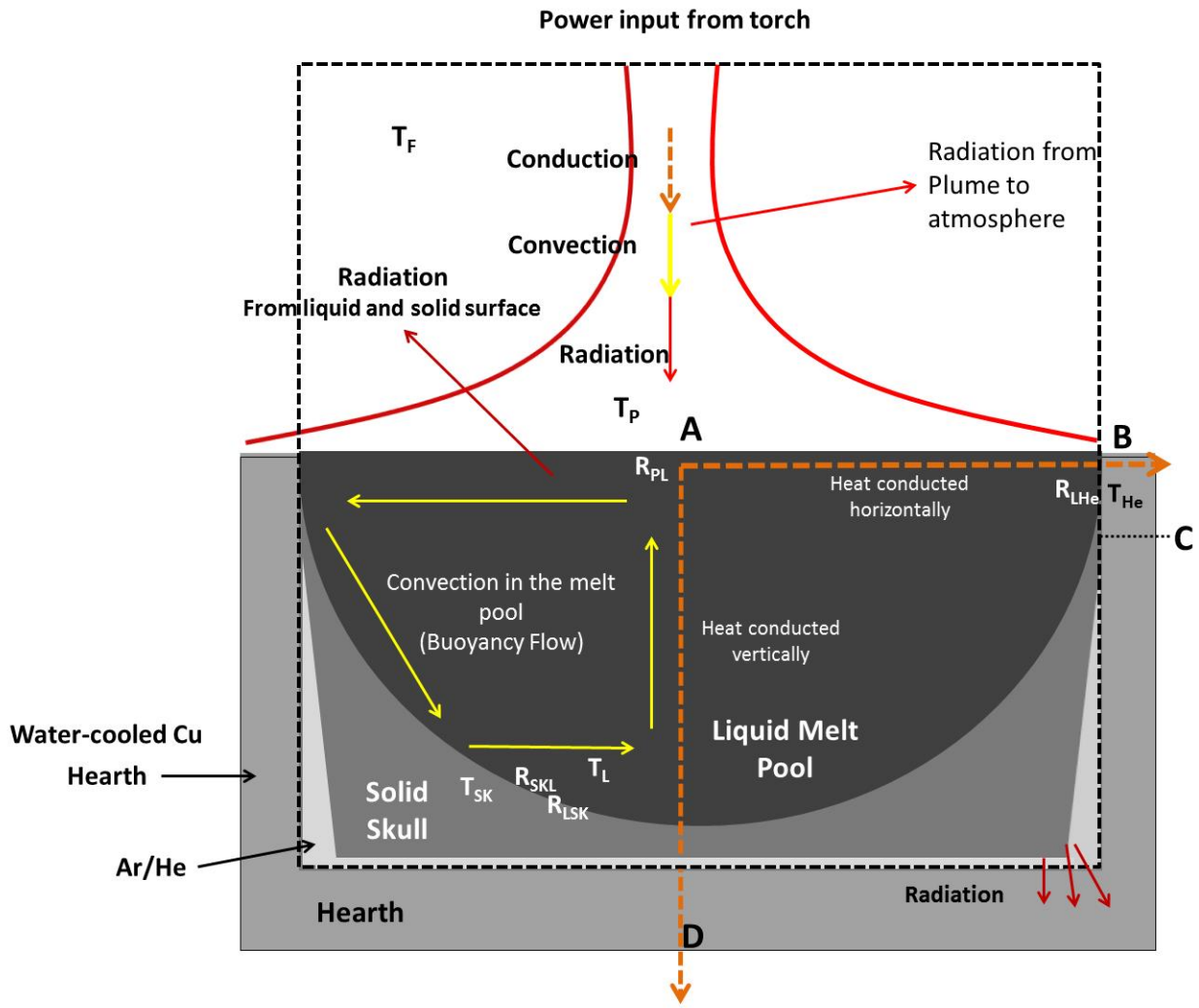

Figure 2.1: Heat transfer between the plasma plume, melt pool, skull and hearth

2.1.1 Summary of Heat Transfer processes

$$Q = \frac{\Delta T}{R_T} = \frac{T_L - T_{SK}}{R_{LSK}} \qquad \textbf{Equation 2.1}$$

Where ΔT refers to the difference in temperature between the liquid and solid (K) and R_T is the thermal resistance of the skull (K/W).

Heat energy is further lost from the skull both by radiation and conduction through the Ar gas trapped between the skull and the hearth, and from conduction directly from the skull to the outside atmosphere through the hearth. It should be noted that Figure 2.1 shows contact between the skull and hearth only at the top of the hearth however, as described later in the

sensors experiment discussion, points of contact can be found along the surface due to the rough skull surface.

The radiation can be represented by the Stefan-Boltzmann Law:

$$\boldsymbol{Pr = A(T_H{}^4 - T_C{}^4)\varepsilon\sigma} \qquad \textbf{Equation 2.2}$$

Where Pr is the radiation power, A is the area over which heat is radiated, T_H and T_C are the temperature of the hotter and cooler object respectively, ε is the emissivity of the object emitting the radiation and σ is the Stefan-Bolzmann constant.

Note for objects where $T_H >> T_C$ radiation only needs to be considered in one direction; however when $T_H => T_C$ radiation must be considered in both directions and Equation 2.2 becomes:

$$\boldsymbol{Pr = A_H(T_H{}^4 - T_C{}^4)\varepsilon_H\,\sigma + A_C(T_C{}^4 - T_H{}^4)\varepsilon_C\,\sigma} \qquad \textbf{Equation 2.3}$$

Where A_H and A_C are the radiation for the hotter and cooler objects respectively and $\varepsilon_{H \text{ and }} \varepsilon_C$ are the emissivity of the hotter and cooler objects respectively. These radiation equations are simplified and normally will contain a view factor; this is a concept that will be expanded on in a later section.

For the purpose of this explanation accumulation will be assumed to be the energy used for fluid flow and dissolution of inclusions, E (although some energy will cause the temperature of the skull to rise). In addition to this the melt pool; the skull, atmosphere and plume are assumed to have no variation in their temperature. The temperature of the plume, Tp is assumed to be much greater than the temperature of the solid, T_S and liquid, T_L, metal.

For the melt pool the Heat Energy Balance is as follows:

- **Input**

Conduction into the liquid from plume and solid skull, and radiation into the liquid from the plume:

$$\frac{T_P - T_L}{R_{PL}} + \frac{T_{Sk} - T_L}{R_{SKL}} + A_P {T_P}^4 \varepsilon_P \sigma \qquad \textbf{Equation 2.4}$$

Where T_P is the temperature of the plume, ε_P is the emissivity of the plume and A_p is the area of the plume.

- **Output**

Conduction from liquid into the skull and hearth, and radiation from its surface:

$$\frac{T_L - T_{He}}{R_{LHe}} + \frac{T_L - T_{SK}}{R_{LSK}} + \mathbf{A_L}(\mathbf{T_L}^4 - \mathbf{T_F}^4)\boldsymbol{\varepsilon_L}\,\boldsymbol{\sigma} \qquad \textbf{Equation 2.5}$$

Where T_{SK} is the temperature of the skull and T_F is the temerature of the Furnace

From Equation 2.5 it can be seen that by increasing the resistance between the melt pool and the hearth, the output from the melt pool can be reduced. As this resistance is a combination of the resistance between the melt pool and the skull, and the skull and the hearth, increasing the latter can reduce the output. This comment was also made by R.M.Ward [13], who observed that in order to increase the volume of liquid produced during melting (i.e. the volume of the melt pool), the resistance between the skull and the hearth must also increase.

Some of the parameters that make up the thermal input and output from a liquid melt pool will be governed by the type of furnace being used, although in addition to the variables

that differ between furnaces there are those that can be varied for each melt. It is these variables that may be optimized to increase efficiency and quality of the refining process.

2.2 Variables that effect Thermal Energy Input

2.2.1 Torch Power

The heat input into the metal is controlled during the melt by the torch parameters that have been set, such as the movement, plasma gas used, arc length and power of the torch. The torch power can have an effect on melting in the hearth and in general has a positive linear relationship with melt pool growth. Although each torch is limited there are a range of powers that are possible. For instance the current for the particular hearth torch can range from 300 to 700 A, changing the power input from the torch. Assuming a voltage of 200 V, this gives a range of torch power from 60 kW to 140 kW.

2.2.2 Insulation

Heat transfer via conduction can be reduced by introducing an insulating layer (i.e. increasing the resistance between the skull and the hearth). R.M.Ward [13] looked into the effect of two different types of insulation (crushed swarf and K-wool ceramic) on the melt pool shape in a crucible. This was carried out by placing the insulation all around the ingot being melted, both on the bottom and sides. It was found that the more insulating K-wool ceramic produced a larger melt pool. This was shown as the beta transus and melt point lines, shown by changes in microstructure (a method discussed later in the Results section) were further from the top of the crucible.

2.2.3 Torch Pattern

The automated pattern used currently follows a ‘Raster’ pattern along the surface of the metal i.e. the torch passed back and forth across the surface. Xia Xu, Hui Chang et al [14] modelled a torch pattern that consisted of one diagonal line across the hearth. The results found may give an idea of the effect of one line in the Raster pattern. They note that as the scanning frequency is decreased (from 0.25 Hz to 0.0833 Hz) the temperature gradients were seen to be larger and a higher melt temperature is achieved (approximately 2025 K at 0.0833 Hz and 1975K at 0.5 Hz). Although this does not take into consideration the effect of parallel lines on one another it does indicate the effect of the torch pattern can be fairly significant. There will not be sufficient time to fully investigate the effect of the torch pattern and for this work the torch will be assumed to be static. In the Torch pattern section of this thesis the ways in which the torch pattern can effect mixing and homogenisation is discussed further.

2.2.4 Water Flow Rate

Blackburn [12]suggests that using a copper water cooled hearth can lead to water leaks and contamination. The solid skull formed between the molten metal goes some way to prevent this from occurring, however regular maintenance of the hearth is required and problems with the cooling systems can lead to delays in production. The water flow rate within the hearth is a further parameter that needs to be monitored and can be varied. Problems occur if it is not high enough as the copper can become overheated, thereby leading to contamination, but also if it is too high as this transfers heat away from the skull and hence the melt pool.

2.3 Comparison of refining processes

2.3.1 Vacuum Arc Remelting, VAR

VAR is a common process for refining titanium and is used extensively by TIMET [6]. It is capable of making ingots of varying sizes (Consarc [15] claim that there VAR furnaces make ingots between 610 and 1075 mm in diameter).

It utilizes a consumable electrode as its feedstock through which current is passed forming an electric arc between itself and the mould. The heat generated from this arc causes the electrode to start melting. To achieve this, the furnaces at TIMET have a power input of approximately 400 kW. Over time the liquid metal drops down into the copper cooled mould and solidifies to into a cylindrical ingot. The melt rate is controlled by maintaining a given arc gap between the electrode and the melt pool by moving the ingot down as the melt continues. On average this process is repeated three times before the number and size of impurities meets the standard for the aerospace industry ($1/5x10^5$kg [16])

The set-up in VAR acts in many ways like the crucible section of a PAM furnace where the ingot solidifies in a vertical set up. However many of the advantages of PAM over VAR are linked to the horizontal copper cooled hearth [17]. It allows high density inclusions to be removed, trapping them in the mushy zone [17]. In addition the consumable electrode in VAR must be self-supporting and have a diameter smaller than the mould unlike PAM where a variety of feedstock geometries can be used. PAM has one further advantage over VAR as the melt rate and the torch power can be controlled separately for the cold hearth processes [18] making longer residence times possible at high temperatures.

2.3.2 Electron Beam Cold Hearth Remelting, EBCHR

EBCHR uses a horizontal copper water-cooled hearth like PAM however has an alternative heat input method. Free electrons within a vacuum are focused into a beam using

electric and magnetic fields. The vacuum causes a negative pressure (i.e. below atmospheric) in the furnace and as a consequence Al volatilization is seen more readily [9, 17]. This can result in an inhomogeneous distribution of alloying elements across the ingot [17].

2.3.3 Limitations of PAM

Despite these benefits PAM still does have limitations, for instance both VAR [12, 13, 19] and EBCHR [20] are thought to produce ingots with better surface qualities. This is linked to the slow moving torch in PAM giving time for the liquid metal in contact with the copper cooled crucible to solidify resulting in laps [12]. As a result Blackburn (1993) suggests that combinations of VAR and PAM/EBCHR are more commonly used to give a low number of inclusions and a good surface quality, homogeneity and microstructure [20, 21]. However it is apparent that by addressing these limitations it may be possible to use PAM on its own, giving economic and time savings.

2.3.4 Extent of research on PAM, VAR and EBCHR

PAM was fairly widely documented in the 90s [8, 13, 22, 23] although the publication of research in the subject has slowed down in the last 10 years. However research has continued on other refining processes such as VAR [23-30] and EBCHR [17, 18, 31, 32], as well as other processes, less commonly used on titanium alloys (for instance Electro-slag Remelting, ESR and Induction melting).

The melt pool in VAR has been modelled using a variety of finite difference and element models that consider laminar and turbulent fluid flow [7, 29, 33], producing fairly comparable results. In addition to this work by P.A.Davison, X.He, and A.J.Lowe [29] , R.M.Ward and B.Nair [30] and others highlight the effects of outside inductors causing a secondary vertical magnetic field [25]. This is a phenomenon that is not as relevant to work on PAM as the process is self-contained and the currents needed are less. However research

carried out on the relationship between competing buoyancy and Lorentz forces are comparable to those seen in the melt pool, both in the hearth and crucible. In addition to this, at this stage, VAR has taken further steps than PAM to being an automated system, in which the production of ingots are controlled more by sensors than by the controller[34]. Methods have been implemented to monitor parameters such as arc gap control (the distance between the bottom of the electrode and the melt pool) to some degree of success [35].

Research into EBCHR is not as detailed at this stage as with VAR, however it has still been fairly widely studied. As with VAR, fluid flow has been studied by numerous researchers. They have found that due to the large temperature gradients at the point in which the electron beam comes into contact with the melt pool, Marangoni flow is the main source of fluid flow for EBCHR [36, 37]. This is different to the flow regimes in VAR and PAM where the arcs cause Lorentz force, and as discussed above most of the research mirrors this and often ignores the influence of Marangoni flow. A. Mitchell [36] suggests that modelling of PAM process is more complicated than EBCHR due to the interaction of the plasma plume with the melt pool and the resultant Lorentz forces. In some ways this makes models of fluid flow in VAR more applicable than research on EBCHR. However A.Mitchell [36] goes on to state that the particle removal efficiency may still be similar. This is likely to be the case due to the horizontal hearth used for both EBCHR and PAM.

2.4 Torch Properties

Blackburn[12] indicates that the residence time is influenced by the molten pool weight and the melt rate. He goes on to link this to four parameters controlled by the torch power: arc length, torch pattern and the thermal input to the hearth i.e. the thermal energy transferred from the plasma gas. Further to this the gas flow rate and composition of the gas

also has an effect on the temperature of the melt pool and hence residence time [38]. These observations highlight the importance of the plasma torch to produce clean ingots.

2.4.1 Current Research

To date most research concentrates on the plasma torch and focuses on one of two areas: the plasma torch (the main components of which are the two electrodes and the plasma plume) [39-43] or the work piece on which the torch is applied. In each case the work piece or plasma torch respectively are considered only with regard to its effect on the boundary conditions [2]. Either way for research to be successful an understanding of how the two interact is important. The importance of this understanding is particularly highlighted by research that has been carried out showing the effect of torch conditions on the current distributions, temperature distributions and hence fluid flow in the melt pool [29, 38].

2.4.2 Physics behind Plasma Torches

Plasma, commonly known as a fourth state of matter, is ionised gas containing electrons and positive ions. Plasma is formed within a torch by ionising gas, by forcing it through an electric field produced between two electrodes in the gun. This gas plume then forms an arc with an electrode with an opposing polarity.

The plasma gun is used to produce and direct the plasma jet and to focus it on a work piece. In general there are two types of plasma, known as cold (non-thermal) and hot (thermal). For hot plasma the system is in thermal equilibrium i.e. the temperature of the gaseous ions and electrons are the same. This phenomenon can also be referred to as having kinetic equilibrium due to the relationship between temperature and mean kinetic energy. Both hot and cold plasmas are formed in the same way but at different pressures. If the

pressure is not high enough cold plasma is formed as, due to their small mass, the electrons are accelerated to a greater degree than the ions, causing them to have a higher temperature. These higher pressures also result in more collisions to occur causing hot plasma to have a higher ionisation and energy density.

High temperatures can be achieved in the hot plasmas, making them useful for refining operations and torches generally operate between the temperatures of 2,000-20,000 K [9, 44]. The use of plasma in this form dates back to the early 20th century, but it wasn't until the 1970's that they were first used for a cold hearth furnace set-up [13]. It is thought that it was first applied to the production of titanium in the USA by the Frankel Corporation in 1981[45]. At this stage the hearth could be moved horizontally below a static torch allowing ingots of up to 3000 kg to be produced and in 1985 Retech started using the two torch system used in the setup described in this work [44].

2.4.3 Uses of Plasma

Plasma Torches are used for melting, welding, processing waste and spraying amongst other things. To date most research focuses on the latter three, however experiments and modelling of plasma welding techniques are particularly useful to enhance understanding of the plasma torch. For instance Gas Tungsten Arc, GTA, is a welding process that involves a reverse polarity torch similar to that seen in PAM. For instance K.B.Bisen, M.Arenas et al. [46] study of weld pools can be used to give an idea of the ratio of melt pool depth to radius.

2.4.4 Variables

2.4.4.1 Torch Gases

In general terms a variety of gases can be used to create a plasma plume for use in heat input. Argon and Helium are particularly utilized in applications where an inert atmosphere is needed.

Blackburn [12] suggests that due to the high conductivity (0.142 W/mK [47]) and ionization potential of He the thermal energy transferred to the plate is relatively high. However Ar is often used instead of or in addition to despite it having a much lower thermal conductivity (0.016 W/mK[47]), which is due to it having a higher ionisation energy.

As described, plasma in its basic form is ionised gas, the kinetic energy of which corresponds to the temperature of the gas. The minimum ionisation energy needed for plasma to form corresponds to the energy needed to remove an electron from the outer most shell of an element and therefore vary depending on the gas used. Using the Maxwell-Boltzmann distribution the average temperature of the torch can be estimated, as shown below. A similar method has been described in previous work [13]. However it should be noted that these temperatures are based on the assumption that 100% of the gas has been ionised. This is very rarely the case and in general Ar is assumed to have a much lower maximum temperature of 11,000 K [42].

Table 2.1: Ionisation and Equivalent Temperature of Plasma Gases

Element	Ionisation Energy (eV)	Temperature (K)
H	1.36E-18	1.E+04
He	5.44E-18	3.E+04
Ar	4.43E-16	2.E+06

2.4.4.2 Transferred vs. Non-transferred

In the plasma furnace used for this work a reverse polarity transferred torch is used. This means that the plasma jet is formed outside of the torch with the work piece forming an electrode. Ideally in a reversed polarity torch the electrode forms a anode and the work-piece forms a cathode. The electrodes transfer kinetic energy to the anode causing it to 'heat excessively' [48], when the anode is the electrode in the torch this effect can cause difficulties as it leads to erosion and need for the electrode to be replaced regularly. Therefore if the anode is the work piece the heating further aids the growth of the melt pool. However these torches require the electrode to be tungsten, increasing the risk of tungsten entering the melt, making it unsuitable for PAM with aerospace alloys.

Not as much research has been carried out on transferred arcs as their non-transferred counterparts. This may be as their use is more limited as the work piece must be electrically conductive to allow it to act as an anode. However for applications such as welding they have proved to be more efficient leading to a number of papers being published in that area.

2.4.4.3 Efficiency

Over the years plasma torches efficiencies have been improved. This can be demonstrated by the difference in temperature that could be seen in the 1960s (when torches were reported to have maximum temperatures of 13,000 K [49]), despite the voltage needed to maintain the arc decreasing from approximately 750 V in the 1980s [12] to approximately 200 V.

The efficiency of a transferred torch is said to be 70-80% (the heating of the work piece/input power)[9]. For non-transferred, the efficiency is based on the ability to heat the plasma gas and is approximately 40-50%. The difference between the efficiencies is in part due to the position of the anode. The heat generated at the anode is relatively high, in transferred torches this is utilized to melt the work piece, however for a non-transferred set-up it is used to heat the gas that then in turn heats the work piece.

The Equation for calculating the efficiency of welding is shown below:

$$\eta = P_o / IV_a \quad \textbf{[42, 43, 50]} \qquad \textbf{Equation 2.6}$$

where P_o is the net Power received by the Work Piece (W), I is the Torch Current (A) and V_a is the Arc Voltage (V).

The overall efficiency of a plasma torch can be broken down into the efficiency of the torch, linked to the cooling system, and the efficiency of the plasma plume (approximately 30-40% [43], the latter of which can be influenced by the arc length of the plume by the Equation below. This theory is expanded in the discussion of the radiation trials later in this thesis.

$$\eta_r = \frac{P_r L_a}{P} \quad [43] \qquad \textbf{Equation 2.7}$$

Where $\eta_r$is the efficiency of the radiation (%) (i.e. the percentage of the input power that s lost as radiation), P_r is the radiation power per metre (W/m), L_a is the arc length (m) and P is the input power (W).

R.M.Ward [13] suggests that the 'useful' power output from the torch is equal to the input power into the skull. The input was calculated by assuming the accumulation of energy in the skull is made up of the energy needed to increase the temperature of the feedstock from atmospheric temperature to the liquidus temperature and the output is equal to the heat loss from the skull.

For these calculations of the radiation and conduction heat loss, in addition to the approximate temperature gradients and dimensions, an emissivity for titanium of 0.15 and a thermal conductivity of 27 W/mK Ti-48-2-2 has been assumed. Emissivity is often a source of error in calculations, as described in later sections, due to its dependency on temperature and surface finish amongst other things, although 0.15 is a commonly accepted value. A literature review carried out as a part of this thesis suggests that the thermal conductivity may be lower than suggested by R.M.Ward [13] (see Table 2.2 below). The impact of a lower thermal conductivity is that the same calculations would suggest a torch efficiency of 20%. Even though it is likely, given the high temperatures the Ti-48-2-2 skull would be at, that a higher thermal conductivity is in this case more accurate, it is interesting to note at this stage the impact such variables can have on calculations.

For the remainder of this work an approximate efficiency of 35% will be used, taking into account the values from all the literature discussed in this section.

2.5 Alloy

Titanium alloys started being used in aerospace by Pratt and Whitney in the 1950s and now make up 36 wt% of a normal engine [51]. Titanium alloys have two phases, α and β, with structures of HCP and BCC respectively. The amounts of these phases that are present depend on the original alloy composition and the heat treatment they have undergone.

2.5.1 Microstructural changes in Ti-6-4 with temperature

Ti-6-4 is a titanium alloy with additions of 6 wt% Al, an α-stabiliser and 4 wt% V, a β-stabiliser, resulting in a beta transformation temperature of 882°C [52]. Above 250°C Ti-6-4 reacts strongly with atmospheric gases, so the inert atmosphere is particularly important at higher temperatures [52] as when titanium alloys are in a liquid state the protective oxide layer of the surface layer is destroyed [53]. Understanding the effect of these transformations on the microstructure can allow temperature predictions and hence melt pool depths to be estimated. For some alloys the orientation of the grains can give an indication of the liquidus and solidus lines and hence melt pool dimensions [13, 54, 55]. However for Ti-6-4 the beta phase continues to grow after solidification has stopped [13] therefore this method cannot be used.

2.5.2 γ-Titanium Aluminides

To evaluate PAM as a refining process and get an understanding of its complexity it is necessary to understand the alloys that will be processed in it. In addition to the more traditional alloys, PAM is used to process more advanced γ-titanium aluminides. Titanium Aluminides are being researched as an alternative to nickel alloys as they have an operation temperature of 800^{o}C [51] (Ti-6-4 operates at a maximum temperature of 315^{o}C [51]) and good resistance to titanium fire. TiAl refers to the gamma phase of the titanium aluminium

intermetallic. The intermetallic can also exist in two alternative phases: Ti_3Al (α_2) and $TiAl_3$ [21]. As suggested by the phase names, the ratios of Ti and Al varies for each phase contributing to different microstructures and hence properties. For the experiments described here the alloy Ti-48-2-2 will be used.

The properties of TiAl have not been as extensively researched as Ti-6-4 and this can lead to errors in modelling of melting processes. The data in Table 2.2 is taken from B.Li [56], who complied them from numerous sources in 1996 and has been since cited by Bisen et al[46] and Xia Xu et al [14].

One thing of particular note for this work is that the liquidus temperature for TiAl (1491 ˚C/ 1764 K) [14, 46, 56] is lower than that for Ti-6-4 (1660˚C/ 1933K)[57].

Table 2.2: Properties for TiAl 48-2-2 and Ti-6-4 [14, 21, 46, 56, 57, 58, 59, 60, 61]

Physical Constants	**Units**	**Values**	
		TiAl 48-2-2	**Ti-6-4**
Density, ρ	kg/m^3	3636[14, 46, 56]	4430[57, 58]
Thermal Expansion Coefficient, α	K^{-1}	$1x10^{-4}$[14, 46, 56]	$9.2x10^{-6}$ [59]
Thermal Conductivity, K	W/mK	11[14, 46, 56]	6.7[57]
Specific Heat, Cp	J/kgK	727[14, 46, 56]	560[59]
Solidus Temperature, T_{sol}	K	1764[14, 46, 56]	1877[57]
Liquidus Temperature, T_{liq}	K	1785[14, 46, 56]	1933[57]
Room Temperature Ductility, %EL	%	1.0-3.0[21, 60]	20[61]

As mentioned, TiAl is being considered as a replacement for Nickel-Superalloys giving a weight saving of 20-30% [21]. Papers focus on different areas of TiAl such as the defect tolerance and fatigue properties [22, 62, 63], TiAl's dependence on microstructure and the effect of manufacturing techniques [21, 31, 64-66]. However they all agree that the main disadvantage that must be overcome to improve the alloys standing in the aerospace market is the low room temperature ductility. The result of this is that TiAl is hard to process and consequently very microstructure dependent.

A good summary of these relationships was given by K.Kothari et al. [21], who listed the main microstructural features that influence ductility, shown in Table 2.3 below.

Table 2.3: Effect of Microstructural Properties on Ductility [21]

Property	Effect on Ductility
Grain Size	Decreasing the Grain Size leads to an increase in the number of grain boundaries that aids deformation (slip and twinning along the {111} planes)
Lamellar/gamma ratio (L/γ)	A ratio of 0.3 to 0.4 is suggested to give the maximum ductility and exsists when the α_2/γ
Impurity Level	Decreasing the O_2 content from 800 ppm to 370 ppm leads to a ductility increase from 2% to 2.7%

K.Kothari et al. [21] further states that L/γ ratio is influenced by the Al content. As seen in the comparison of refining techniques, Al content does not change significantly under the pressures in PAM and therefore can be controlled. From this it may be inferred that it is advantageous to look into the use of PAM for the processing of TiAl.

As the alpha phase is brittle in nature, stabilisation of alpha grains can be detrimental to the ductility of the alloy. Al is an alpha stabilizer and is prone to segregate to the alpha grains [12, 16, 67] causing changes in Al concentrations on a local scale. Oxygen is prone to segregate in a similar way making it imperative to control and understand segregation on a micro and macro scale as much as possible [16, 67].

Grain size will primarily be controlled during solidification in the crucible [68]. In general a faster cooling rate will result in finer grains, although the process can be much more complex than this[69].

2.5.2.1 Production of TiAl

The tight control needed to achieve the required ductility and high temperature strengths for aerospace applications increases the complexity of processing of this alloy. For instance the low oxygen content can be difficult to achieve if scrap is to be used. It is known that scrap can significantly reduce the cost of production, however its high oxygen content (1000-1500 ppm O [70]) can lead to multiple refining stages being required.

2.6 Inclusions

2.6.1 Types of inclusions

In titanium alloys there are two main types of inclusions that cause concern to manufacturers, hard alpha and high density inclusions (HDI). Hard alpha inclusions can theoretically be formed by any alpha stabiliser, however most commonly contain high percentages of nitrogen (approximately 10wt%[36]), forming TiN. In addition they contain varying amounts of alloying elements and up to 5wt% O [36]. HDI are commonly formed with heavier elements such as Tungsten, Molybdenum, Tantalum and Tungsten Carbides.

Inclusions can be introduced from the feed stock as well as by 'anomalous conditions' in the hearth [2]. These can be hard to detect [17], and diameters <1mm, dependent on the stresses applied, can be shown to be a crack initiator [16]. A typical inclusion is approximately 0.25 mm [16]. However PAM has an advantage over VAR as the melt rate and the torch power can be controlled separately for the cold hearth processes [71] giving a longer residence time at high temperatures.

2.6.2 Removal of inclusions

HDI fall to the bottom of the melt pool and are in most cases removed via buoyancy segregation in the skull. As a result they get trapped in the skull and are therefore not able to

be carried into the crucible. This effect can be seen on examination of the skull after a melt where X-ray inspection shows it to contain relatively high numbers of HDIs [72]. The temperatures that are achieved within the melt pool have a large influence on the processes that occur during melting. Hard alpha particle (TiN) have a melting point of approximately 2623-3223 K [71]. However it is unlikely that the melt pool temperatures will get that high unless directly under the torch (where temperatures are approximately 200°C above the liquidus temperature).

For titanium alloys at 1670 K and above nitrogen diffuses out [16] of the alpha grains into the liquid through the high temperature beta layer [73] (a few hundred μm thick [16]) surrounding the particle. In addition Zhang et al. [17] suggests the dissolution of TiN hard particles is controlled by the dissolution of Al through the beta into the particle which is dependent on the velocity of the liquid flow and can lead to an initial growth in size. X.Huang et al [2] suggests that the dissolution of hard alpha inclusions may in fact lead to the formation of further inclusions as the nitrogen forms TiN with the surrounding titanium if not redistributed quickly. However other researchers suggest that the due to the volume of inclusions being much less than the volume of the bulk alloy the influence of the diffusing nitrogen is negligible [16].

Wiliam R.Chinnis [72] reports on the implementation of a PAM furnace, with three hearth set-up, by Teledyne Allvac in the early 1990s. His research suggested that after some original operational problems, such as water leaks in the plasma torch, it was possible to produce billets with 100% removal of HDI and 99% removal of hard alpha inclusions. This was concluded after inspection of 6 ingots using X-ray and ultrasound. These results suggest a satisfactory inclusion removal in comparison to other refining processes, although care should be taken when using results from such non-destructive testing techniques where inclusions can be missed due to background noise from the bulk metal [36]. A.Mitchell

reports similar levels of inclusion removal for EBCHR resulting in inclusions on rotating parts occurring $1/10^5$ kg (equivalent to 99.9999% defect free occurrence)[36] although this is relatively low the aerospace industry in general require an incidence rate with even lower occurrences of inclusions ($1/5x10^5$kg) [16] suggesting an improvement even from EBCHR, an accepted technique, is still needed.

Ideally 100% of inclusions should be removed during a melt. Theoretically this could be possible if the inclusions were allowed to have long residence time in the liquid metal. However this is not economically favourable as longer melt times reduce output. As a result a significant amount of research has focused on the dissolution of Hard Alpha and HDI, in particular work by French and Canadian Universities into the dissolution of inclusions in titanium alloys using EBCHR [16, 36, 73]. The significance of the melt pool temperatures therefore can highlight the limitation in the associating residence time directly with the dissolution rate of inclusions. The graph below (Figure 2.2) shows the effect of temperature of the dissolution rate of TiN. It shows how the temperature can significantly affect the dissolution rate and suggest that approximately every 1°C causes the dissolution rate to increase by 5 ηm/min.

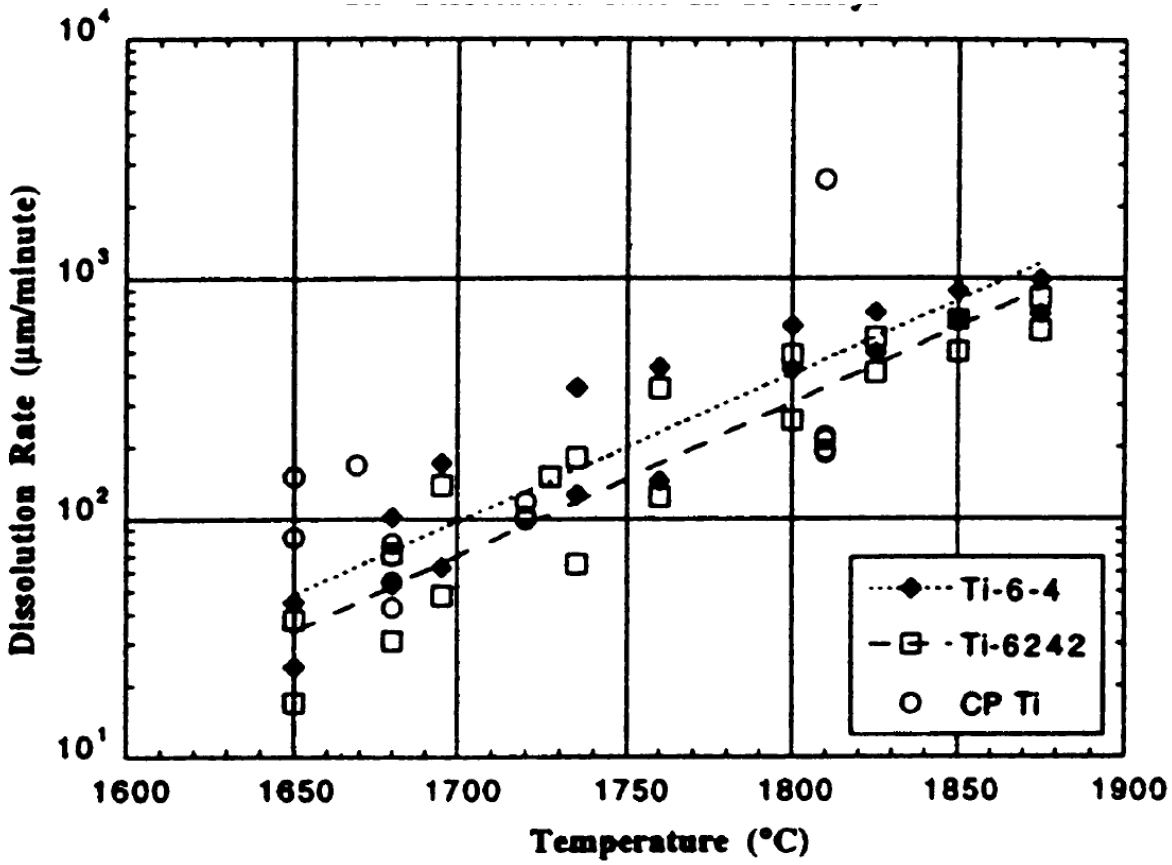

Figure 2.2: Variation in the Dissolution Rates of TiN in Titanium alloys with Temperature [74]

The density of the inclusions can have similar effects on rate of inclusion removal due to the temperature gradient in the melt pool. Low density inclusions float to the top of the melt pool, where the temperatures are high and therefore have a high melt rate. However medium density inclusions sink to the middle of the melt pool where temperatures are not as high and have the highest dissolution rate. Bellot et al. [16] suggest that as well as temperature and density, inclusion dissolution rates can be affected by the velocity at they are moving within the melt pool. They found that at higher velocities the dissolution time decreased (at a temperature of 1800°C the dissolution time decreases from 500s to 110s when the velocity increases from 0.1cms^{-1} to 10 cms^{-1} [16]).

From this it can therefore be ascertained that for 'clean' ingots to be produced a high average temperature and velocity is needed.

2.7 Homogenisation

2.7.1 Effect of mixing on homogenisation

Homogeneity is influenced by liquid flow in the melt pool. During melting their relationship is relatively simple. Natural convection is caused by density and buoyancy differences and the torch can create flow by the Lorentz force. Chu, 2004 [38] found that the torch current has a direct relationship with the temperature of the melt pool and at higher torch currents the temperature distribution was more homogeneous. The torch current consequently affects the liquid flow significantly, a link that has been made by many researchers [2, 23, 38, 40, 75-82] and a subject discussed in detail in the experimental section of this thesis. In general any mixing increases the homogeneity of the liquid metal and hence the final ingot. However it should be noted that mixing can have negative effects as it can allow inclusions to be dragged quickly through the melt pool, not allowing it to have a sufficient residence time to dissolve them [13]. In fact to get the best chance of removing all inclusions it is recommended that plug flow is used [13], in which, one compact is fed in at a time with no mixing, although this can have negative effects on the homogeneity.

2.8 Fluid flow

Fluid flow in a liquid melt pool is commonly considered to be controlled by three forces:

- Buoyancy Flow (using Boussinesq assumption)
- Marangoni force (linked to surface tension)
- Lorentz force (Cross product of current density and magnetic flux)

Buoyancy flow is the most commonly considered mechanism for fluid flow as it can be relatively easily calculated from the temperatures in the melt pool and the resulting density differences [27, 29, 83, 84]. Note the buoyancy flow can also be driven by differences in

local concentration, however these are harder to estimate. The Lorentz Force is linked to the current density and corresponding magnetic field and hence is closely linked to the current input from the plasma torch. As discussed in the comparison of EBCHR and PAM, the Marangoni force is not considered to be as significant for PAM. This is because the heat is distributed over a much larger area, decreasing the temperature gradients on the melt pool surface and hence reducing the surface tension gradient that would lead to Marangoni Flow.

The extent to which each of these forces compare to one another in a plasma melt pool is a matter of discussion. When considering the effect of fluid flow on the temperature distribution in a plasma hearth, Xia Xu et al. [14] ignores Lorentz force, concentrating on Buoyancy and Marangoni forces. This assumption is based on a paper by R.M.Ward and M.H.Jacobs [85], that Xia Xu et al [14], claim shows the Lorenz force to be 'relatively weak'. Their calculations compare the Lorentz Force (found to be approximately 3000 N m^{-3}) to the Buoyancy Force, calculated from the density, ρ, and volume, V (mass) of a material multiplied by the gravitational force, g. For titanium alloys this is approximately 40,000 N m^{-3}.

$$\boldsymbol{F_B = mg = (\rho * V) * g} \qquad \textbf{Equation 2.8}$$

However to properly compare the effect of Lorentz flow to Buoyancy Flow (rather than Buoyancy force), the difference in density between the hot and cold regions of the melt pool should be used.

$$\boldsymbol{F_B = \Delta mg = (\Delta \rho * V) * g} \qquad \textbf{Equation 2.9}$$

These fluid flow phenomenons when combined can be complex to model, particularly if the temperature dependent variables, discussed further in the method section, are taken into account.

2.9 Models

Models of a PAM furnace can have different levels of complexity, dependent on the assumptions being made and the area of the furnace being looked at.

2.9.1 Summary of Models

To date a few comprehensive models of PAM have been made. In addition models of more established processes (such as EBCHR) that may be applicable are not easily adapted to PAM without more information being determined, such as how the plasma plume effects the melting and fluid flow.

As with most models simplifying assumptions such as steady state fluid flow are often made, to make the model computationally viable. Ultimately a model that takes longer to run than a full scale experiment is not beneficial. In order for these assumptions to hold researchers often focus on modelling just one section PAM, such as the Hearth, Crucible or Plasma Plume.

2.9.1.1 Hearth Models

X.Huang et al. [2] presents a fairly comprehensive model of the refining hearth of the plasma furnace in order to examine the survivability of inclusions in the hearth. Like many models of this type it has the assumption that the torch heat flux had a Gaussian distribution [2], this assumption will be discussed further in later sections.

2.9.1.2 Modelling of the plasma torch

For the plasma torch to be modelled an assumption as to the state of equilibrium within the plasma is often made. There are three main types of equilibrium possible; Complete Thermodynamic Equilibrium (CTE), Local Thermodynamic Equilibrium (LTE) and the Two Temperatures description.

Many models use the LTE approach as it achieves a balance between accuracy and simplicity [1, 39, 41, 86]. These tend to model the flow and temperature distributions within a transferred arc simultaneously. S.M.Aithal et al.[39] justified this approach by showing there was little temperature difference between the electrons and heavy particles, allowing the single temperature distribution to be a valid assumption. However if the temperature or concentration gradient is too high CTE and LTE conditions cannot be met [1, 39, 87] and the more complex Two Temperature approach should be used [13]. This Two Temperature approach considers the temperature of both the electrons (T_e) and the heavy particles (T_h) [87-89]. E.Pfender et al. [89] used a two temperature approach in the region close to the anode and found there was up to a 12,000 K difference in the temperature of the heavy particles in comparison to the electrons. However this difference was only really apparent in the region within 0.2 mm of the anode suggesting that for most cases the LTE case is a valid assumption.

Additionally the plasma arc is often further modelled using a combination of mass, momentum, and electrical and thermal energy conservation Equations [1, 38, 39]. Although these models will not be recreated in this thesis their results will be used for comparative purposes and some of the results from are seen below (Figure 2.3). These governing equations are often processed by a finite volume or finite element in order to get a velocity and temperature distribution.

2.9.1.3 Results from Plasma Torch Models

A lot of research has been carried out on the temperature distribution for a transferred plasma arc. Most use similar methods to model the process, often working out the temperature distribution from a velocity distribution[38, 41, 90]. The results from some of these reports are summarised in the graph below. Of most interest here is the variation in temperature from the plasma centre line to the edge of the plume. Unfortunately despite a significant number of models, measurements of the temperature distributions are fairly rare. As shown in Figure 2.5 the temperature in a plasma plume varies fairly significantly radially, with the highest temperature isotherm being located just under the cathode.

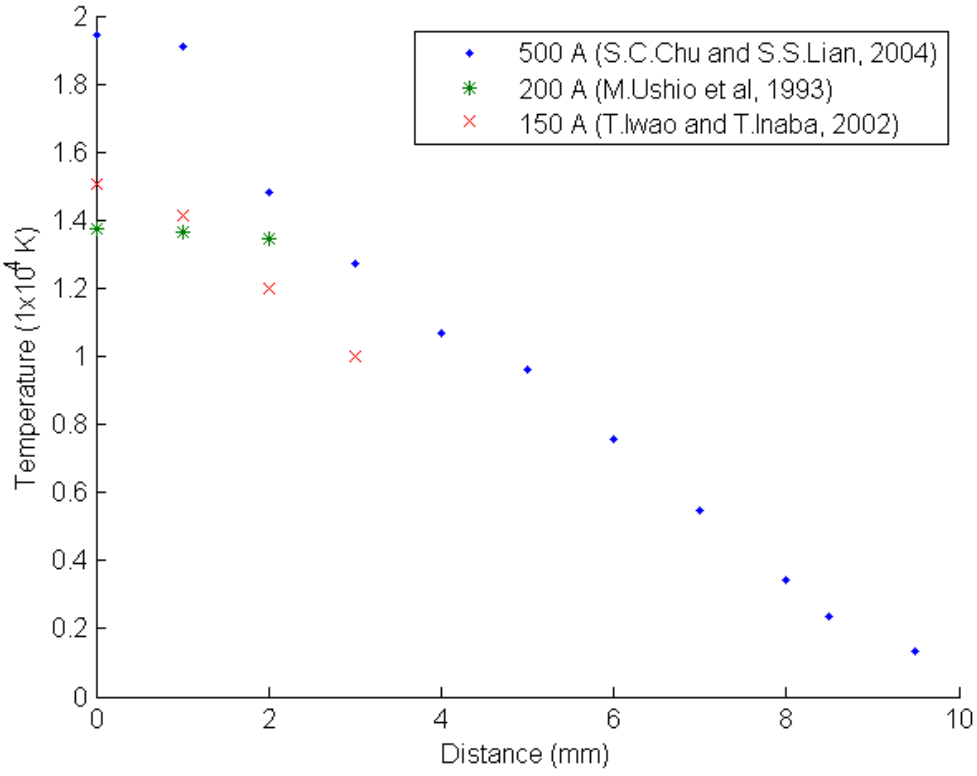

Figure 2.3: Plot of Temperatures within a plasma plume with distance from the centreline for currents of 500 A[38], 200 A[91] and 150 A[42]

2.9.2 Using experimentation to provide data for models

Experimentation can be used to provide input data and validate models. For instance melting experiments can be used to examine fluid flow and heat transfer by using a combination of sensors (such as thermocouples and voltage wires) [13, 25, 27, 92] and melt pool profiles aided by microstructural features [13] or the addition of tungsten ball markers [25] or powder [55].

Huang uses a combination of these things to examine the furnace refining hearth with additional seeded inclusion and water models to verify the movement of inclusions modelled [2].

Using experimentation to verify plasma plume models is more difficult. The plume is hard to observe visually, as the plasma gas is fairly optically transparent, so measurement of torch radius is difficult. In addition the very high temperatures in the torch making conventional temperature measurement techniques (such as inserting thermocouples) are impossible.

2.9.3 Important concepts for models

2.9.3.1 Boundary conditions

Huang X et al. [2]models the plasma's refining hearth and suggests three boundaries, the top surface, side surface and bottom surface. Huang et al. [2] deals with this by using a lower emissivity for the liquid region (0.23) than the solid region (0.4). These models also take into account the radiation between the solid skull and hearth through the inert gas. E.N.Kondrashov et al. [28] uses a similar technique to calculate the depth on the melt pool in VAR and show clearly in their work how the boundary conditions can be set-up dependent on the type of heat transfer that is assumed to occur at each boundary. They consider 6 boundaries in total, considering separate areas for the melt pool outside and under the

electrode and the area of the ingot directly in contact with the hearth and that separated by gas due to shrinkage in the metal. The area under the electrode is assumed to have a temperature above the liquidus temperature, and that outside of the electrode has a temperature less than and equal to the liquidus temperature. This would correspond to a liquid and solid region. From this it may be said that a hearth model could be further split, although the changes in boundary size with time, caused by the growth of the liquid region, may complicate the model. Huang does not appear to consider the effect of different amounts of shrinkage with temperature; however as the percentage of the ingot that is in a solid state is less than that for VAR, it may be considered fair to assume a constant air gap.

2.9.3.2 Turbulence

In addition to this turbulent flow may also need to be considered. Turbulence is difficult to accurately model however there are a number of techniques to model the effect of turbulence on the energy of the process. One of the most common is the K-ε model that models turbulence in terms of kinetic energy (represented by K_E, the mean kinetic energy and k_E, the turbulent kinetic energy) and the rate at which the energy is dissipated.

When modelling processes simplifications are possible by making certain assumptions about the process. For instance for VAR it is assumed that fluid flow in the melt pool is only influenced by the buoyancy driven flow and is laminar (no turbulence is accounted for). K.M.Kelkar, S.V.Patankar and A.Mitchell [93] however suggest that turbulence is assumed to occur due to the 'large length scales and substantial temperature differences' and uses a K-ε model to account for turbulent mixing. As the length scales are less for PAM than either VAR or ESR due to the horizontal hearth (note it is the vertical height that is often assumed to be the length over which liquid moves), particularly in small scale hearths an assumption of laminar flow in the melt pool may be reasonable.

This can be checked using the following equation for the Reynolds number (dimensionless) and using the assumption that flow is purely laminar if the Reynolds number ≤ 2100 [94].

$$\mathbf{Re} = \frac{\textbf{Inertial Forces}}{\textbf{Viscous Forces}} = \frac{\rho v L_{Re}}{\upsilon} \qquad \textbf{Equation 2.10}$$

where v is the mean velocity in respect to fluid and is assumed to be 10 ms^{-1}; L_{Re} is a length that can be assumed to be the hearth depth (0.025 m), υ is the viscosity ($kgm^{-1}s^{-1}$) and ρ is the density (kgm^{-3}). As viscosity is both material and temperature dependent the following Equation 2.11 was used. It is based on results from a levitation experiment carried out by P.F.Paradis, T.Ishikawa and S.Yoda[95]:

$$\upsilon = 4.42 - \left(6.67\text{x}10^{-3} * (T - Tm)\right)/1000 \qquad \textbf{Equation 2.11}$$

Where υ is the viscosity in Pas (or $kgm^{-1}s^{-1}$) and T and Tm are temperatures (K).

Assuming that the temperature ranges between 2150 K (approximately 200K above the liquidus temperature) and the liquidus temperature, 1950 K the viscosity was calculated to be $3.086\text{x}10^{-3}$ and the resultant Reynolds number was 810. As this is less than the threshold limit of 2100 discussed above then laminar flow is a fair assumption.

2.10 Conclusions from the literature review

Refining in the PAM furnace relies heavily on the volume, temperature and flow of the metal in the liquid melt pool as literature shows this increases inclusion removal and homogenisation. Refining is also therefore influenced in the large part by the increase in input and decrease in output of thermal energy into the melt pool in the hearth. On

examination of the governing equations and literature some suggestions can be made how increased input and decreased output can be achieved:

- Increasing the resistance between the hearth and skull by adding insulation between them to reduce heat loss via conduction
- Increasing the distribution and temperature of the plume when it meets the melt pool surface (suggested to be linked into torch power and arc length)

Literature also showed how materials properties, such as liquidus and solidus temperatures and thermal conductivity can affect the input and output into the melt pool. Finally models of the plume have shown that its temperature ranges between 20,000 K and 1,000 K varies radially from the centre. However there has been found to be a lack of experimentation to verify their claims.

Modelling of the PAM hearth has been much less apparent and examination of literature also highlighted the limitations in transferring data from previous VAR and EBCHR research directly to the PAM furnace. Removal of inclusions differs between VAR and PAM due to the horizontal hearth; however the use of an electric arc makes melt pool growth mechanisms and fluid flow behaviour fairly applicable. Research into EBCHR on the other hand provides an insight into the behaviour of the inclusions in the hearth, although fluid flow differs within the melt pool due to there being no significant Lorentz force effect. Nevertheless, these gaps in processes can be bridged if more detailed knowledge of the current density and heat flux resulting from the torch can be ascertained.

3) Aims and Objectives

The main aim of this work is to assess the efficiency of the plasma torch and how it interacts with the ingot in order to provide insight and potential advice on how the process can be improved. This can be broken down in to the following aims:

- To evaluate the torch as an energy input into the ingot.
- Assess the flow of electrical and thermal energy through the ingot
- To gain an understanding of energy losses from the torch

This will be achieved by carrying out a number of objectives:

- Carry out visual measurements of the melt pool growth as torch parameters are varied.
- Equate the surface area to energy inputted into the ingot.
- Utilise thermocouple and voltage measurements at near surface positions on a plate to evaluate energy flow from the plasma plume into the ingot.
- Use measurements to better understand the plume diameter and depth of the melt pools created.
- Calculate the radiation energy from the plume and estimate the energy lost using thermocouples facing the plume and relevant view factors.

4) Study of the melt pool growth

There are many variables that can affect production of an ingot such as torch current, arc length, alloy being used as the feedstock, insulation in the hearth, furnace pressure and gas flow rate amongst others. It was therefore felt that a good place to start was to get a basic idea of the effects of these variables on the process.

The reactive nature of the titanium alloys being melted restricts the techniques that can be used to analyse the process. Access to the furnace is also limited whilst the plasma torch is on due to the atmosphere needed to prevent reaction of the titanium. Therefore initial observations of the behaviour of the melt pool were made using one of two view ports built into the furnace. These view ports, mounted with cameras, are used by operators to observe how the feedstock is being melted during hand operated stages of the melt. These cameras were used to video a simplified melt for different conditions (see Table 4.1). During these melts a solid skull that had been previously formed in the hearth and allowed to cool was used. The torch was applied to the centre of the skull for approximately 20 minutes to ensure the melt pool was allowed to reach its optimum size. A static torch was used to allow a single melt pool to be observed as it grows over time.

4.1 Method

These videos only show the surface of the melt pool, however literature has suggested a link between the size and the average temperature of the melt pool [71]. Therefore the growth of the melt pools can give a fairly good indication of the effect of the variables. Four variables (Current, Arc Length, Insulation and Alloy) were examined over a number of melts.

Table 4.1: Conditions for each Trial

Variable	Alloy	Current (A)	Actual Current* (A)	Arc Length (cm)	Insulation (Yes/No)
Current	Ti-6-4	650	636	10	Yes
	Ti-6-4	550	541	10	Yes
	Ti-6-4	450	385	10	Yes
Arc Length	Ti-6-4	550	531	5	Yes
	Ti-6-4	550	531	10	Yes
	Ti-6-4	550	537	15	Yes
Insulation and Alloy	TiAl	450	548	10	Yes
	TiAl	450	531	10	No
	Ti-6-4	450	528	10	Yes
	Ti-6-4	450	543	10	No

***The 'Actual Current' is based on the average of all the currents recorded over time during the entirety of the melt.**

4.1.1 Method for analysing results

Once recorded these videos were analysed as individual frames to show the growth of the melt pool over time. Image analysis is a process that has been researched for a wide range

of purposes and has increased in accuracy with the introduction of higher resolution cameras and improved imaging processing software. A recent paper presented at the 2013 LMPC conference by Trevor J.Watt et al [54] showed how a combination of an image processing software, 8 megapixel SLR camera and Matlab could be utilised. Although their research was focused on a much smaller scale (a microscale), the process to obtain a melt pool shape (a macroscale) is much the same.

In general the method proposed in the aforementioned paper is to process the raw data from images. Filtering methods were used to reduce 'noise', improve clarity and finally quantify the features of interest. Once split into individual images, filtering was carried out using Matlab whilst the frames were still in video format, by utilising a moving average of 10 frames at a time. The hope is that this will remove any bright spots in the images that is likely to be caused by side arcing of the plume [13].

As multiple frames were recorded per second resulting in thousands of frames over the time recording was taking place not all of these were processed. Frames at certain times (100, 300, 600 and 800 seconds) were chosen over the first 800 seconds (after this stage the melt pool size was observed to plateau). The brightness and contrast of these frames were subsequently adjusted to define the melt pool better. The final stage was to then quantify the area of the melt pool in m^2 to assess how it grows with time.

There were two ways that were looked at to measure, as accurately as possible, the size of the melt pool for the selected frames. The first was a threshold method where any area over threshold brightness was selected and the area was calculated. This method worked as long as the threshold was adjusted for each image whenever the brightness varied.

Table 4.2: Error using ImageJ, showing the values for area when the same image is measured 5 times

Test number	Area (cm^2)
1	115.09
2	114.68
3	114.88
4	114.34
5	114.41
Average	114.68

The second method was to use the free hand tool in an image processing software to draw around the melt pool. The area of the region drawn around was measured in pixels by the software which was then converted to an area in metres. This was done by drawing around the edge of the skull from one of the frames and equating the number of pixels to the known area of the skull. It was found that this method more accurately found the melt pool edge although it introduces human error. The extent of this error is shown in Table 4.2 that shows the areas measured by the same operator over a period of a few days.

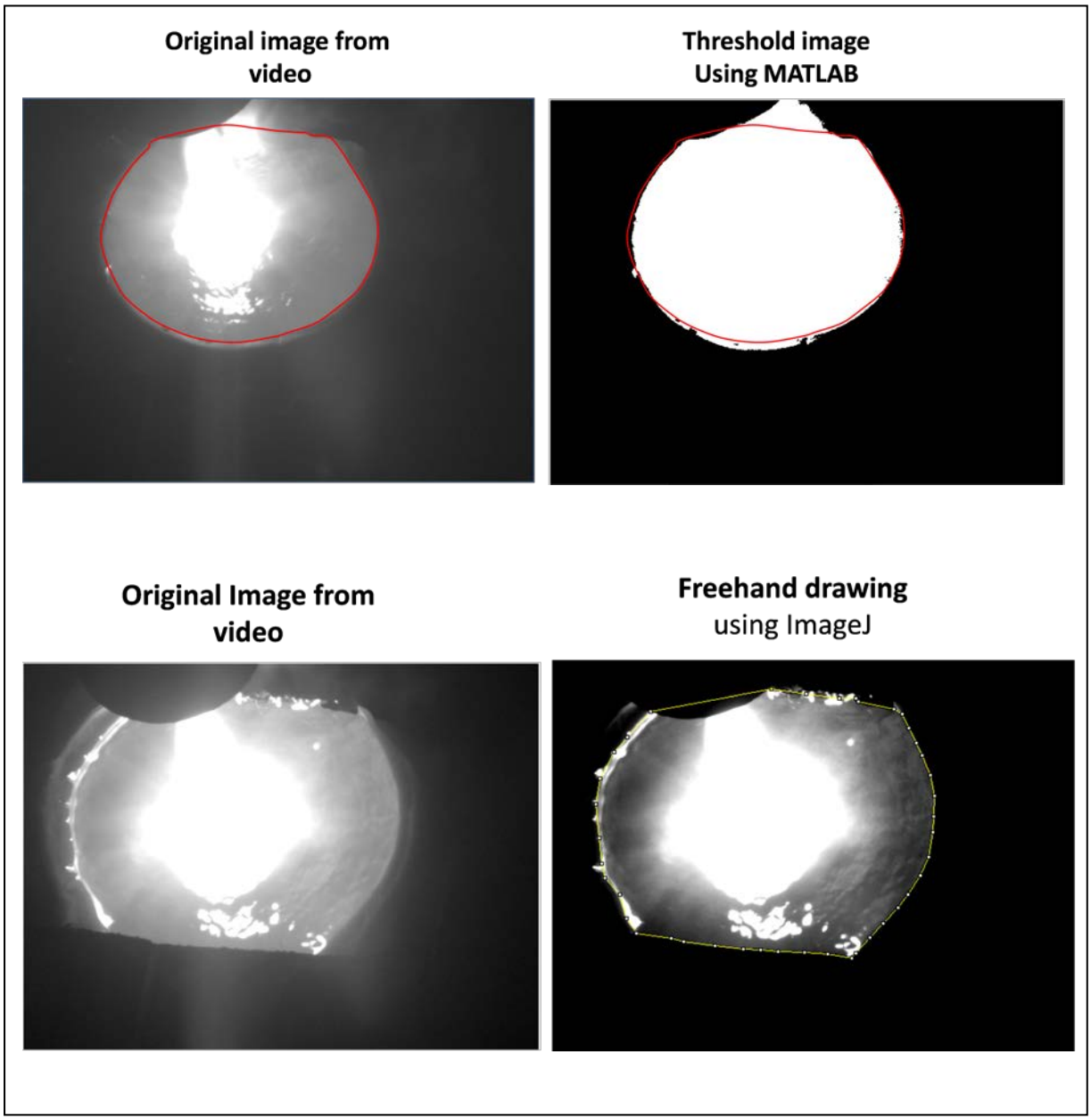

Figure 4.1: Frames from the videos of the melt showing how the melt pool area is measured

As shown in Figure 4.1 the image was still processed to a certain extent before the area was drawn around. The hope was that by adjusting the contrast the melt pool will become more visible and any region such as the mushy zone shown in the bottom left hand image is not counted.

4.1.1.1 Conversion of Area to Energy

In order to fully understand the results it is necessary to also look at the melt pool in terms of energy. The areas measured can be equated to the energy required to make the melt pool. i.e. the amount of useful energy from the torch (as shown in Figures 4.3, 4.6, 4.9 and 4.11). This was done using the following equation:

$$E_{IN} = C_p(T_L - T_0)\rho Vol \qquad \text{Equation 4.1}$$

Where E_{IN} is the Energy input into the melt pool (kJ), T_0 is the starting temperature (assumed to be equal to the room temperature) and Vol is the Volume of the melt pool (m^3)

The volume of the melt pool was estimated using the following equation:

$$Vol = \frac{\pi h}{6}(3a^2 + h^2) \qquad \text{Equation 4.2}$$

$$A = \pi a^2 \qquad \text{Equation 4.3}$$

Where a and h are the radius and depth of the melt pool respectively. These equations can be combined to eliminate a and reduce the number of values that must be estimated.

$$Vol = \frac{Ah}{2} + \frac{\pi h^3}{6} \qquad \text{Equation 4.4}$$

The depth of the melt pool, h, can then be estimated using Grong's Equation and using boundary conditions calculated in later sections (this model assumes a torch is moving so the minimum possible velocity of 0.025 mm/s had to be used to approximate a stationary torch). As a part of the depth model the diameter of the melt pool is outputted, from which the area can be calculated. This diameter was converted to a melt pool area and compared to the melt pool area measured during the experiment for the same conditions. These areas were comparable, suggesting the error from the moving torch assumption was negligible. Further information about the methodology of Grong's Equation and the boundary conditions are documented in 'Section 5.5.3.1 Moving Torch' of this thesis. The depth is calculated from the following inputs: torch power and physical materials properties.

On examination of these equations it can be noted that there are a number of variables that will affect the melt pool area and therefore energy in the melt pool. The first of which is the alloy being melted, in particular the specific heat, Cp and the solidus temperature, which both have a positive relationship with input energy. The second is the power received from the torch calculated from the current, I, and voltage, V with an assumed efficiency of 0.35 (this assumption was discussed in Section 2.4.4.3 Efficiency), which has a direct impact on the depth of the melt pool. The final variable is the area of the melt pool, from which the volume can be approximated and this is measured during the experiments as discussed.

4.1.2 Torch Current

4.1.2.1 Method

The torch current refers to the input current to the torch used to produce plasma by ionising the plasma gas. It is expected that the torch current will have a positive relationship

with the melt pool size i.e. at higher torch currents larger melt pools are formed. These assumptions are based on Equation 4.5, that shows that if the voltage (V) is constant[96], the power (P) increases with current (I).

$$\mathbf{P = IV} \qquad \textbf{Equation 4.5}$$

It has been suggested that higher currents quickly burn out the electrode, however lower levels decrease the arc stability [97]. On a similar note there is research that suggests that for higher currents the temperatures in the plume are more evenly distributed [38]. Although it will not be possible to study these effects during the experiments here, it is important to note the influence of torch current over long periods of time. It is also significant as it highlights why, even if the relationship between torch current and melt pool size is positive, it is not economically viable to simply use very high currents.

4.1.2.2 Results

For this work three currents were used representing a high, medium and low current relative to this torch.

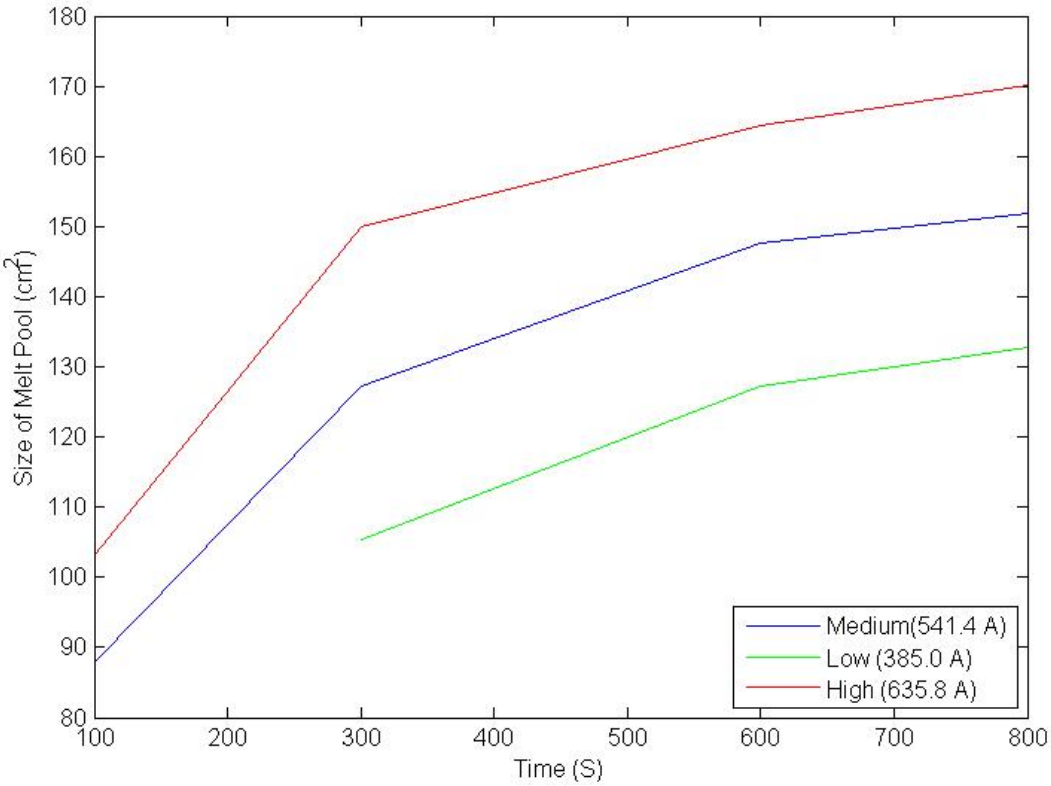

Figure 4.2: Effect of current on the Area of the melt pool

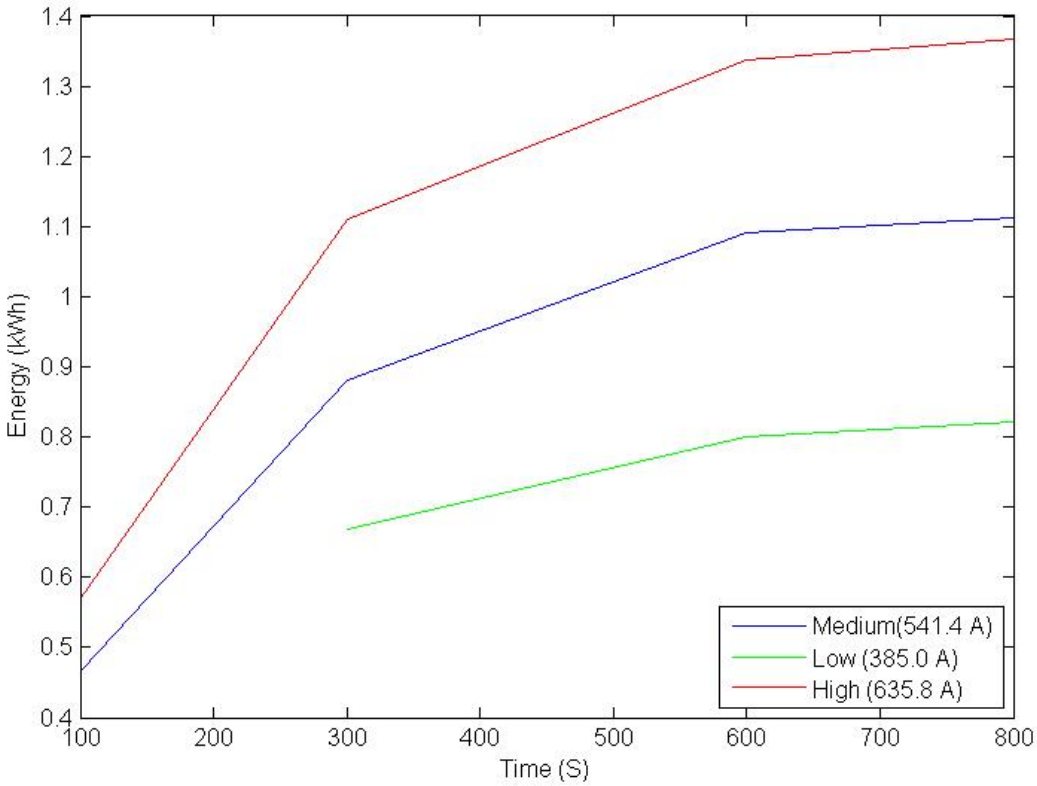

Figure 4.3: Effect of current on the Energy inputted into the melt pool

Figure 4.2 and Figure 4.3 show the change in the size of the melt pool and Energy in the melt pool with time for different torch currents. The first point for the 'Low' current (green line) hasn't been plotted as the camera was not properly orientated at the start of the video until it was adjusted at 155 seconds.

4.1.2.3 Discussion

The currents shown in the graph legend in Figure 4.2 refer to the average current logged whilst the torch was on. The standard deviation for each current is 0.4665, 0.3754 and 0.3246 for the low, medium and high current respectively. This suggests, to some extent, that the torch is more stable at higher currents, agreeing with the reports from literature. However this pattern could only be verified properly with further repeats.

From the results it can also be inferred that an increased current causes a larger melt pool, however the extent to which current relates to surface melt pool area is not immediately obvious.

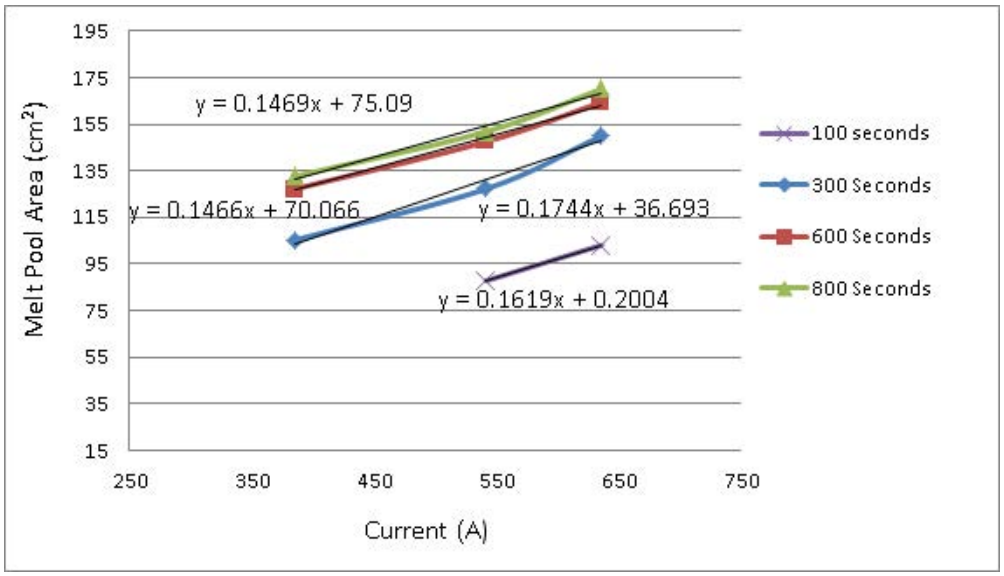

Figure 4.4: Effect of changing current on the melt pool area

Figure 4.4 shows how the current affects the melt pool area. Each line represents a common time for each melt. Therefore the gradient represents the rate at which the melt pool size changes with current. The gradients are fairly consistent for each suggesting that the effect of current remains constant throughout the melt.

This linear relationship was then used to correct for the difference between the current set during the melt and the actual torch current produced for subsequent trials. For instance the torch current was set to 550 A for all arc length melts (rows 4-6 in Table 4.1). However the currents were recorded to be 531 and 530 A respectively. The average gradient of the lines, k, was used to correct values using the Equation 4.6

$$X = ky + c \qquad \textbf{Equation 4.6}$$

Where X = Corrected melt pool area

y = Difference in current (expected-actual)

c = Calculated melt pool area

Finally it is possible using this data to get an idea of the efficiency of the torch. The torch voltage is taken to be 150 V, for the currents 385.0, 541.4 and 635.8 this equates to a power of 57.8, 81.2 and 95.4 kW respectively. Over the 800 seconds the torch is run this is an energy output from the torch of 12.8, 18.0 and 21.2 kWh respectively, resulting in efficiencies between 0.061-0.064. No pattern was seen to suggest that the size of the current affects the efficiency of the torch. Given the torch is accepted to have an efficiency of 0.35, it may be estimated that of the energy that reaches the ingot a fraction of 0.18 is utilised in melting the metal. Although the author suggests these energy efficiencies should be used only as a guide at this stage as numerous until some of the estimations (e.g. depth of the melt pool) can be replaced with measurements.

4.1.3 Arc Length

4.1.3.1 Method

For a non-transferred torch the arc length is fairly difficult to correctly ascertain a value for. It is heavily influenced by the torch current, flow rate and pressure [98]. However for a transferred torch, used for all of these experiments, the arc length is directly related to the distance between the cathode and the work piece (the anode). Therefore the arc length can be calculated fairly simply by measuring the torch height. Due to the anode being held within the torch, the part of the plasma plume within the casing is concealed. This distance is hard to measure without dismantling the torch and therefore there is a constant error for the visual experiments. T.Iwoa [43] made the distinction between the ‘actual’ arc length and the

'appearance' length, L_a in order to acknowledge this error. For later discussion of the arc length in regards to the plume height used in radiation calculations it is only L_a that is of significance, so the error is not relevant.

4.1.3.2 Results

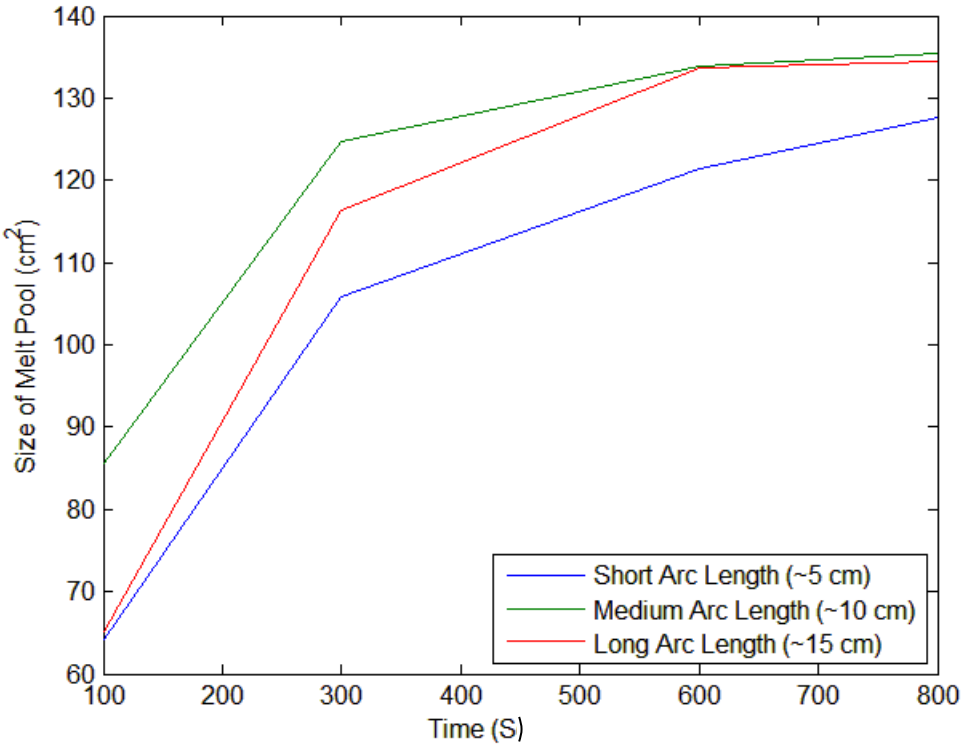

Figure 4.5: Graph comparing the effect of arc length on the area of the melt pool produced with an insulated hearth and a torch current of 550 A

The Arc lengths referred to in Figure 4.5 are noted in order to compare them to each other. They were recorded from the 'Torch Height' (equal to the arc length) recorded on the control panel, and are relative to an arbitrary origin point. This origin point should represent the top of the cathode; however it is often a number of cm's above this point. The torch heights shown in Figure 4.5 are corrected based on the position of the torch (measured from bottom of the torch to the surface of the work piece using a centimeter ruler) when the control panel reads the position as '0 cm'.

On examination of the results in Figure 4.5 it could be suggested that medium arc length produces the largest melt pool at the highest melt rate. Interestingly, during a conversation with the regular torch operator, it was revealed that this medium arc length corresponds to the torch height most commonly used during a melt. This is because they found by trial and error it to be the most effective.

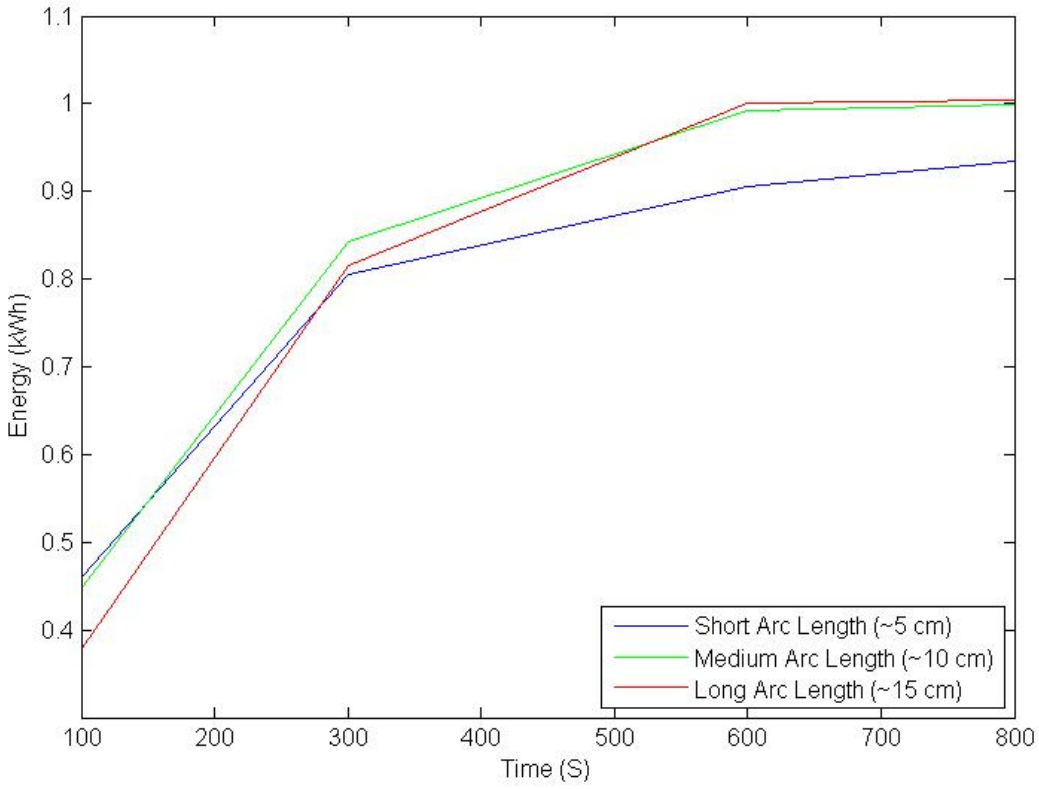

Figure 4.6: Graph comparing the effect of arc length on the energy in the melt pool produced with an insulated hearth and a torch current of 550 A

4.1.3.3 Discussion

Figure 4.5 and 4.6 suggests that there is an optimum arc length. A low arc length causes a small melt pool; this is possibly linked to the positive relationship noted between arc length and radius by previous research [42]. If the radius of the plume was decreased there would be a smaller area over which heat can be transferred (i.e. A_p would be smaller). It was also found that the highest arc length gives a larger melt pool than the low arc length.

However the melt rate is slower than at the medium arc length. This may be linked to radiation from the arc. A longer arc length is likely to decrease the efficiency of the torch as more heat is lost to the atmosphere.

These results suggest that there is an uneven temperature distribution within the torch flame with a higher temperature region in the centre. This agrees with the results shown by Chu, 2004, [38] whose research also suggested that at higher torch currents the effect of arc length would be less as the temperature distribution is more even.

For this trial the efficiencies for the short, medium and long arc lengths were found to be 0.05, 0.056 and 0.056 respectively after 800 seconds. Interestingly after 100 seconds the torch efficiencies are in the opposite order with the most efficient being the short arc length (0.207) then the medium arc length (0.20) and finally the long arc length (0.17). This may further explain the existence of an optimum arc length. The comparably high energies found for the short arc length in the early stages may also suggest a melt pool that has a higher depth to area ratio than at the higher torch arc lengths.

4.1.4 Insulation

The impact of the research carried out by R.M.Ward [13], discussed in the literature review, was the use of insulation on the bottom of the hearth in the furnace at the IRC for all melts. As a result it was felt necessary to repeat these experiments on the hearth to confirm these effects.

An insulated layer was placed between the bottom of pre-made skulls (made of Ti-6-4 and TiAl) and the hearth. The same solid skulls were used for both of the insulation experiments (with and without insulation) and set up as seen below. (It should be noted that Figure 4.5 shows example skulls that are similar, but not the same, to those used in the experiment in order to compare insulated and non-insulated skulls).

Figure 4.7: Example picture of two skulls with and without insulation

Table 4.3: Showing the Thermal Conductivities of the materials between the skull and the hearth. [14, 45, 56, 57]

Material	Conductivity (W/mK)
Insulation Materials	0.035-0.16
Titanium	22
Ti-6-4	6.7
TiAl	11
Argon Gas	0.016

Table 4.3 shows thermal conductivity of the materials through which heat is lost from the skull via conduction in a plasma furnace. With no insulation there is a rough surface under the skull (as shown in Figure 5.20) through which heat is conducted through the titanium, where the skull is in direct contact to the hearth, and argon. Therefore even though argon acts as a good insulator, as shown by the low thermal conductivity, a relatively large amount of heat is lost. Insulation prevents the problems with skull/hearth contact as it acts as a physical barrier between the two. Therefore in theory [13] the heat output along the bottom of the hearth is decreased.

4.1.4.1 Results

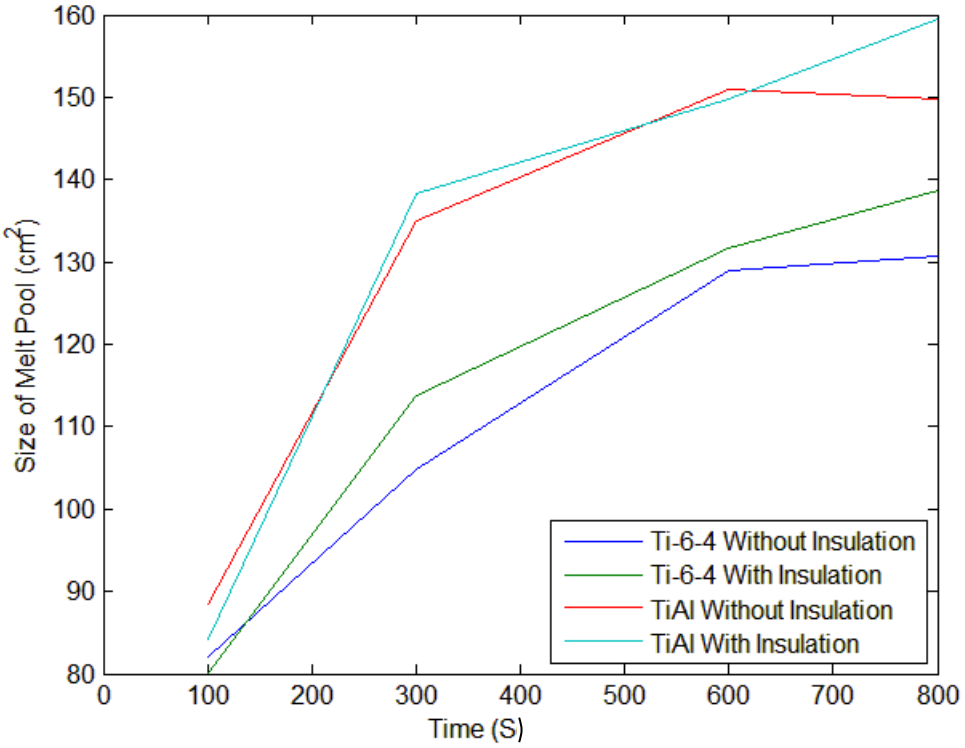

Figure 4.8: Effect of Insulation on the Melt Pool with a torch current of 450 A

Figure 4.8 shows the effect of insulation over 800 seconds of a melt. Four points have been plotted at the same time intervals as the previous experiments. For Ti-6-4 (the bottom two lines) the insulation seemed to have a notable effect on the melt pool size. However for Ti-48-2-2 the insulation seemed to have little effect on the melt pool area. The same conclusions can also be drawn by examining Energy vs. Time graph below (Figure 4.9).

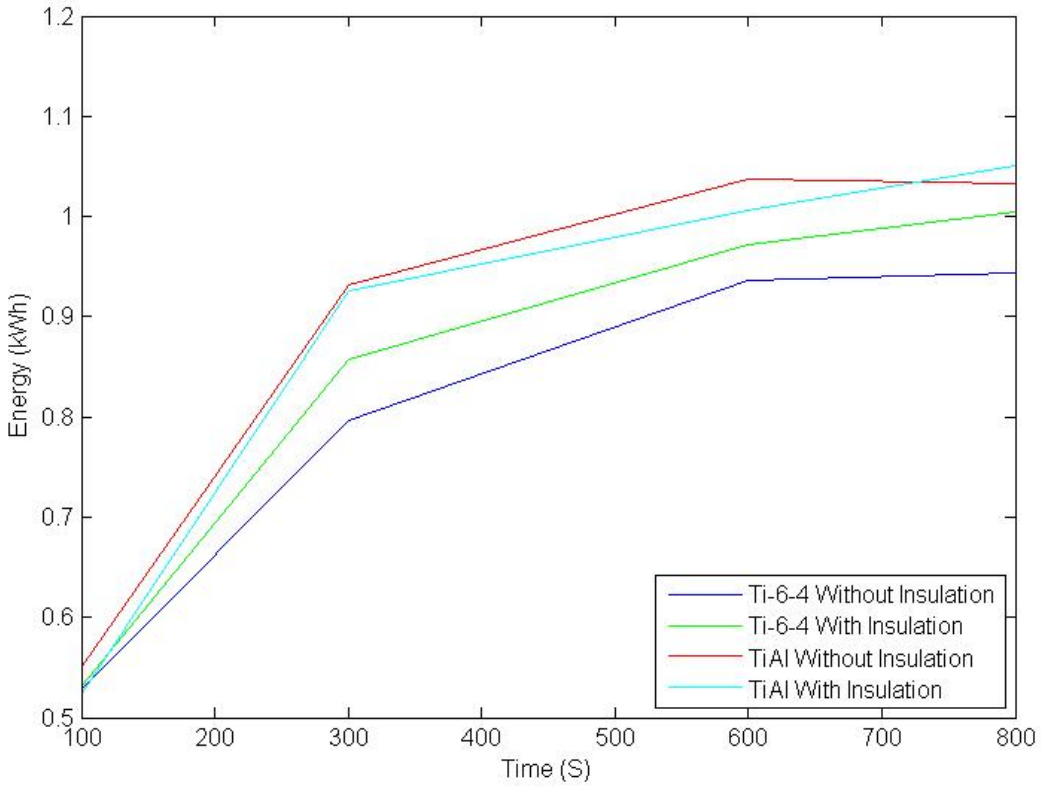

Figure 4.9: Effect of Insulation on the Energy in the melt pool

As the insulation was placed between the bottom of the skull and the base of the hearth and not the sides of the hearth, it is possible that a significant amount of thermal energy may still be lost to the sides of the hearth (as described in the energy balance in the literature review). Therefore it was decided to study the first four minutes of the melt pool growth, before the melt pool has made contact with the sides of the hearth.

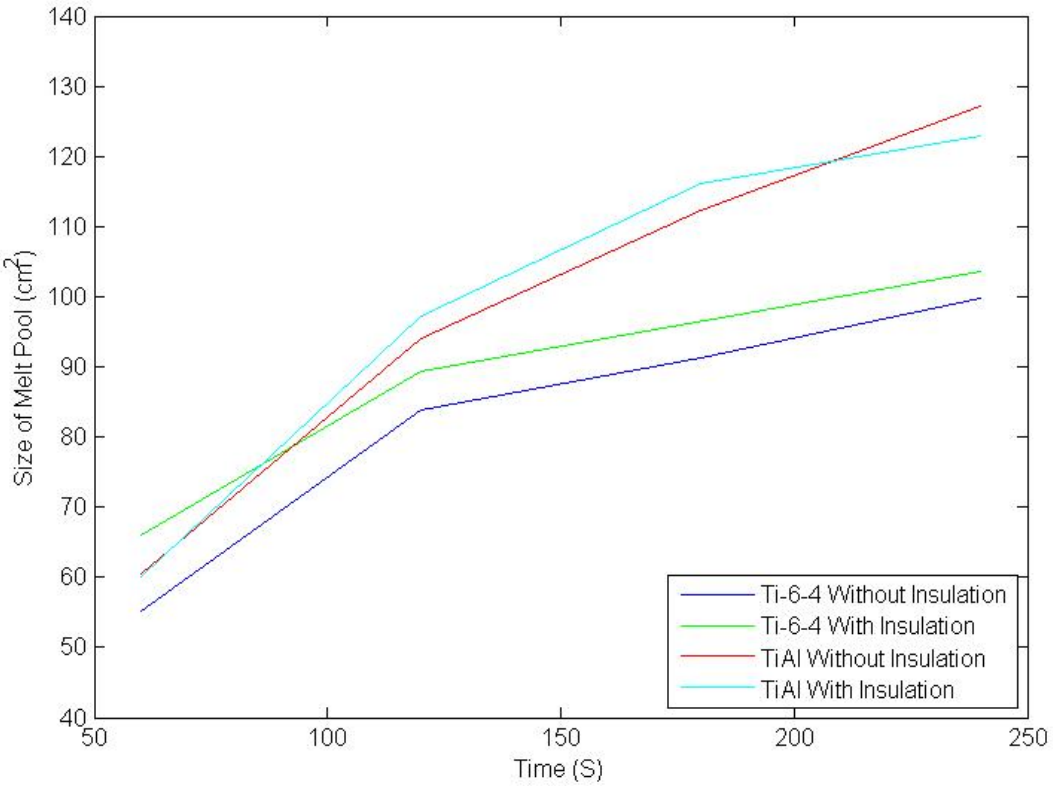

Figure 4.10: Effect of Insulation in the initial stages of Melt Pool growth

Figure 4.10 suggests that over this initial growth phase the insulation seems to have a slightly greater effect on the melt pool growth. In addition to this there is also a smaller difference between the melt pool surface area for the two alloys. Figure 4.11 agrees with the latter statement however shows little difference between the melt pool area for TiAl with or without insulation.

For all the melts the growth of the melt pool with time was shown to be positive but non-linear. The growth rate of the melt pool on the surface seems to slow down as time progresses. i.e. the gradient of the graphs decrease.

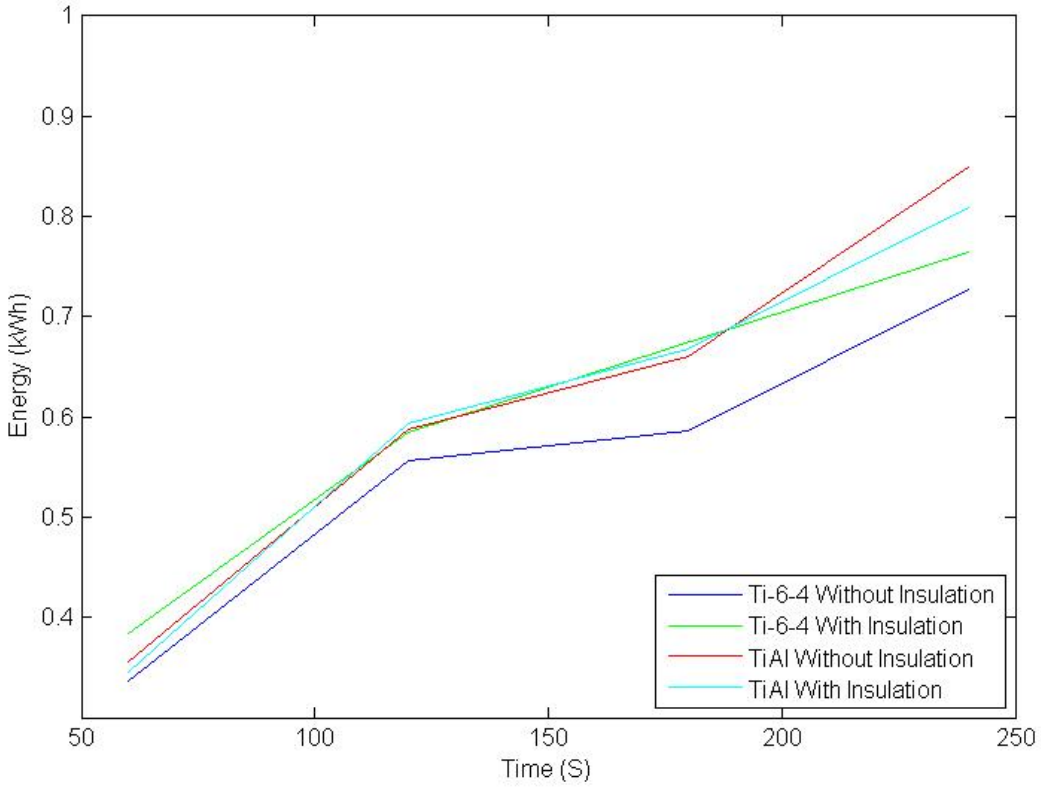

Figure 4.11: Effect of Insulation in the initial stages of Energy into a Melt Pool

4.1.4.2 Discussion

The results seen from the insulation experiment differ in part from those described by Mark Ward. It was found that once contact is made between the melt pool and the hearth, the effect of the insulation was not as evident (at least in the case of the TiAl melt). There are two theories that can be put forward as the reason for these results.

Firstly it may be inferred that the majority of heat is lost through the sides of the hearth rather than the bottom. Given that the insulation was only covering the bottom of the skull it would therefore not be as effective. In addition to this as the melt pool grows the effects of radiation as heat loss mechanism increases, which decreases the significance of the effect of the insulation. Finally the shape of the melt pool has not examined and it may be

possible that having insulation on the base may comparatively increase or decrease the melt pool depth.

These results suggest that for insulation to be useful at increasing the melt pool size two conditions should be met. These are to either put insulation on the sides and bottom of the hearth or preventing the melt pool from having contact with the sides of the hearth. This would also prevent liquid metal from being able to flow easily between the skull and hearth or prevent heat loss from the sides and spillage respectively.

4.1.5 Alloy

4.1.5.1 Method

Two alloys were looked at for this experiment, Ti-48-2-2, a Titanium Aluminide intermetallic, and Ti-6-4, a commonly used Titanium alloy. They were chosen due to their present and future use in high and low temperature sections of the aerospace engines respectively. Due to the lower liquidus temperature of TiAl, it is expected that a larger melt pool size will be formed given the same power input. However as discussed in the literature review the differences between the two alloys are much more complex than that. A skull of each alloy was made for this comparison, and melted first without and then with insulation.

4.1.5.2 Discussion

There are four variables that affect the minimum energy required to form a melt pool that differ between two alloys. These are: Specific Heat Capacity, Cp; Thermal Conductivity, K, the Solidus Temperature, T_{SL} and the density, ρ. Figures 4.8-4.11 show the different behaviour of TiAl and Ti-6-4 when heated. The results show that the alloy properties have an effect on the size of the melt pool achieved, as larger melt pools were seen for TiAl than Ti-6-4. This agrees with other research that suggests if a liquidus temperature is between 1873-

1893 K unmelted metal can be found [67], although this was observed in VAR where residence times are thought to be lower.

Insulation only seems to have an effect on TiAl during the early stages of the melt (Figure 4.10 and 4.11). This is because at this time the melt pool is in close proximity to the torch and heat transfer may be dominated by conduction and convection directly from the torch. Although as the melt pool grows the heat transfer is much more dependent on thermal conduction through the melt pool and skull. At this point the higher thermal conductivity of TiAl (as shown in Table 2.2) will allow heat to be conducted at a faster rate than in Ti-6-4.

Finally it can be seen that although there is a fairly large difference between the area of the melt pools for TiAl and Ti-6-4 alloys. However, the difference between the Energy for each alloy is much less. This is because the combined effect of Cp, T_L and ρ (and hence mass for a given volume) is greater for Ti-6-4. This suggests that to achieve the same melt pool size a higher amount of energy is needed to melt Ti-6-4.

4.1.6 Anomaly

Whilst processing the results for the trial (details shown in row 2 in Table 4.1) one video stood out as behaving differently to the others. As shown in Figure 4.8, the melt pool suddenly decreases in size approximately 2.5 minutes into the melt.

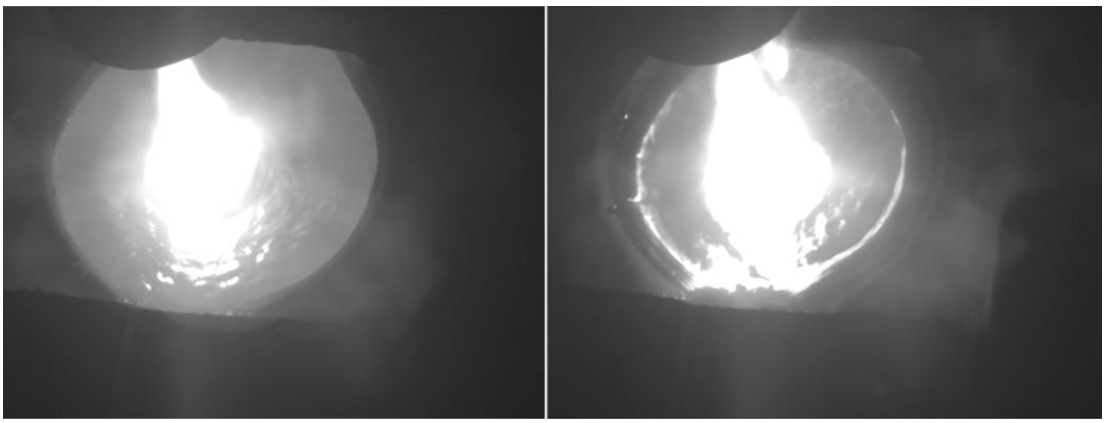

a **b**

Figure 4.12: Showing the melt pool shrink during a melt of insulated Ti-6-4 at a current of 550 A. There is a time difference between the two frames of 17 seconds.

The reason for this shrinkage is likely to be caused by a leak in the skull allowing liquid metal to flow into the gap between the skull and the hearth. By examining the video it could be seen that this shrink occurred just after the melt pool reached the side of the skull (the bottom edge of the picture in Figure 4.12), suggesting it flows over the edge.

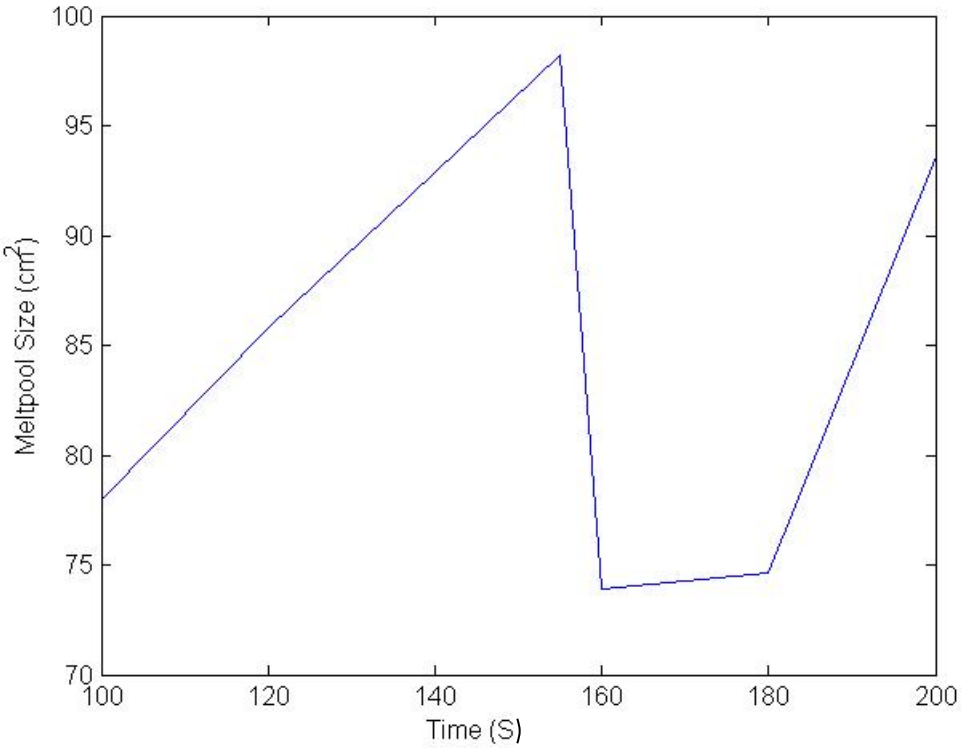

Figure 4.13: Change in melt pool area over time for the anomaly melt

This ‘anomaly’ is not an uncommon occurrence in the melt and can lead to decreased efficiencies as it reduces the volume of the melt pool. This causes a decreased residence time and highlights one limitation of the cold hearth in PAM. In a normal melt the torch is moved in a computer controlled pattern, or by the operator, as discussed previously. Great care has to be taken to not melt the solid skull during this time by not allowing the torch to get too close to the skull edge, as well as maintaining a good water flow in the hearth.

Two areas of future work can be identified from this, one is to gain a greater knowledge of the water flow rate in the hearth and how that effects melting and the other is to investigate better torch patterns. Both of these are discussed in more detail in the ‘Future Work’ section of this thesis.

4.1.7 Limitations of visual experiments

As a whole these experiments gave an idea of how the melt rate is affected by different variables. The most obvious limitation is that they indicate only the change in the area of the melt pool surface. In addition to this it should be noted that these results only show a small part of what is happening. For instance they say little about the temperature in the melt pool (only that it exceeds the liquids temperature) or the temperature gradient. Which limits its use as a method for looking at the dissolution of TiN which is very temperature dependent [67]. They also give little idea to how localised the effects of variable changes are. For instance a change in the arc length is not likely to be felt by the copper hearth. However an increase in the torch current will, as the current will be conducted out of the skull through the hearth. Finally they do not show how the variables interact with one another. R.Knight, 1991, [71] suggests that the arc length does not play such a large role at higher torch currents.

The estimation of energy input into the melt pool did to some extend negate these limitations i.e. they made it easier to compare the experiments and give an indication to the interaction of the variables. For instance it is possible to say that the specific heat of the alloy being melted matters more than the existence of insulation.

5) Sensors

5.1 Background Theory

As described in the introduction section, the plasma torch is used as a power input to melt the feedstock. During melting the torch transfers both electrical and thermal energy to the metal causing the temperature of the metal to rise and, once liquid has formed, fluid flow to occur. However not much is known as to the interaction between the torch and the surface of the metal, or how the heat and electrical energy is transferred through the plate. Some idea as to what may happen can be gained by looking at the physics behind the processes.

5.1.1 Thermal and Electrical Theory

When the torch is applied the main form of heat transfer from the torch through the metal is via conduction. Radiation and convection can be assumed to be negligible [99] and at this stage in the research will not be considered as their effect is felt mostly at the surfaces. The conduction of a heat through a material can be described by the rate of heat transfer, Q, using the Equations in Table 5.1

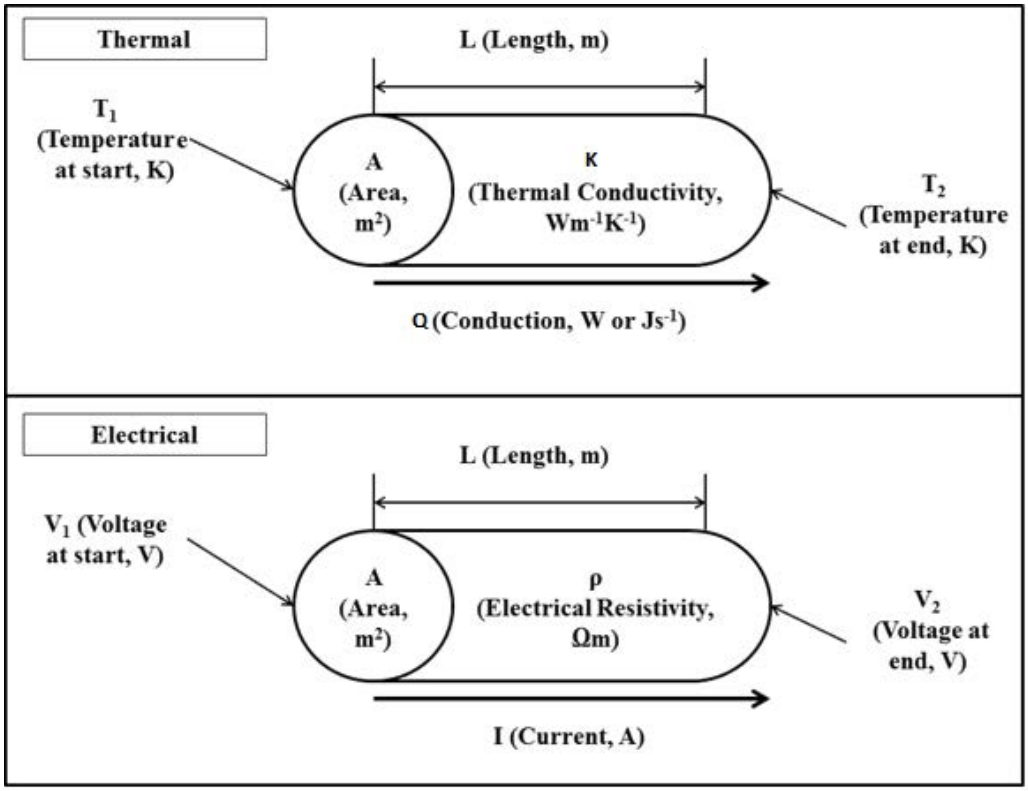

Figure 5.1: Diagrams showing the Thermal (Top) and Electrical (Bottom) conduction through a wire

Table 5.1: Comparison of Equations for thermal and electrical conduction

Temperature	Electrical
$\Delta T = QR$ Equation 5.1	$\Delta V = IR$ Equation 5.3
$R = \frac{L}{kA}$ Equation 5.2	$R = \frac{L\rho}{A}$ Equation 5.4
$Q = KA\frac{T_1 - T_2}{L}$ Equation 5.5	$I = \frac{1}{\rho}A\frac{V_1 - V_2}{L}$ Equation 5.6
$Q' = \frac{q}{A}$ Equation 5.7	$J = \frac{I}{A}$ Equation 5.8

The rate of heat transfer, q, describes the rate at which heat is transferred in a given period of time, however it is sometimes more useful to refer to the heat transfer rate per unit area. This is known as the heat flux, Q'. Using experiments, such as that described below heat flux can be calculated providing that temperatures T_1 and T_2 can be ascertained, and that the dimensions are carefully recorded.

The flow of electricity follows a similar set of equations whilst in steady state (as shown in Table 5.1). In a similar way to temperature, if the two voltages are known it is possible for the current to be calculated. From this the current per unit area, known as the current density (J) can be calculated as shown in Equation 5.8.

It should be noted that Equation 5.5 and Equation 5.6 assume the material properties, k and ρ are constant with temperature, however for most metals this is not the case. For some metals, such as constantan, the effect of temperature is negligible, however temperature changes can have a significant effect on ρ for Ti-6-4[100].

These Equations form the back bone of the majority of models that look at flow of electrical charge and heat energy through a material as well as the basis for the experiment described in the modelling and method section.

5.2 Method

5.2.1 Embedding thermocouples and voltage wires in the plate

The sensors experiment used a Ti-6-4 plate with the dimensions 300x260x25 mm. There was no surface treatment carried out on the plate before the experiment although dirt was removed using acetone and water. Sensors were placed vertically into holes from the bottom in a plate of ti-6-4. This meant the measurements they took represented the temperature and voltages approximately 20 mm from the top surface of the plate at different horizontal positions. The position of the tip of each sensor was carefully recorded (Figure 5.2) in order for the data to be used later in models. The proximity of the plate and thermocouples to the hearth was also recorded (Figure 5.3).

It was identified that as the temperature of the plate increases it will expand, causing the thermocouples and voltage wires to no longer be in contact with the metal surrounding it. This would lead to errors as, if a gap was to form, then the thermocouple would be reading the temperature of the air in the hole and not the plate itself. To combat this, a spring loading system was used to ensure the wires remained in contact throughout the experiment.

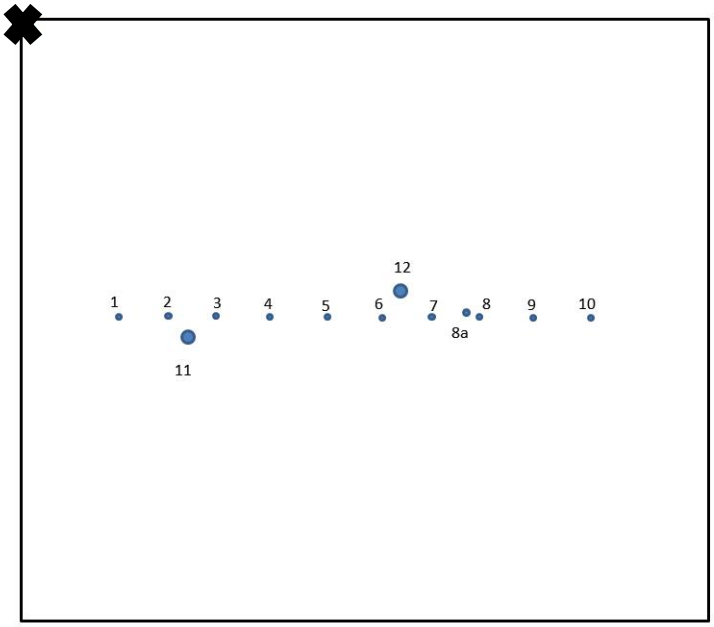

Co-ordinates (Origin should as point x)

Number	Position
1	(40.97, 132.41)
2	(66.1, 131.27)
3	(92.20, 132.65)
4	(117.55, 132.69)
5	(141.62, 131.69)
6	(165.99, 133.59)
7	(191.38, 133.34)
8a	(215.84, 133.84)
8	(217.86, 134.05)
9	(239.87, 133.99)
10	(164.28, 135.21)
11	(78.47, 145.99)
12	(181.35, 116.25)

Figure 5.2: Showing the exact locations (in mm) of the voltage and thermocouple holes as seen from above

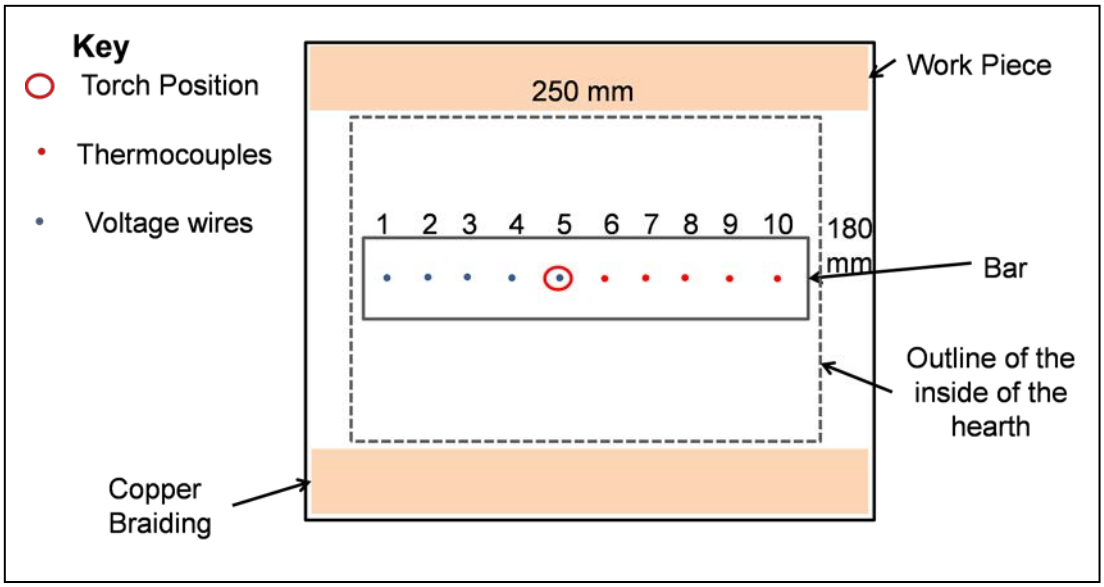

Figure 5.3: Schematic of the bottom surface of the Ti-6-4 plate looking up through the bottom surface of the hearth

5.2.2 Thermocouples

To take measurements of the temperature in the plate type-K thermocouples have been used. Thermocouples work by connecting two dissimilar metals, in this case nickel-chromium (chromel) and nickel-aluminium (alumel), forming a hot junction and a cold

junction. For this experiment the cold junction was within the data logging box and was at approximately room temperature, whereas the hot junction was placed in a drilled hole in the plate. The differences in the temperatures between the two junctions cause voltages (in the region of mV) to be produced that were recorded and later converted to temperature readings. Due to current flowing through the plate whilst the torch is on there is a possible error (see Appendix A), although this was found to be relatively small.

Thermocouples have a range of temperatures in which they can operate. For a Type-K the maximum temperature it can operate under is 1150°C, therefore for the first trial it was decided to only apply the torch for a few seconds so it can be repeated at little cost if necessary. Consequently small response times for the thermocouples were vital for this experiment and small diameter (1mm) thermocouples were used. Ungrounded thermocouples were used due to their easy availability at the time of the experiment. For this arrangement the thermocouple wire is isolated from the sheath leading to potential longer response times that the grounded counterparts, although they were found to still be low enough for this experiment (approximately 0.33 seconds).

5.2.3 Voltage Wires

The voltage readings are recorded using multi-stranded copper wire; copper was chosen due to its good electrical conductivity. Multi-stranded wire is more ductile for the same diameter than single stranded wire. As noted previously the voltage difference is needed to calculate the current. Therefore the wires are setup in such a way to measure the difference between themselves and wire nearest the edge of the plate (approximately 10 cm from the torch, Position 1 in Figure 5.2). The wire was sheathed in glass fibre to stop it from making electrical contact with metal parts in the furnace. Glass fibre was chosen in particular due to

its high melting point. It was exposed only at the tip where it enters the plate to give good contact with the plate.

5.2.4 Set-up in the furnace

Once assembled the plate was placed on top of the hearth with copper braiding along two edges of the hearth (as shown in Figure 5.3 and Figure 5.4). The point of this was to create two clear areas of contact between the hearth and the plate. In this set-up the hearth acts as a heat sink and as a path for current to flow. Two multi-pin 40 mm Klein Flange (also known as a Quick Flange) feedthroughs were used to take the wires from the inside of the furnace to the data logging box on the outside. Great care was taken to clearly label all wires so it was known which channel in the data logger refers to which position in the plate. Both of the feedthroughs used copper wire, this may be considered a source of error for the thermocouples, however was thought to make little difference providing the wires on either side of the furnace remained at similar temperatures. The number of pins had to be kept to a minimum given the small diameter of the port leading from the inside to the outside of the furnace. The length of the internal pins were checked for before the day of the experiment to ensure they were long enough to pass through the hole in the furnace whilst not being exposed.

The torch first had to start on the strike off block, shown in Figure 5.4, once stable it was moved into position to the centre of the plate. Trial runs were carried out with the torch turned off in which the torch was moved by a distance set by the controller until the final location of the torch was as close to the centre of the plate as possible.

For this experiment a current of 600 A was used at a voltage of 150 V; a gas flow rate of 12 ft^3/min and arc length of 67 mm. These readings are based on the numbers indicated on

the equipment and therefore are all approximate as error varies depending on the calibration of the built in sensors.

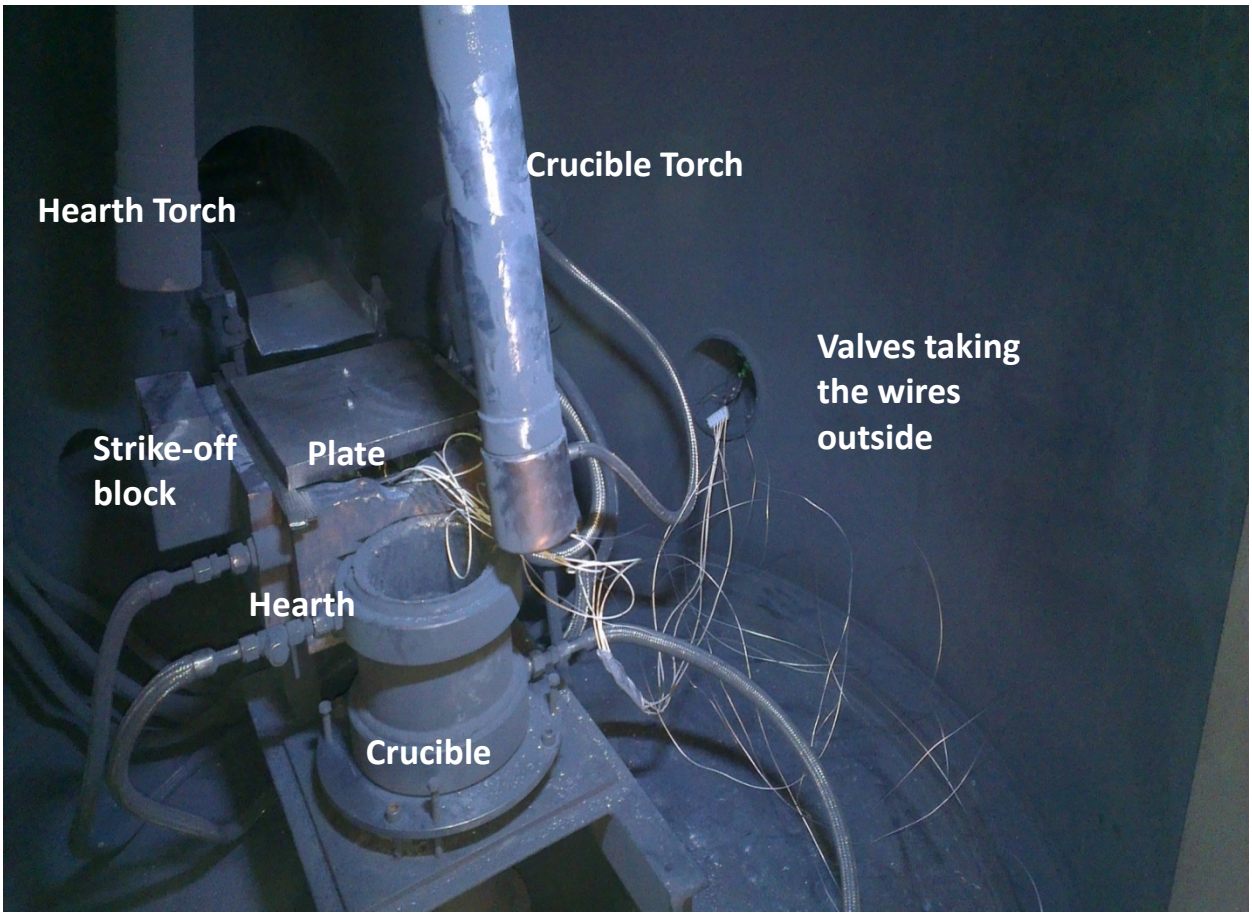

Figure 5.4: Photo showing the set-up of the plate inside a large plasma furnace.

5.3 Results

Despite being checked beforehand and handled with care, two thermocouple wires once set-up in the furnace, were found not to work. Time limitations for access to the furnace prevented the connections being fixed before the melt giving only three temperature readings.

The initial observations of the experiment are shown in Figure 5.5 and Figure 5.6. As mentioned the plasma torch must was first turned on over the strike-off block, shown in Figure 5.4, and then moved across the plate into position. By examining the resultant melt

pool on the plate it can be seen that the torch moved approximately 13 cm (the distance between A and B in Figure 5.6).

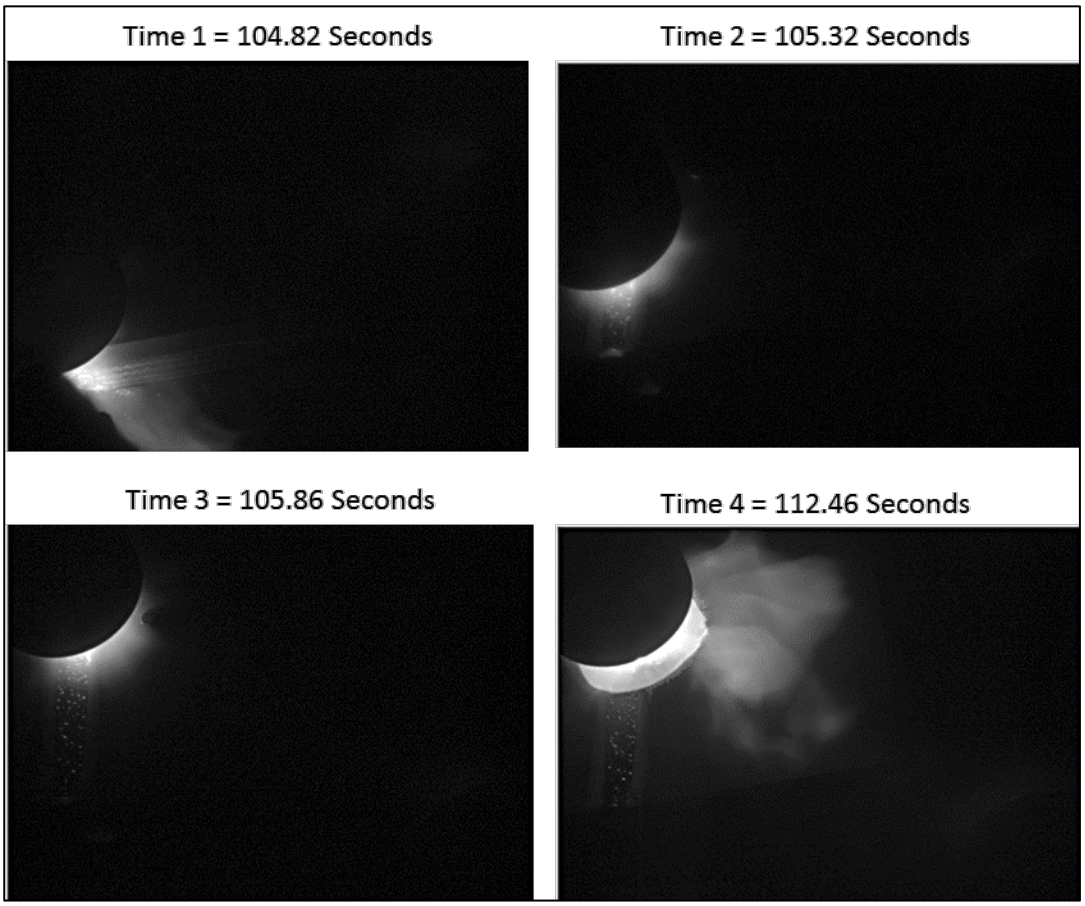

Figure 5.5: showing the torch starting at the strike off block on the edge of the plate (Time 1), across to the centre of the plate (Time 2 and Time 3) where it remained for 6.6 seconds before being turned off.

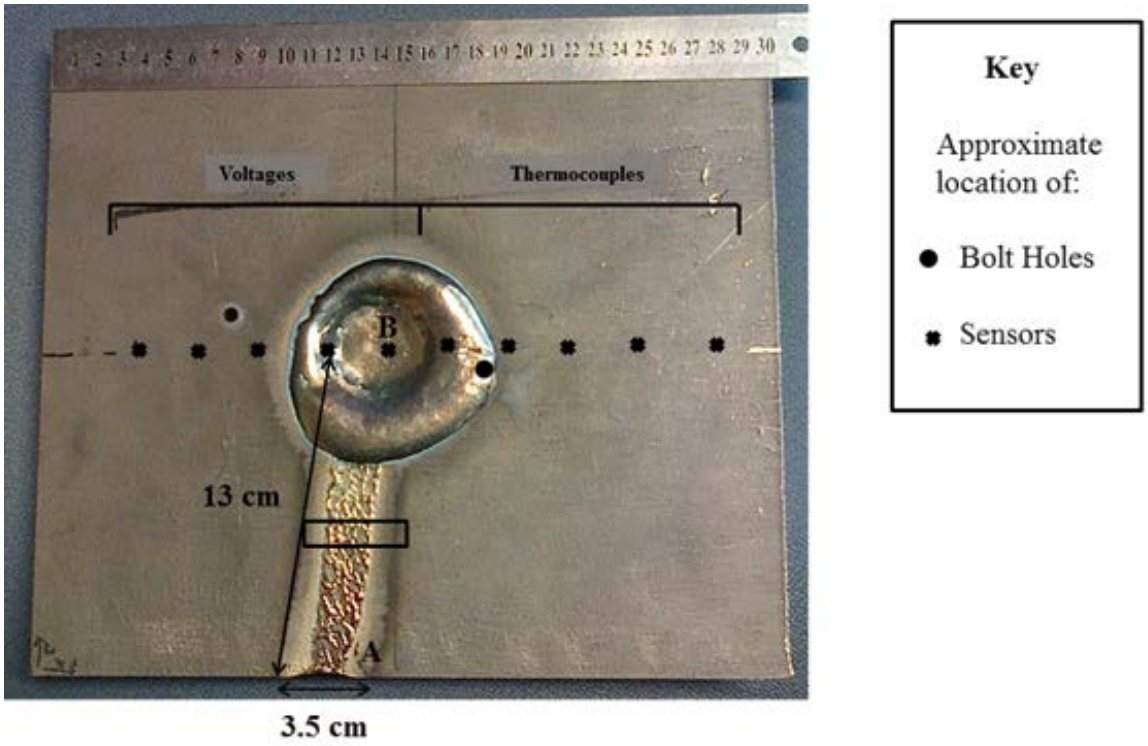

Figure 5.6: Plate after the plasma torch has been applied

The torch remained stationary in the centre of the plate for 6.6 seconds (Time 3-Time 4 in Figure 5.5) where a melt pool was formed with a diameter of 8.3 cm. The middle of the melt pool lies directly above a voltage wire. The nearest bolt, used to support the spring loading system, had been melted into the plate. This and the second steel bolt in hindsight may cause a disruption to the conduction of heat and current through the plate due to its different properties relative to titanium.

5.3.1 Voltage experiments

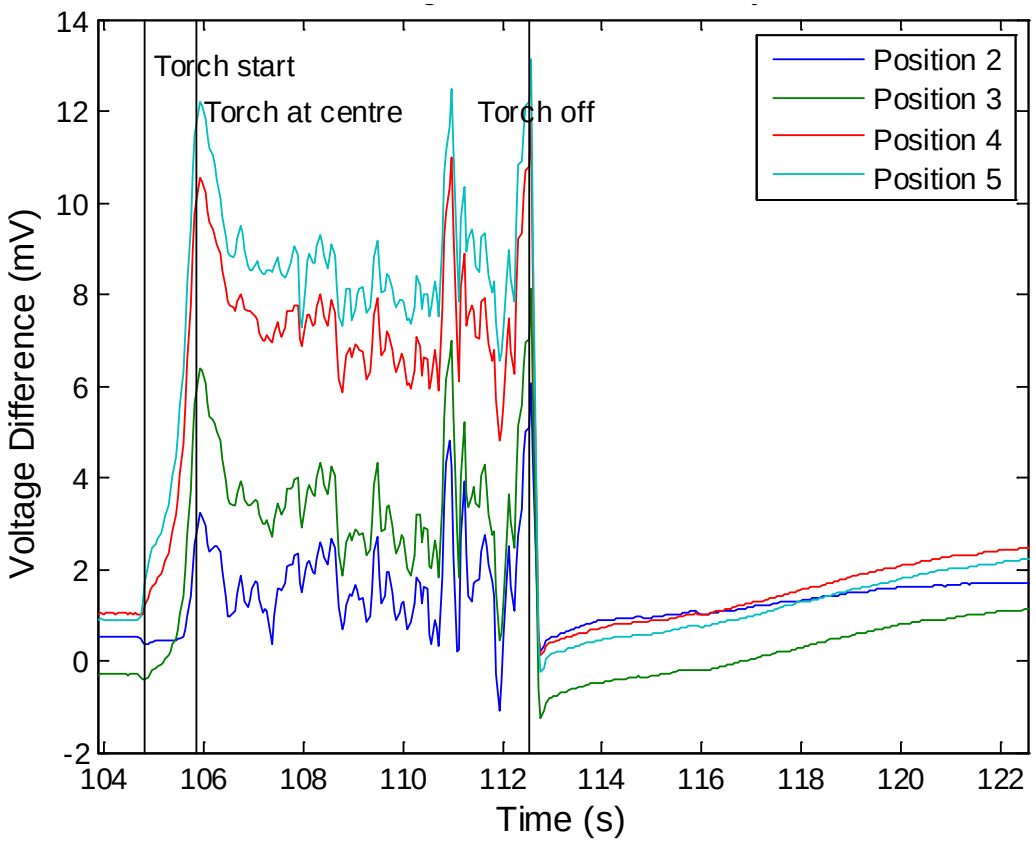

Figure 5.7: Graph of the data collected from the voltage wires whilst just before, during and after the plasma torch was on

Unlike the temperature readings the voltages are shown to change as soon as the torch is switched on, as shown in Figure 5.7. In general the voltages recorded through each wire rise as the torch moves closer to them; are maintained during the period that the torch is stationary and fall quite rapidly once the torch has been switched off. Position 5 is nearest the centre of the plate and as shown in Figure 5.3 is located directly under the plasma torch. At this point the highest voltage difference can be seen suggesting that it drops from the centre to the outside edge of the plate.

5.3.2 Thermocouple Experiments

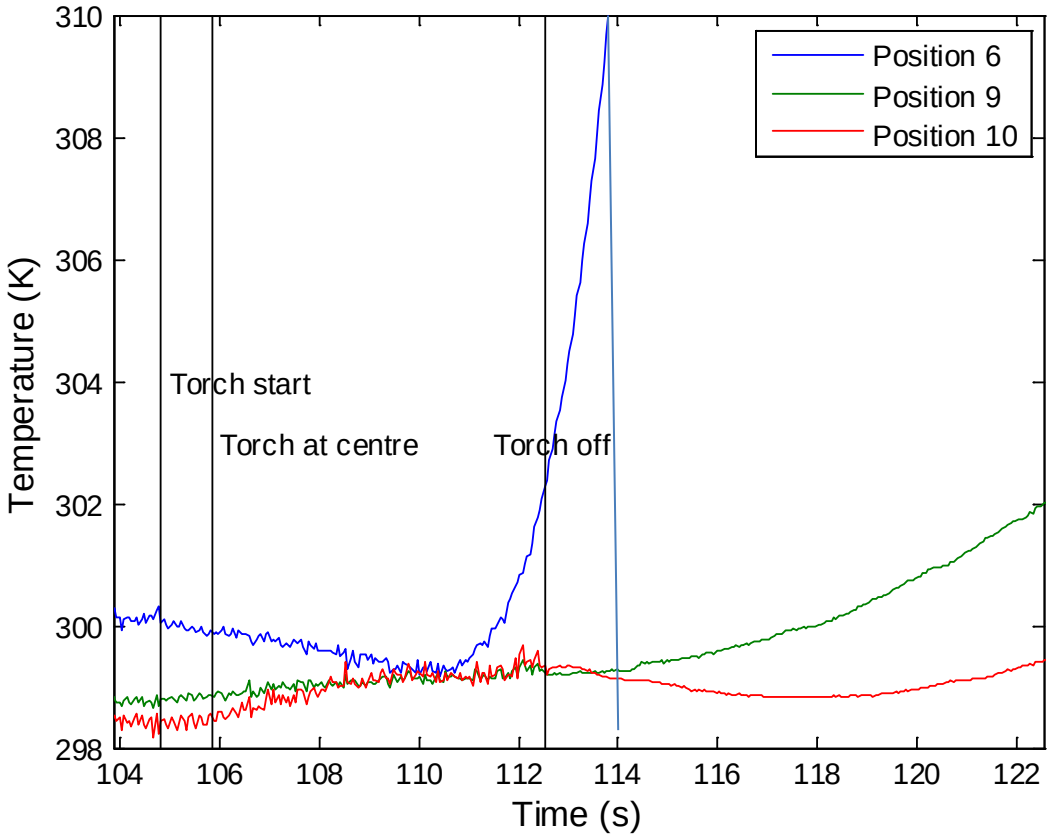

Figure 5.8: Graph of the data collected from the thermocouple whilst just before, during and after the plasma torch was on

When the torch is initially turned on little effect is seen by the thermocouples, this is because at this stage the torch is still relatively far away from them. Position 6, as shown in Figure 5.3, represents the thermocouple that was located closest to the plasma torch. This thermocouple was the first to respond to the rise in temperature taking approximately 4 seconds. The thermocouples in positions 9 and 10 took approximately 8 and 11 seconds respectively. This suggests that the heat from the torch took time to be conducted horizontally through the plate. At each position the rate at which the temperatures rise can also be seen to be different, suggesting that the heat energy was more widely dissipated by the time it reached the outside thermocouples. Finally the highest temperatures reached decreased as the

thermocouples positions got further out from the torch. This follows the expected temperature distribution shown in Figure 5.9.

5.4 Discussion: Current Density

5.4.1 Background

One of the main purposes of measuring the voltage in the plate was to then calculate the current density in the plate at these points. Figure 5.9 shows a schematic of the possible patterns that may be found for the current density and heat flux when the torch is applied to the surface of the plate. Literature suggests [71], the heat energy is found to be concentrated in the area corresponding to the centre of the torch plume.

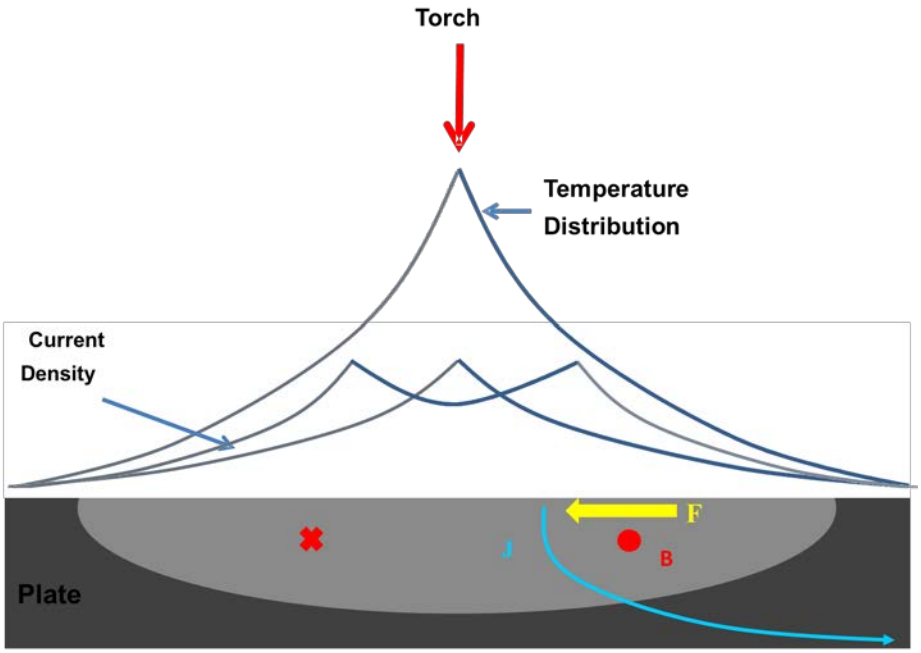

Figure 5.9: Possible current distributions in the torch a) one peak [38] and b) two peaks [2] with the effects of the melt pool

$$\underline{F} = \underline{J} \times \underline{B}$$ **Equation 5.9**

The plot of current density could take one of two shapes. It was originally thought that, like temperature, the current density would peak at the centre of the torch plume and have a gauss distribution [86]. However some research suggests that the current density in fact has two peaks nearer the edges of the plasma plume [2].

Both the current density and temperature distribution influence the liquid flow within the melt pool. The current density interacts with the magnetic field causing Lorentz forces to be produced. This leads to a flow of liquid metal to form as it rises up towards the peak in current density. Consequently the orientation and location of the peak in current density has an effect on the mixing within the melt pool. A temperature gradient within the melt pool causes buoyancy flow that can oppose the flow caused by the Lorentz force.

An analysis of these combined effects was done to give an indication as to which were the predominate mode of flow in the melt pool. It was assumed that the flow caused by the changes in surface tension is negligible [36]. Although not completely accurate, it allows the Lorentz and buoyancy forces to be directly compared.

It was found that the Lorentz force was approximately 15 N m^{-3} stronger than the Buoyancy force using Equation 5.9. This is assuming the density changed from 4200 to 4100 N in the hot and cold regions (just below the solid density of Ti-6-4, 4430[57, 58]) and that the torch current was 650 A and evenly distributed through a cylinder of 3 cm diameter. Using these details the two graphs below were formed.

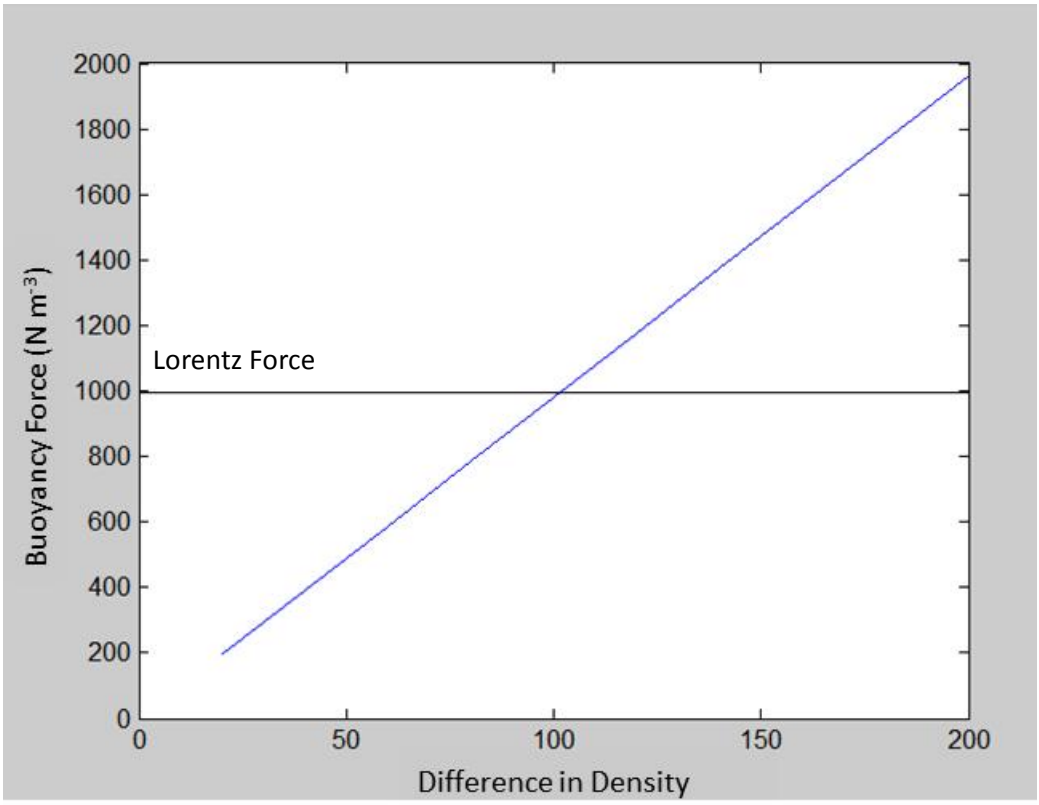

Figure 5.10: Change in Buoyancy Force with Density

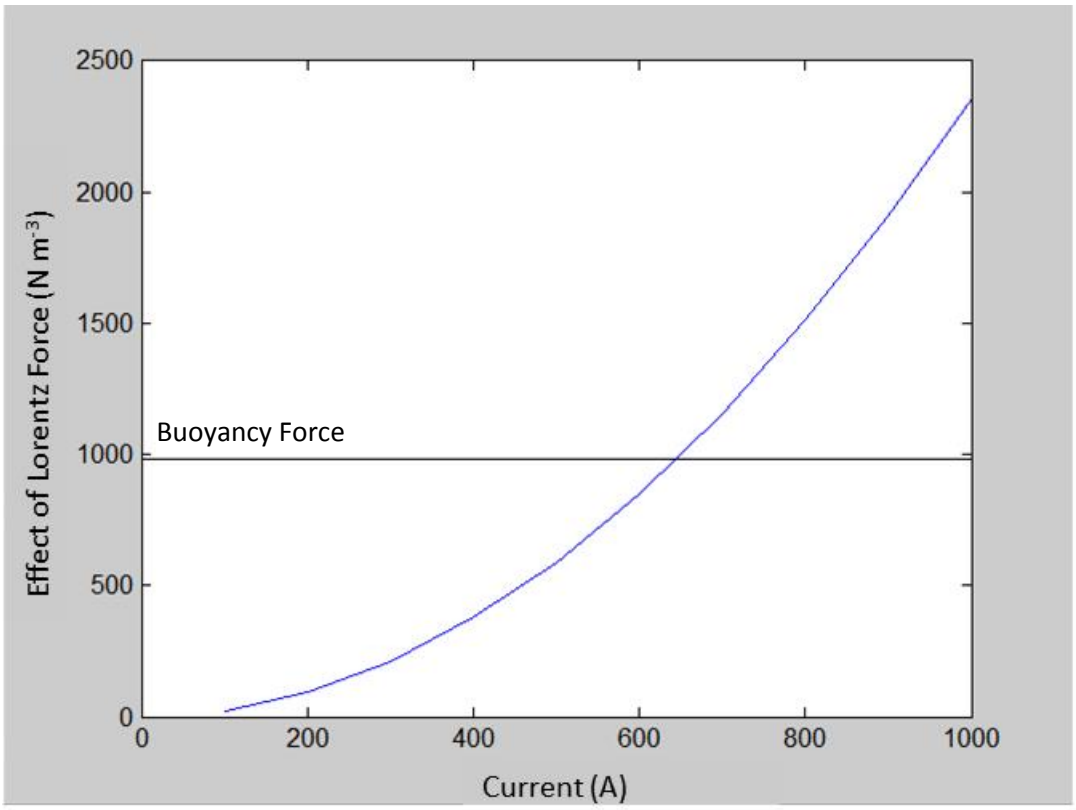

Figure 5.11: Change in Lorentz Force with Current

Figure 5.10 shows that if a current of 650A is assumed (shown by the horizontal line in Figure 5.10); the density difference must be greater than approximately 100 for the Buoyancy force to be stronger than the Lorentz force. Similarly the current must be above approximately 650A for the Lorentz force to be stronger than the Buoyancy force (Figure 5.11). This is if the density difference was assumed to be 100, giving a buoyancy force of 980 (shown by the horizontal line in Figure 5.11).

These graphs also show the positive relationship between Lorentz force and current (Figure 5.11) as well as the positive linear relationship between Buoyancy force and density difference (Figure 5.10).

5.4.2 Voltage Results

From the voltage readings (shown graphically in Figure 5.12) the current density, J (A/mm^2) in the plate can be calculated. The calculation of J is based on Ohms Law, shown in Equation 5.10 [1, 38, 39, 89].

$$\boldsymbol{J = -\sigma_e \frac{\delta V}{\delta x}} \qquad \textbf{Equation 5.10}$$

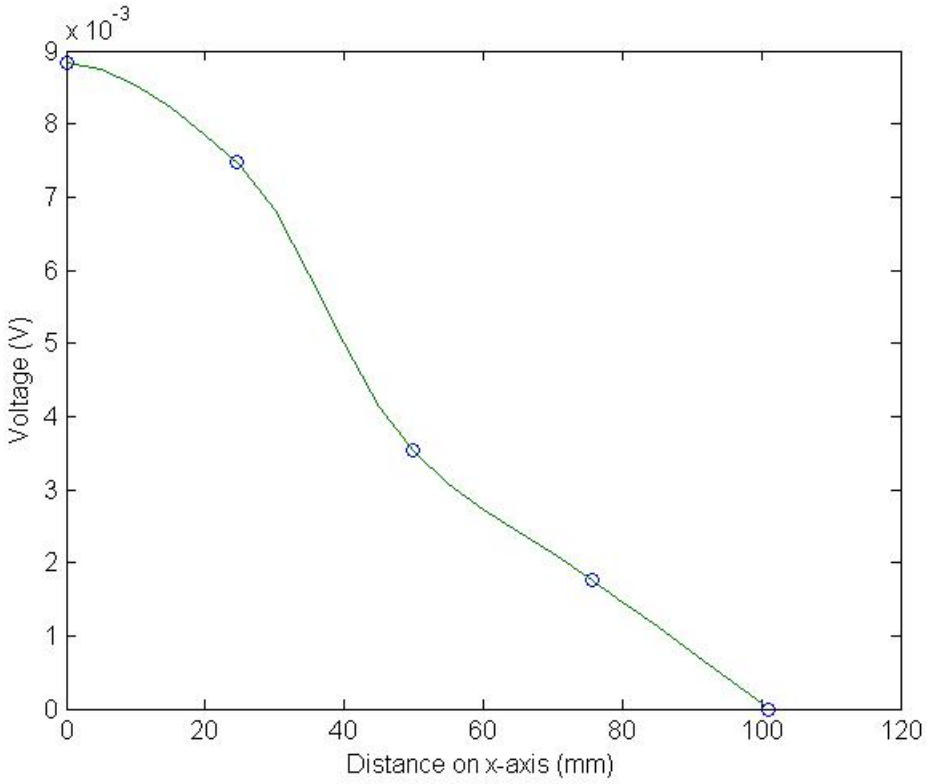

Figure 5.12: Mean Voltage with distance on plate

5.4.3 Voltage and Current Density Models

5.4.3.1 2D Model of Plate

First a simple analytical model of a 2D, axi-symmetrical, cylindrical plate was carried out using MATLAB. It assumes all of the current enters the plate in the centre and leaves plate along the outside edge.

As described previously, electrical current flows as a result of a voltage difference in the plate. This model aims to access the voltage difference across 'cells' in the plate. The voltage difference can be calculated if the following are known: the area through which the current must flow (m); the thickness of the section (l), the resistivity of the plate (ρ) and the value of the current (I). It should be noted at this stage that the value of ρ is temperature

dependent. Grong[50] evaluates the limitations of a model in which a temperature independent value is used and concludes that, although the assumption of constant variables can be ‘unrealistic’, the error can be reduced by using a reasonable average. For this reason, to maintain the simplicity of the following model, an average value for resistivity will be used.

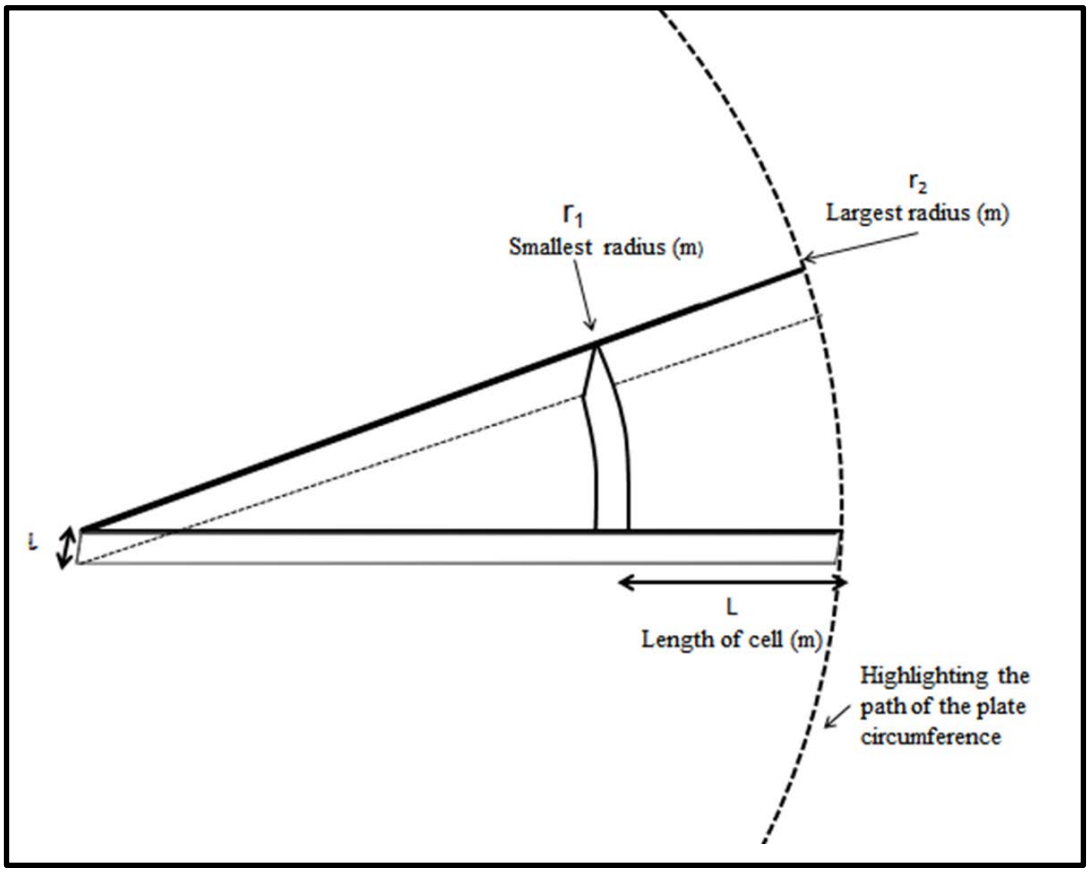

Figure 5.13: Diagram showing the basis for the analytical model

The model is based on Equation 5.2, Equation 5.4, Equation 5.11 and Equation 5.12, rearranged to make the resistance of the subject (Equation 5.13). The resistance changes from the centre to the edge of the plate in relation to the change in area. A cylindrical co-ordinate system is used to allow for an even voltage distribution.

Equation 5.11and Equation 5.12 show how the area and length can be calculated in general terms for this set-up (refer to Figure 5.13). The resistance in the cells were integrated as shown by Equation 5.14.

$$\boldsymbol{A = 2\pi rl} \qquad \textbf{Equation 5.11}$$

$$\boldsymbol{L = dr} \qquad \textbf{Equation 5.12}$$

$$\boldsymbol{R = \int_{r_1}^{r_2} \frac{\rho_e dr}{2\pi rl}} \qquad \textbf{Equation 5.13}$$

$$\boldsymbol{R = \frac{\rho_e}{2\pi l} \ln\left(\frac{r_2}{r_1}\right)} \qquad \textbf{Equation 5.14}$$

By equating Equation 5.2 and Equation 5.14 it is possible to work out the voltage difference across each cell as shown in Equation 5.15.

$$\boldsymbol{V = I * \frac{\rho_e}{2\pi l} \ln\left(\frac{r_2}{r_1}\right)} \qquad \textbf{Equation 5.15}$$

Where r_1 and r_2 are radii and *l* is the depth of the disk section all with the unit of metres.

5.4.3.2 2D Model including Current Density

In reality the current does not all enter the plate in one central point and flows both vertically and horizontally, making a 2D model more appropriate. (referred to here as Model 2). When the plasma arc is applied to the plate the current from the arc flows down and into the plate resulting in a voltage difference between the edge and the centre. The amount of current that enters the plate in reality varies radially and is based on the current density of the plume at that point. This is an expansion of the theory discussed above in which all of the current is assumed to enter in one central place.

To consider this vertical current flow from the plume in the plate the current density from the plasma plume has to be looked at. This model starts by assuming values for the current densities entering the plate at points that correspond to where the voltage readings were taken for the experiment. i.e. at 0, 25, 50, 75 and 100 mm. As the outside edge (100 mm) was taken to have a voltage difference of zero, the current density will be assumed to be zero at this point. The current density (shown graphically in Figure 5.14) can then be used to calculate the current that enters that segment based on the segments area.

This vertical current flow is then added to the horizontal current entering that segment (made of the summation of the current from the previous segments) and used to calculate the voltage at that point. The model was implemented in two ways, using analytical and numerical integration methods in order to verify the results.

Ultimately the model takes current density values and produces voltage values for a plate of a given area and electrical resistivity. However, as the experiment is set-up to measure the voltage in the plate this model needs to be reversed so that the voltage can be entered to the model and calculate the current density. This ‘backward’ model uses a goal seek approach, adjusting the current density values until the measured voltage values are obtained.

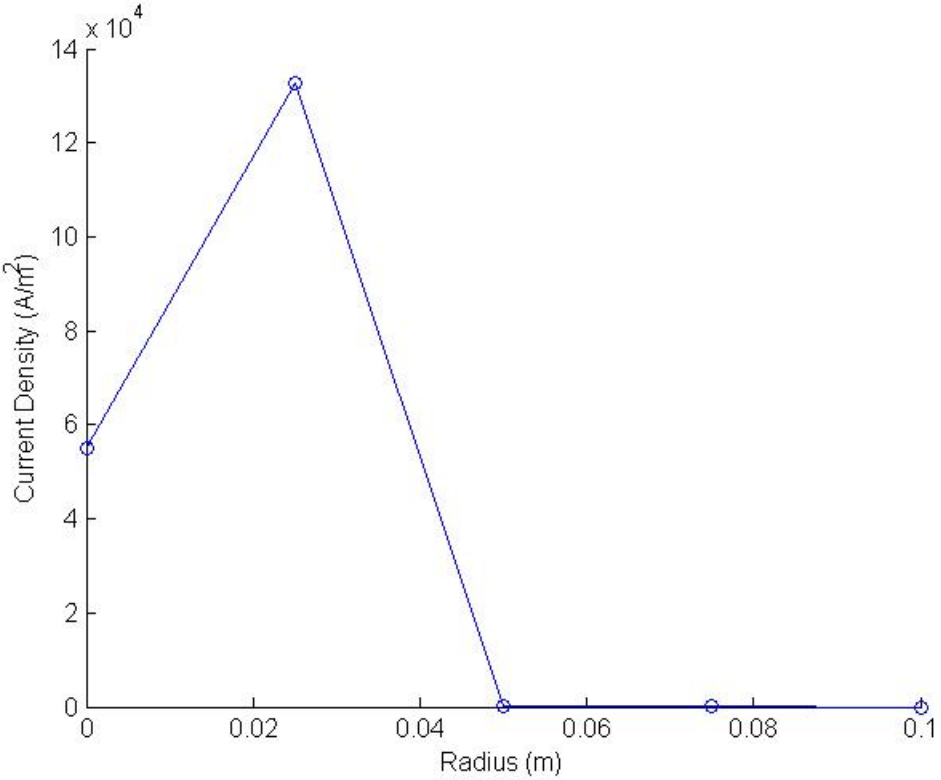

Figure 5.14: Change in Current Density with radius

The Current Density values shown from this model suggests that it is at its highest in at approximately 0.025 m and on average current density in the plume is approximately 90,000 A/m^2 (If only the first two higher current density readings are taken into account, assuming the others are outside of the plume). More points would be needed to properly ascertain where the highest current density lies, however it does support previous research discussed earlier that there are two peaks either side of the centreline of the plume (see Figure 5.9).

These results compare favourably with previous research (published in two separate papers by the same group), that used a CFD model of PAM, validated by experimental data. They found a peak in current density of $25x10^4$ [1, 2] and $39x10^4$ A/m^2 [1] at 36 and 25 mm from the plume centre respectively.

5.4.3.3 FEM Model

The third model of the plate used for comparison here was made by research fellow Bindu Nair [101] and used a finite element method to model a rectangular plate (Figure 5.15), with a set-up based on the sensor experiments (Figure 5.3). This model assumes the current enters the plate through a cylinder of copper (modelling the plume), 3 cm in diameter, that has an even current distribution. Copper was chosen as the material through which current was inputed as it is a good electrical conductor.

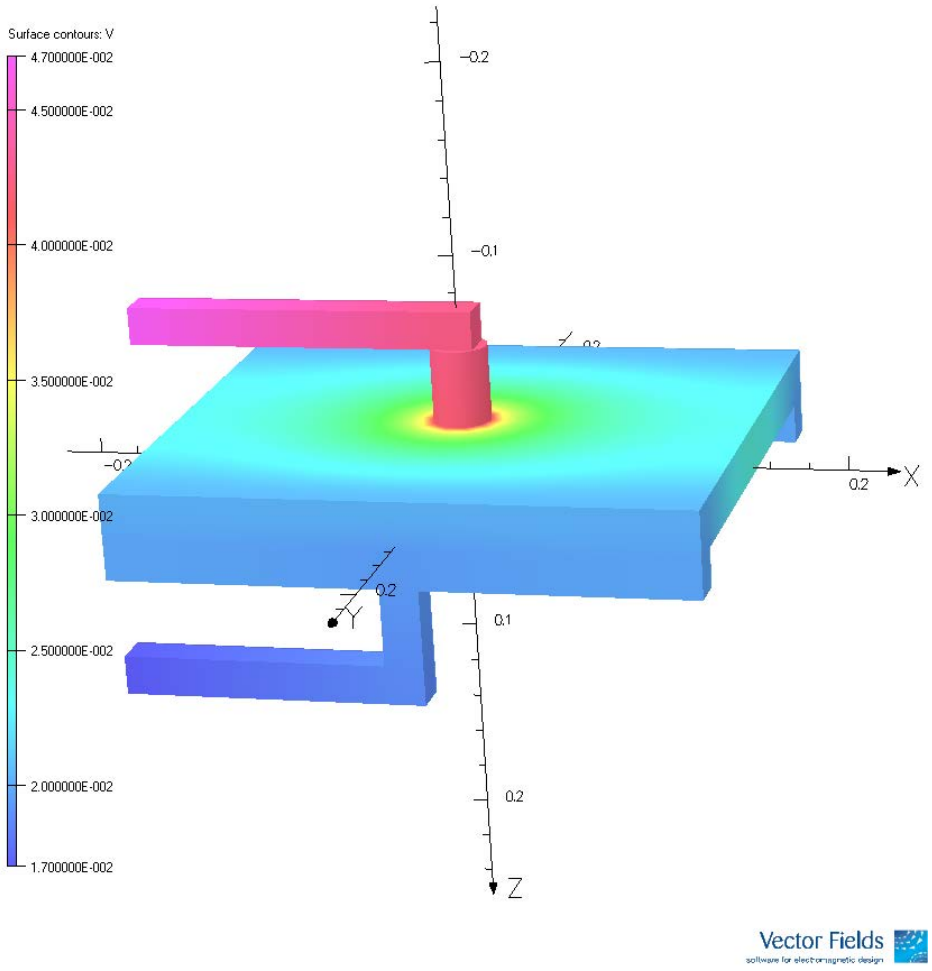

Figure 5.15: Model of the Plate using FEM [101]

One difficulty in modeling this situation is the presence of the hearth under the plate. The hearth increases the resistance felt by the current exsiting the plate. This meant it was not adequate to assume the current came out through the copper braiding strips only. Therefore strips of metal, significantly thicker than the copper braiding was used to represent the current output.

5.4.3.4 Comparison of Model and Experimental Results

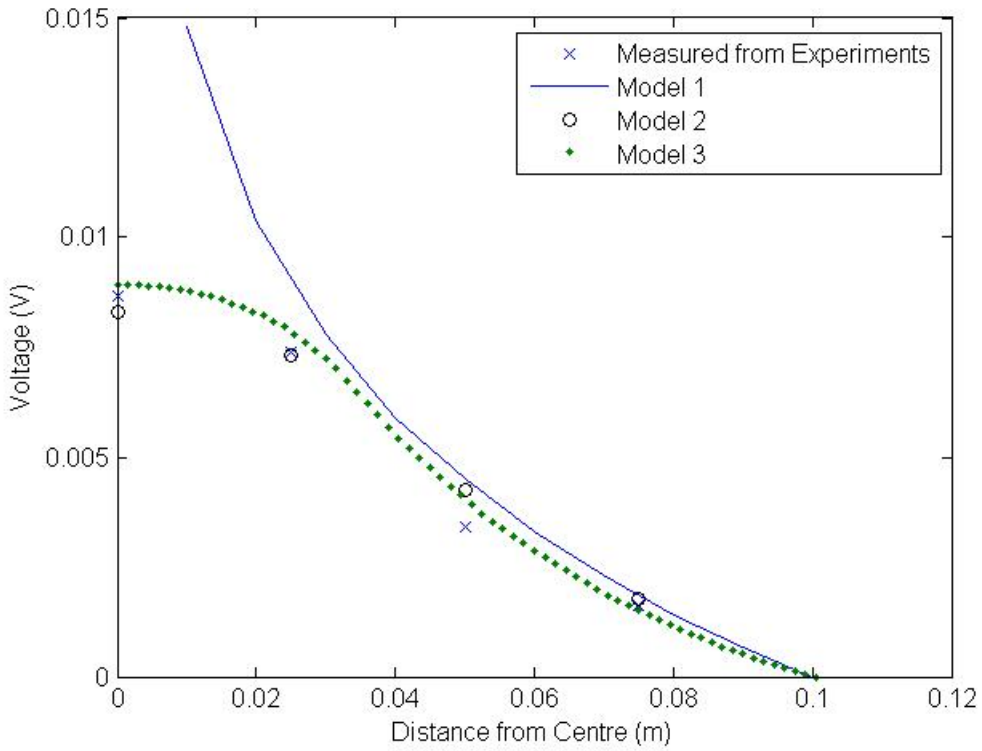

Figure 5.16: Comparison of the Voltage Difference data from the models and experiment

Model 1, 2 and 3 differ in the most part by the way in which the current is assumed to enter the plate and this can be seen in the resultant voltage readings. For example Figure 5.16 shows how all of the models match closely at higher radii (between 0.03 and 0.1 m). This is because in the outer regions of the plate the current has been distributed to such an extent that it doesn't matter at which point the current has entered. In the centre the difference between the models is more apparent.

The analytical model (Model 2), due to the assumption of an even current distribution, shows a smooth change in the rate of change of the voltage difference with distance from the torch centre. As may be expected this is not the case for Model 1 and 3, or experimental results, where the current is not evenly distributed. However the second model does not match the experimental data fully either. This is most likely due to the assumption that the plasma arc acts as a 3 cm cylinder containing an evenly distributed current not being completely accurate.

It is difficult to tell exactly what is occuring in the plasma plume during the experiment due to there only being 4 points, although some suggestions can be made as to what is occuring. The initial section of the experimental graph (before the change in the gradient of the line starts to even out) is steeper, less smooth and longer than that seen in the FEM model. This may suggest that the plasma plume is wider than assumed and has an uneven current distribution.

5.4.4 Lorentz Force Calculations

It has been discussed how the Lorentz force impacts the mixing and hence inclusion removal and homogenisation in the melt pool. The approximation of the Lorentz force value, shown in Figure 5.10 and Figure 5.11, suggests it is of equal scale to the Buoyancy force, however does not allude to its distribution. If enough of these measurements were taken it may be possible to calculate enough current densities to allow the Lorentz force in the plate to be calculated. Although with this data the only Lorentz force that can be calculated corresponds to the current densities heading vertically downwards into the plate i.e. it does not give any idea to the current density distribution.

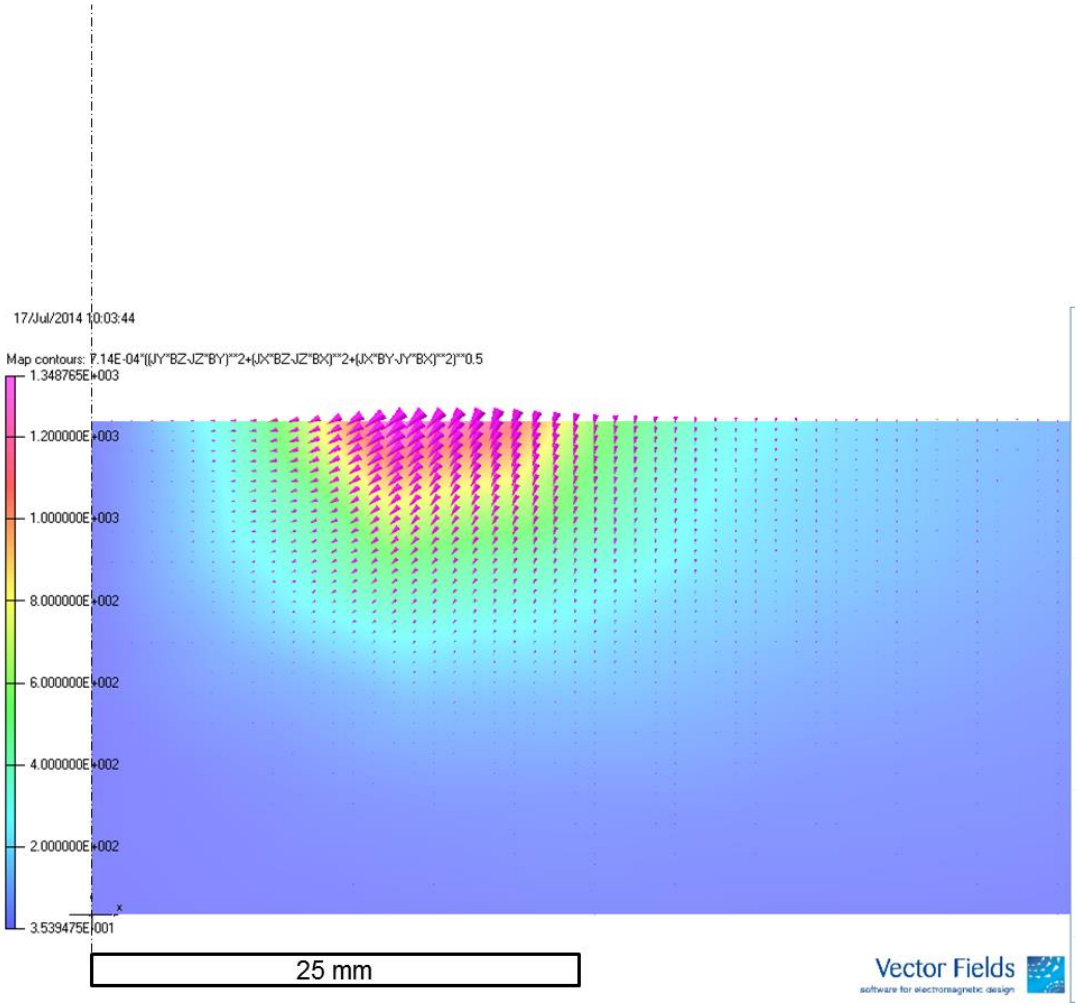

Figure 5.17: FEM model of the Lorentz forces in the plate using the voltage distribution and subsequent current densities calculated previously (Figure 5.15 [109])

This model (shown in Figure 5.17) allows the current to enter the plate in a series of cylinders of increasing radii (corresponding to the positions of the wires in the plate) within one another, similar to the calculations above. However it also takes into account the effect each cylinder has on one another (using the summation rule) and the path the current takes through the plate, assuming it all leaves through the edges. Finally by using a series of equations simultaneously the current is allowed to bend.

This model suggests a Lorentz Force of ~1350 N m^{-3}, 20 mm from the centre of the plume, acting downwards and towards the centre of the plate. These results agree in magnitude with the original estimate of the Lorentz Force and reinforce the theory that it is a

similar value to the Buoyancy Force (1000 N m-3). In addition it also shows that the Lorentz force is fairly localised corresponding to the point in the plume with the highest Current Density.

5.5 Discussion: Temperature in Plate

5.5.1 Initial Processing of data

Attempts were made to analyse the temperature results in a similar way to the voltages in order to give an idea of the heat flux. However as none of the points lie in the centre of the plume and there are only a small number of data points, the results would have not been accurate enough to be of use. Although the change in temperature with distance, seen in Figure 5.18 below does show how rapidly the temperature drops from the centre of the plate to the edges. The circles in this image mark the locations of the thermocouples; the data in between them have been interpolated to suggest the sort of curve that may be seen. The first point corresponds to the thermocouple in Position 6 (Figure 5.3), which was placed below the melt pool.

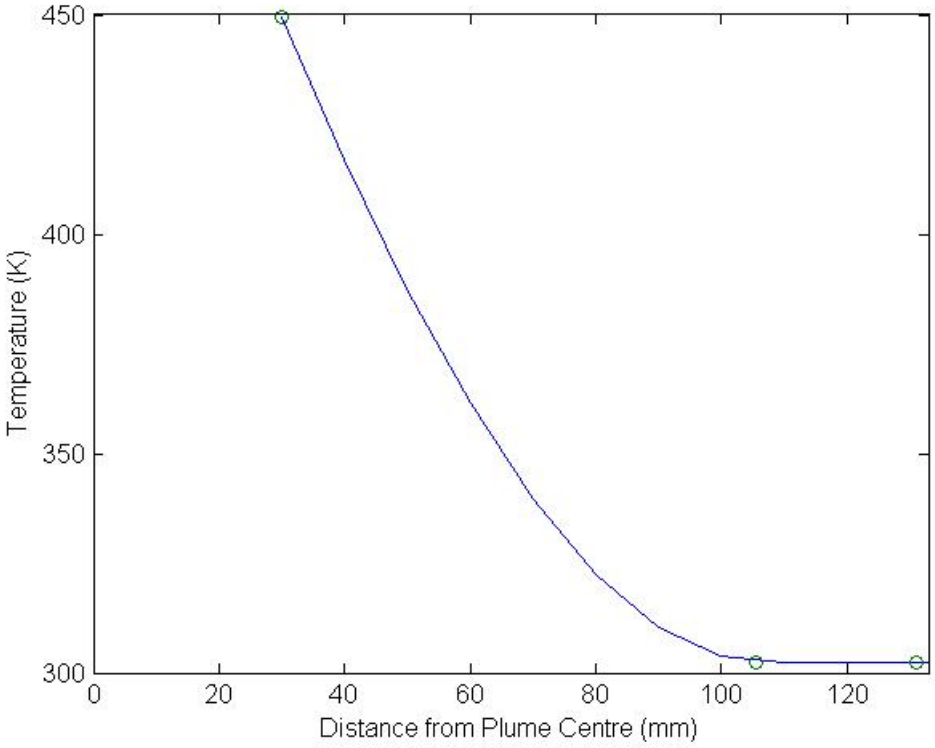

Figure 5.18: Change in temperature with distance based on the average of data recorded during and just after the plasma torch was on for each position.

5.5.2 Microstructure

In addition to the temperature measurement, a section was cut out using the EDM as shown in Figure 5.19. By looking at the melt pool microstructure it may be possible to estimate the temperatures in each region. The melt pool depth was observed and using data of the time the torch is over this area, an idea of the melt pool depth achieved in a given time could be calculated. For this the time was estimated from the velocity the torch moves over the surface.

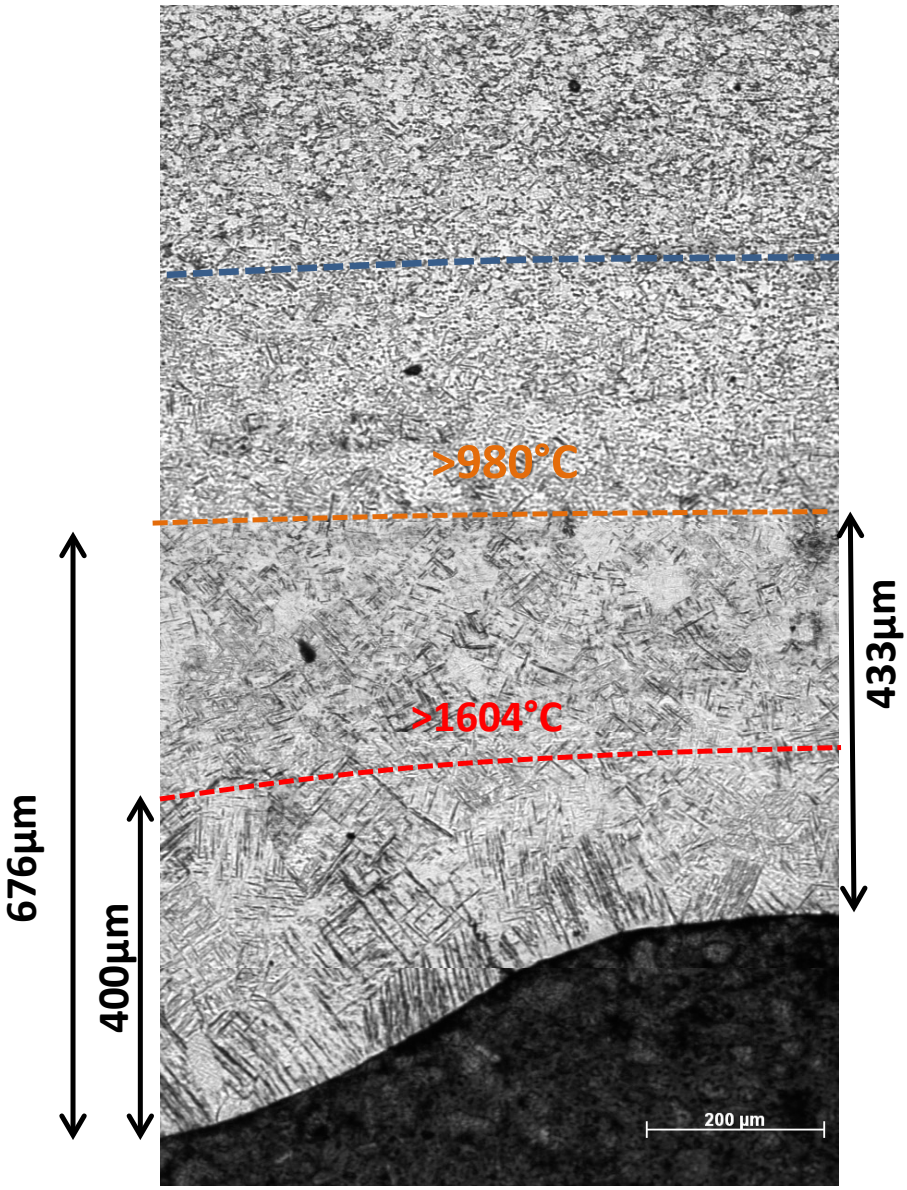

Figure 5.19: Optical Microscope Image of the microstructure from a cross-section highlighted by a box in Figure 5.6

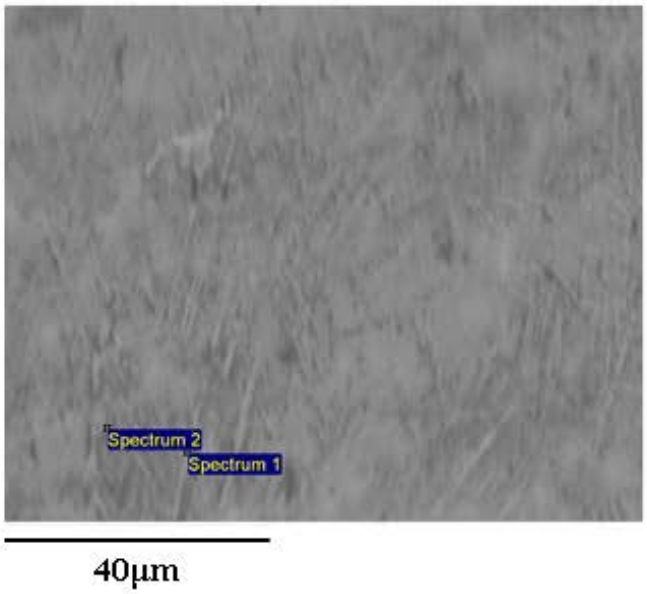

Element	Spectrum 1 Weight %	Spectrum 1 Atomic %	Spectrum 2 Weight %	Spectrum 2 Atomic %
C K	2.76	9.68	0	0
AL K	7.29	11.38	6.74	11.39
Ti K	87.42	76.85	90.15	85.82
V K	2.52	2.09	3.12	2.79

Spectrum 1 corresponds to the dark area

Spectrum 2 corresponds to the light area

Figure 5.20: SEM image of section and EDS analysis of the phases

Microstructural analysis of the plate gives an indication of the temperatures reached in the melt pool as the torch was moved across the plate. The torch was moved at 12 cm/s and assuming the torch plume is 3 cm in diameter, it can be estimated that the torch was applied to this section for 0.0025 seconds.

Once the section was polished and etched with a Kroll etchant, four different areas could be identified. The top of the image, shown in Figure 5.19, shows the bulk microstructure containing alpha and beta grains. Below the blue line the beta grains (shown by the lighter area) can be seen to be larger than in the bulk (changing from microns to tens of microns). This suggests that during the melt the α+β phase field was reached and upon cooling beta was retained. Below the orange line it appears that the microstructure now consists of acicular alpha needles in a beta matrix suggesting that in this region the beta has

been fully transformed before cooling and therefore reached temperatures within the beta transus (990°C).

The alpha needles were confirmed using EDX that showed the needles (seen as lighter regions in Figure 5.20) had a higher Al content and lower V content than the surrounding regions. In the final region, shown under the red line, the alpha needles have grown from approximately 5-20μm (as shown in the top regions) to 50-100μm. These larger alpha needles indicate a region in which the liquidus temperature was reached i.e. a melt pool was formed. Given the short period of time the torch was applied it can be suggested that there is a fairly high local oxygen content on the surface of the metal. It is possible that this was introduced during the melt as the furnace had not been run for a period of time before the experiment was carried out.

5.5.3 Temperature Model

There were two quantifiable sets of results from the thermocouple experiment on the plate: the temperature isotherm estimations from the microstructure and the temperature measurements from the thermocouples. These known temperatures can be used to create models of the heat transfer through the plate when the torch is applied. The movement of the torch during this experiment can be modelled by a moving torch, similar to a weld line, and a stationary plasma torch.

5.5.3.1 Moving Torch

As Equations already exist within the book by Grong ‘"Metallurgical Modelling Welding" for a moving torch [50], it is easiest to look at this section of the trial described in Section 5.2. Using this Equation, Matlab was used to calculate the temperature of each cell within a grid for a given power input, (calculated to be Resistance*Current*Efficiency,

150*600*0.35=31.5 kW), track width and material properties. A Gaussian distribution is assumed for the torch plume. This model runs in approximately 54 seconds and therefore can be used easily to estimate the track width of the plume necessary to get the depth of the beta isotherm from the surface, taken to be an average of the distances shown in Figure 5.19 (0.554 mm).

$$dT = \frac{q_0}{2\pi\lambda}\frac{1}{(R+100)}\exp\left(-\frac{\frac{v}{2}}{a}(R+xx)\right) \qquad \textbf{Equation 5.16}$$

Where,

$$R = \sqrt{xx+yy+zz} \qquad \textbf{Equation 5.17}$$

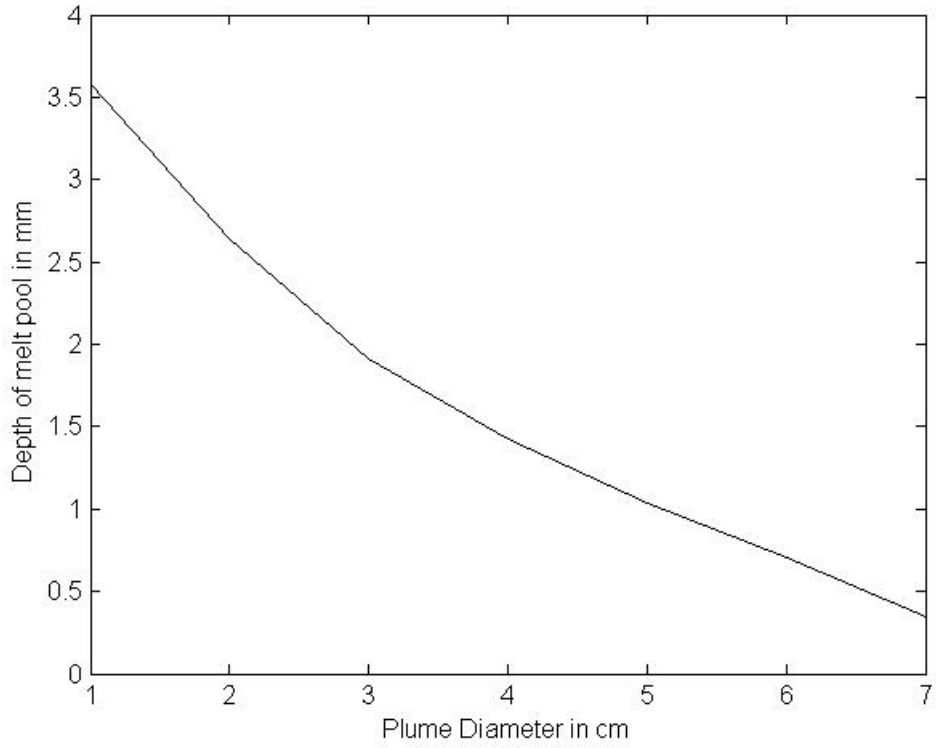

Figure 5.21: Graph showing the effect of the plume diameter on the melt pool depth

From the above graph it was found that for the required outcome, a plume diameter of 6.4 cm is needed. Using this, a similar process can be carried out to calculate the melt pool depth using the FEM software, Sysweld. Unlike the Grongs Equation, this software takes in account

the effect temperature has on the properties of titanium (for instance an increase in thermal conductivity with temperature). This FEM model takes approximately 4 hours to run, as a fine mesh size is needed through the depth of the plate in order to measure the shallow melt pools expected.

For this software, the power is inputted in terms of the energy per unit length (J/mm), EPUL, calculated from Equation 5.18. Whilst the torch is moving this was found to be 720 J/mm (based on a net power of 90,000 kW and a velocity of 125 mm/s, calculated from the video of the melt).

$$\boldsymbol{EPUL = P * \frac{1}{v}} \qquad \textbf{Equation 5.18}$$

Where P is the net power of the torch and v is the velocity, the units for which are shown below.

$$\boldsymbol{\frac{J}{mm} = \frac{J}{s} * \frac{s}{mm}} \qquad \textbf{Equation 5.19}$$

A fine mesh was used on the sides of the plate perpendicular to the weld direction, and an inverse Gaussian distribution of mesh size on these planes. This was in order to give a fine mesh distribution in the region parallel to the weld line direction, to increase accuracy while reducing the overall mesh size to decrease processing time.

0.07 seconds

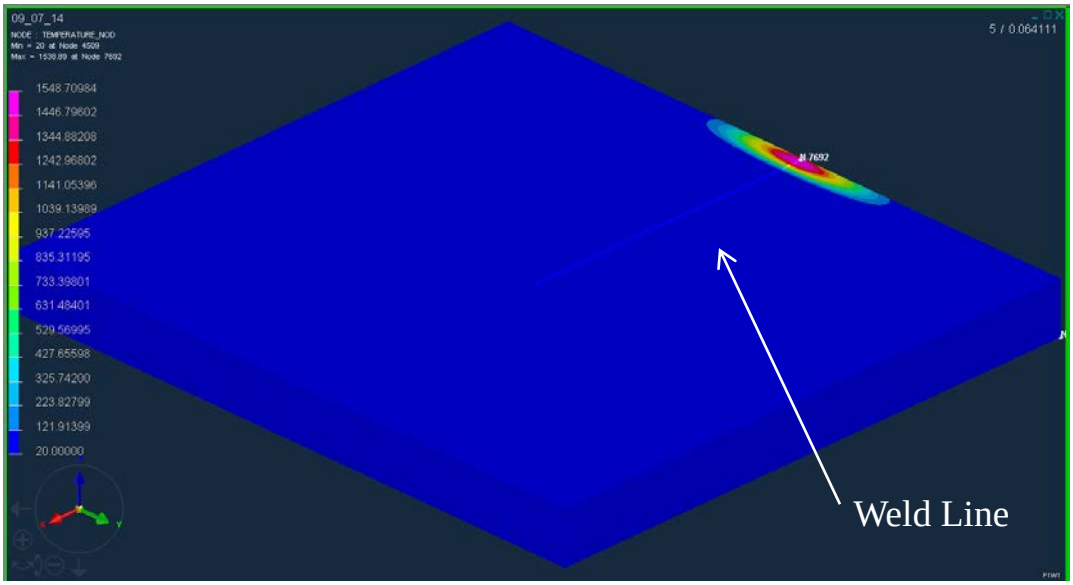

0.58 seconds

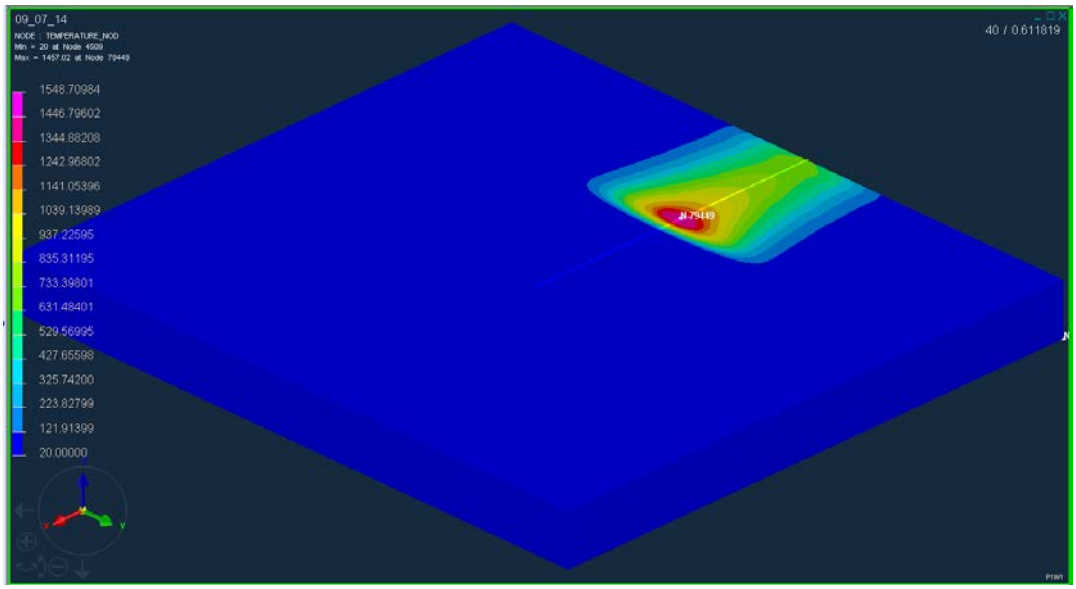

1.05 seconds

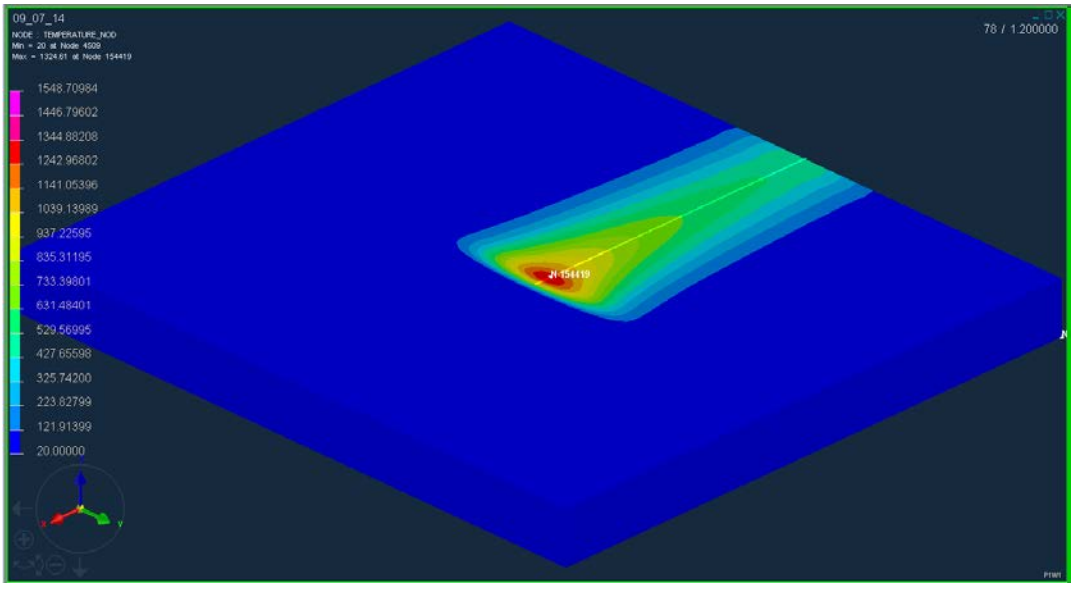

Figure 5.22: Showing the thermal isotherms formed as plasma torch moving from the edge to the centre of the plate. (13 cm at 12.5 cm/s)

A threshold was applied to the plate marking any areas above 990˚C as grey. A cross-section was then made in the approximate position the microstructure was taken, at the time step when the beta transus isotherm was at its deepest. The beta transus was found to be 0.47 mm, comparable to the beta transus depth measured from the microstructure, when the track width of the plume was 5.5 cm. A further check was then made by measuring the width of the beta transus on the surface of the plate, which was found to be approximately 40 cm for both the model and the actual plate. These dimensions are shown in Figure 5.22. The reason this is smaller than that calculated using the Grong Equation, is likely to be due to the temperature dependent properties allowed for in Sysweld, causing the conduction of heat to be greater leading to the energy being dissipated faster.

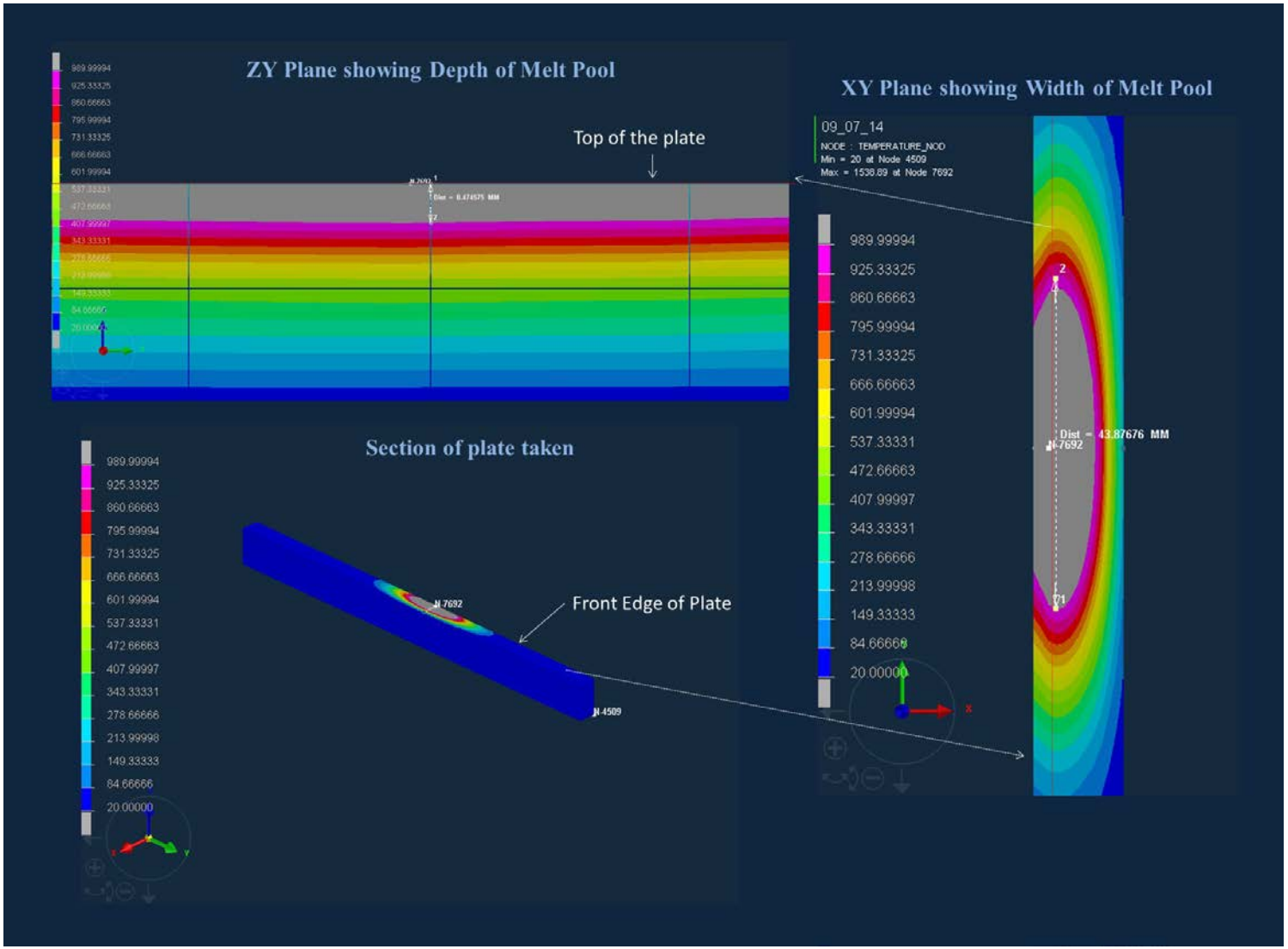

Figure 5.23: Images from Sysweld highlighting the regions from which measurements were taken

5.5.4 Limitations of Sensor Experiments

As the voltage wires measure the difference between two positions, 5 wire results in only 4 points, there are few data points. Therefore, in order for the current density to be calculated, the values between these points would need to be interpolated, decreasing the accuracy of the results. So it is necessary to carry out a second experiment, which has many more measurement points closer together.

The point of this experiment, ultimately, is to get temperature and voltage measurements that will indicate how the plasma torch effects feed stock as it is melted into a hearth. There are a few ways in which the plate experiment differs from an actual melt. These simplifications limit the ways the results can be compared to real life applications. As mentioned, the plate sits on top of the hearth and has two clear relatively continuous contact points. In reality, the solid skull containing the liquid metal forms, has a rough bottom surface forming multiple small contact points between it and the hearth. The skull is much thicker than the plate, (~60 mm) so in reality the heat and current must pass through more titanium before reaching the copper hearth. Also, due to the positioning of the plate it is possible heat is lost due to radiation, not just from the surface of the plate as in a normal melt, but to the area between the plate and the hearth as well.

In addition, by not melting, there is some possible difference in the current and heat transfer to and within the plate. For instance, the current and heat transfer from the plasma to the liquid metal might be different to that from the solid. Furthermore, the radiation from the hot plasma to a relatively cold plate, will definitely be different to that to a hot solid or liquid melt pool.

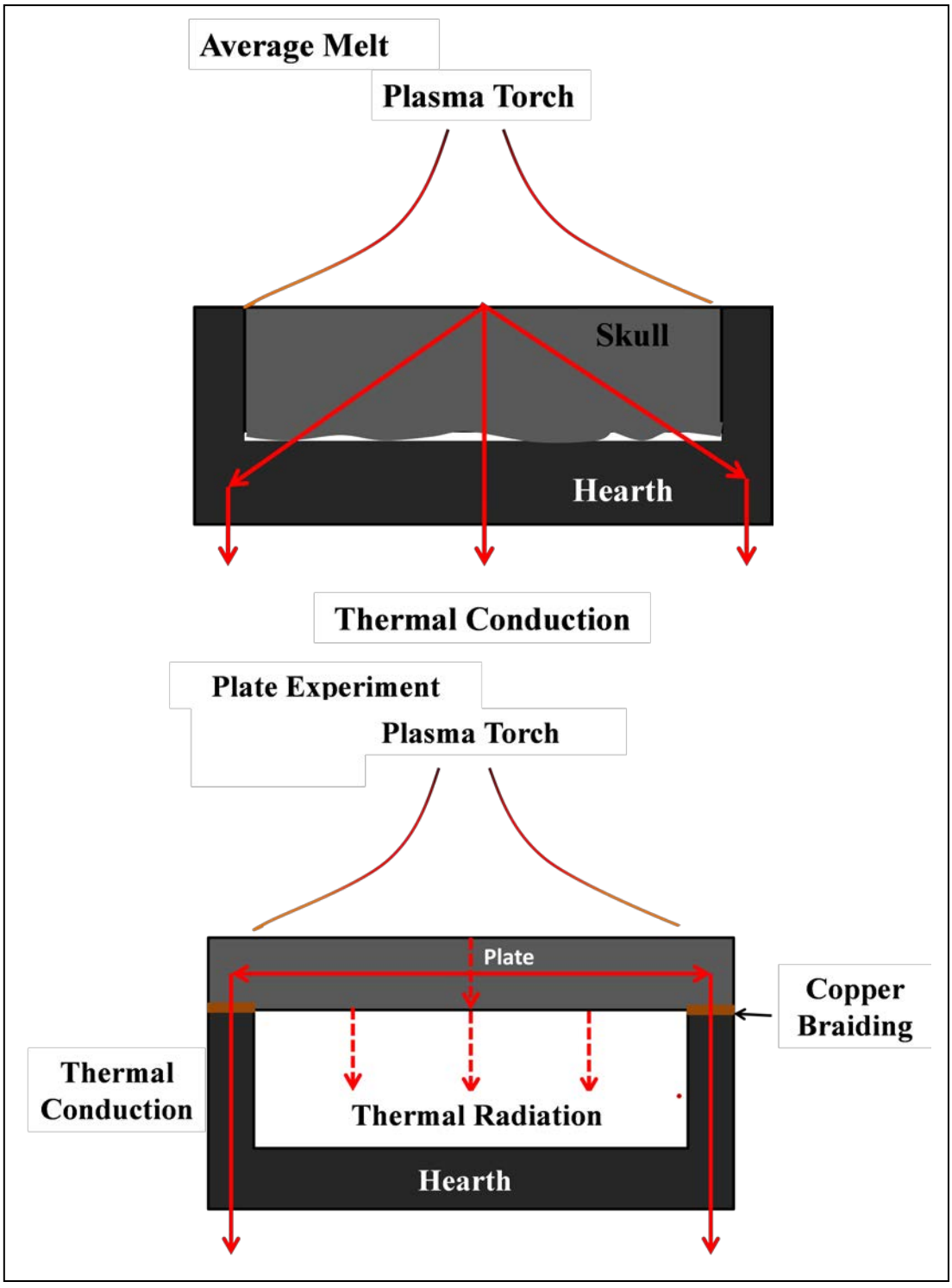

Figure 5.24: Showing the difference in conduction for the plate experiment and during an actual melt

An error that should be also noted relates to the use of the thermocouples. A fair amount of work has been done over the years looking at the response time and effect of orientation on the thermocouples. It has been discussed that heat flow in the most part, is vertical in the hearth. In order to measure the temperature changes in the plate, thermocouples

are orientated vertically, parallel to the heat flow direction. As the thermocouples were mounted 3mm into the plate, and have a different thermal conductivity to the titanium, there is an interruption to the heat flow as described by William D.Brewer in 1967[102]. He found that by orientating the thermocouple parallel to heat flow, some readings can be in the order of hundreds of kelvin below the actual temperature. This is due to heat being conducted away from the material.

The response time can be reduced by using small diameter thermocouples, although for this experiment, the size of the thermocouple was limited by the possible drill hole sizes. As mentioned, the thermocouple needs to sit tightly within a hole in the plate, therefore the drill hole needs to be ideally 0.1 mm bigger than the thermocouples diameter. For this reason 1 mm thermocouples, with 1.1 mm holes were used. However, due to the short period of time the torch was on it was felt necessary to measure the response time, which was found to be less than a second.

In addition to the thermocouples, steel bolts were required to hold the spring loading system in place. This is similar to the method used by R.M.Ward et al.[103], where they inserted thermocouples into an ingot in a plasma furnace crucible. As steel has a higher thermal conductivity than titanium, it is likely that the presence of these bolts causes some effect on the heat flow.

6) Radiation

6.1 Introduction

It has been mentioned that radiation is one way in which heat is transferred from a plasma torch. However, little research has been done to date looking at the amount of heat radiation produced from a plasma torch and the subsequent effect that has on melting. It is

often assumed that heat is only transferred from the torch by conduction or convection, considering radiation solely as a source of heat loss [41]. A deeper understanding of the radiation from the plasma torch, as well as increasing the accuracy of models, it is also an important way to increase torch efficiency [43, 55]. Loss via radiation has been suggested as a cause for the decrease in efficiency particularly at higher torch powers [55].

The radiation flux (i.e. the power density in W m^{-1}) for a plasma plume can be assumed to be the total radiation emitted from the plume divided by its area. By considering the flux received at a second area and knowing the geometry of both, it is then possible to calculate the flux leaving the first object.

6.2 Method

The purpose of the radiation trials is to assess the extent to which radiation plays a part as a heat transfer mechanism from the plume to its surroundings. Radiation is often thought purely as a heat output from the melt pool and skull, rather than an input. This part of the thesis hopes to look at the validity of this assumption in more detail, by calculating the amount of radiation that reaches the melt pool.

In this work, radiation was measured using a copper disk thermocouple that was pointed at the centre of the plasma plume (shown as the ‘target’ in Figure 6.1 below). The temperature rise felt by the thermocouple, is indicative of the heat flux from the plasma (see equations 6.1-6.3).

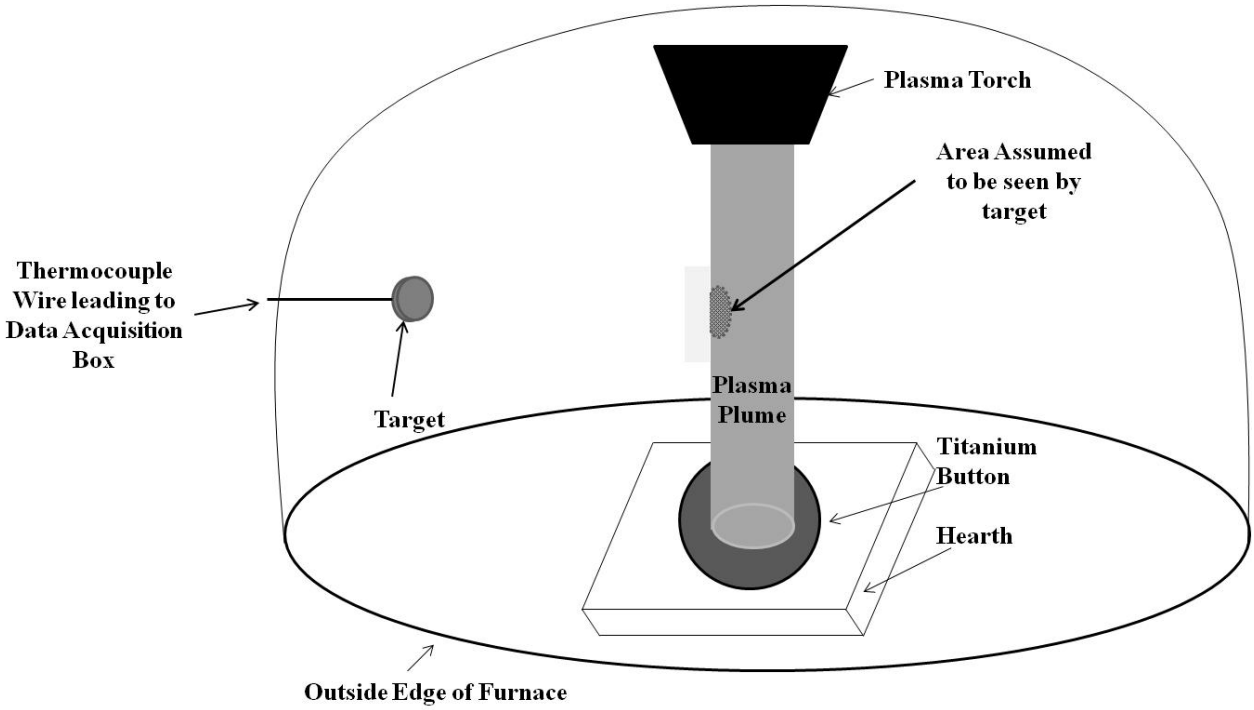

Figure 6.1: Schematic of the set-up of the thermocouple in the Plasma Button Melter.

6.2.1 Equations

All of the radiation calculations in this thesis are based around the following Equations:

$$\boldsymbol{Q = C_p m_t \frac{\Delta T}{\Delta t}} \qquad \textbf{Equation 6.1}$$

$$\boldsymbol{Q = F_{1-2} P_r A_t} \qquad \textbf{Equation 6.2}$$

$$\boldsymbol{P_r = (T_H{}^4 - T_C{}^4)\varepsilon\sigma} \qquad \textbf{Equation 6.3}$$

Equation 6.1 describes the rate of temperature rise on an object, $\Delta T/\Delta t$ (K/s), in relation to its heat capacity, C_p (J/kgK), and mass, m_t (kg). Most of these values relate to the properties of the disk thermocouple which is constant, the only one of which that varies during the experiment is the $\Delta T/\Delta t$ and is measured during the melt. Therefore it is necessary to measure the materials constants prior to the experiment as described below.

Equation 6.2 goes on to describe the heat energy on the thermocouple as a result of the radiation from the plasma plume, linking the thermocouple and the plume. For this equation A_t refers to the area of the thermocouple disk. A view factor, $F_{1\text{-}2}$, has also been included at this point, as not all radiation that leaves the plasma plume will be intercepted by the thermocouple.

Finally Equation 6.3 describes the radiation heat flux (in units of W/m^2) from the plasma plume. This equation is identical to Equation 2.2, however is included at this stage for completeness. In addition to Equations (6.1-6.3), the view factor will need to be calculated for each set-up.

6.2.2 View Factors

View factors, $F_{A\rightarrow B}$, are used extensively and describe the amount energy produced by object A that is intercepted by object B (commonly also referred to as shape factors).View factors take a value between 0 and 1 and can therefore be used to find the amount of the total radiation that hits object A from B. The value for the view factor is purely controlled by the dimension, shape and orientation of the two objects. (More details are given in Appendix D). The most common view factors available are based on parallel rectangular plates, parallel disks and perpendicular disks [104]. However, work has been published focusing on much more complex set-ups, for instance a disk parallel with an annulus [105]. Using trigonometry it is possible to look at two bodies that are off centre from each other (e.g. un-aligned plates), however this often complicates calculations.

6.2.3 Uses of view factors

There is a wide variety of purposes for which radiation view factors may be used. Research to date using view factors has included, but is not limited to, applications on multiple scales such as:

- Sky view factors are used fairly extensively to study the proportion of radiation that hits the ground with given topographies, canopies and their consequential effects. This is done most commonly using known view factors describing the relationship between hemispheres (the sky) and points inside the hemisphere (the ground) [106-109] or, by using video camera with a fish eye lens in order to count the proportion of pixels that contain sky from a given region [110].
- Radiative heat transfer in cellular metal foams with open cells uses complex repeating geometries to model the cells [111].
- Fire spread due to radiation from the flame front to model the time between 'ignition of the flames to steady-state spreading', [112] in order to access necessary response times. Where the flame front is modelled as a circle moving over time further from a point source [112].

These examples show the range in geometry and scale that can be studied using radiative view factors. Given the success of this technique over many years, it was felt worthwhile to apply it to the plasma torch in the PAM furnace to study the amount of the heating from the work piece caused by radiation. Without the use of expensive Spectrometer Equipment, the measurement of the radiation from a plasma plume relies on a disc thermocouple placed outside of the plasma plume and pointing towards it. This method can therefore be described by two objects, A and B, with a given view factor from A to B, $F_{A\rightarrow B}$, where $T_A >> T_B$.

6.2.4 Assumptions

For all the experiments and any models of the plume, there are some unknowns that have to be accounted for by the following assumptions:

- The plasma is a blackbody i.e. it absorbs 100% of radiation and is hence opaque. The benefit of this simplifying assumption is that the emissivity value can be assumed to be 1 to calculate the energy leaving plasma. It also means that radiation is assumed to only come from the plume surface nearest to the target and not travel through the plume.
- In general, the plasma plume is a cylinder of length, L_a and radius, r_p. From which the surface area can be calculated.

Further assumptions will also be made later regarding the geometries of the thermocouple and plasma for given situations.

6.2.5 Preliminary Experiment

Preliminary experiments were carried out in order to determine the constants for each thermocouple being used for this experiment. By combining Equations 6.1, 6.2 and 6.3, it is possible to describe the rate of temperature rise as follows:

$$\frac{dT}{dt} = \frac{\varepsilon_T A_T}{m_T C_p}\, \sigma \varepsilon_F T_F{}^4 F_{F \to T} \qquad \textbf{Equation 6.4}$$

The variables, $\frac{\varepsilon_T A}{m_T C_p}$, are all dependent on the properties (dimensional and material) of the thermocouple being used and can therefore be assumed to be a constant C, for a given thermocouple, simplifying Equation 6.4 to Equation 6.5 below.

$$\frac{dT}{dt} = C\,\sigma\varepsilon_F T_F{}^4 F_{F\to T} \qquad \textbf{Equation 6.5}$$

By using a furnace of a known temperature, T_F and $F_{F\to T}$ can be treated as independent variables and the rate of change of temperature can be measured using a disk thermocouple connected to a data acquisition device. Once a value for C is acquired, it can be used for calculations when T_F is not known (i.e. in the calculation of the radiation from the plasma plume).

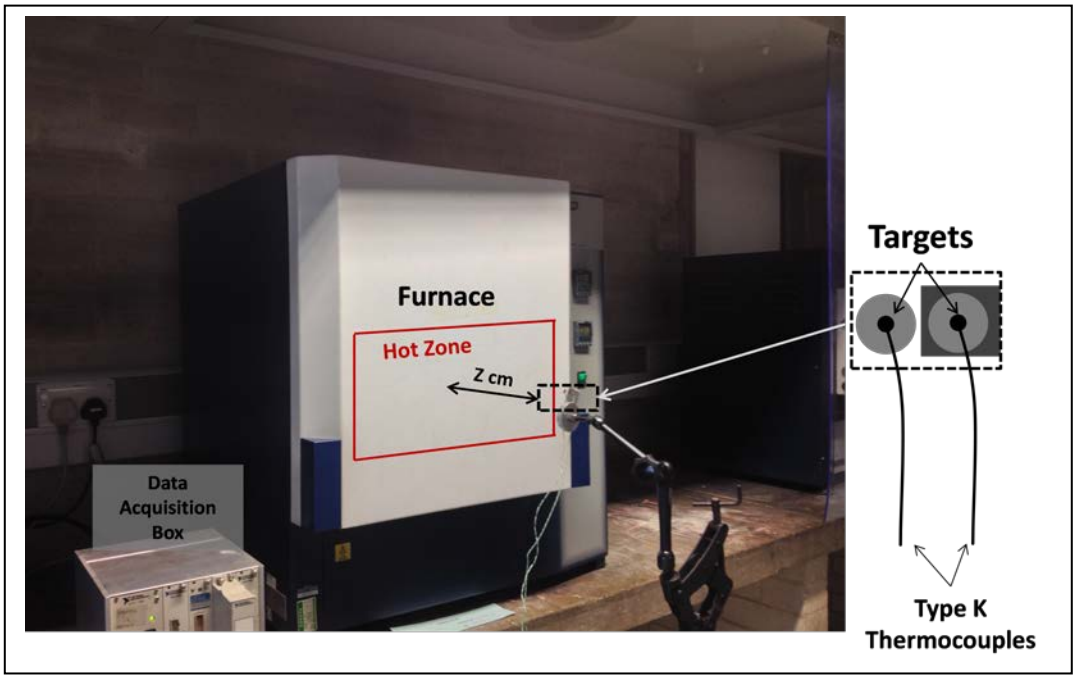

Figure 6.2: Set-up of target in front of the furnace

The set-up for these experiments is shown in Figure 6.2. The target is placed in front of the furnace approximately in line with the centre of the hot zone, and once at the desired temperature has been reached, the furnace door is opened. Whilst the door is being opened, the view factor of the target is slowly increased until the door is fully opened. Therefore, assuming it takes one second to open the furnace door, the first second of temperature measurements should be discounted. Secondly, due to the large temperature difference

between the furnace and the room, heat is transferred quickly via conduction, convection and radiation, causing the temperature of the furnace to decrease. Therefore, the readings of interest are those taken for the first few seconds after the furnace door has been fully opened. It is assumed that the temperature stated by the oven sensor is accurate, as the difference in the temperatures being looked examined here are fairly significant. The summarised results from this experiment are shown in Appendix C.

The graph below shows how the temperature of one of the thermocouples (labelled 'Thermocouple 1' in Table C-1, Appendix C) changed with time. This graph suggests that there is a positive relationship between the rate of temperature rise in the thermocouple, when it is either closer to the oven or the oven temperature is increased.

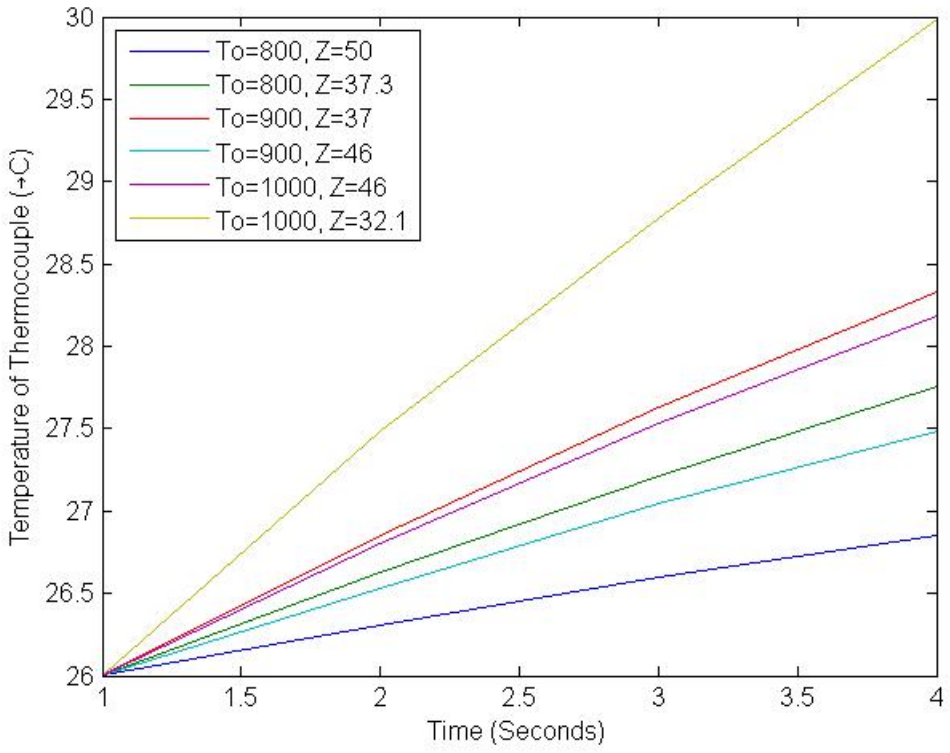

Figure 6.3: Change in temperature with time for a thermocouple where the distance between thermocouple and oven, and temperature of the oven, are varied.

(To is the temperature of the oven (°C) and Z distance between the oven and the thermocouple (m))

The results for all the thermocouple are further summarised in Figure 6.4 below.

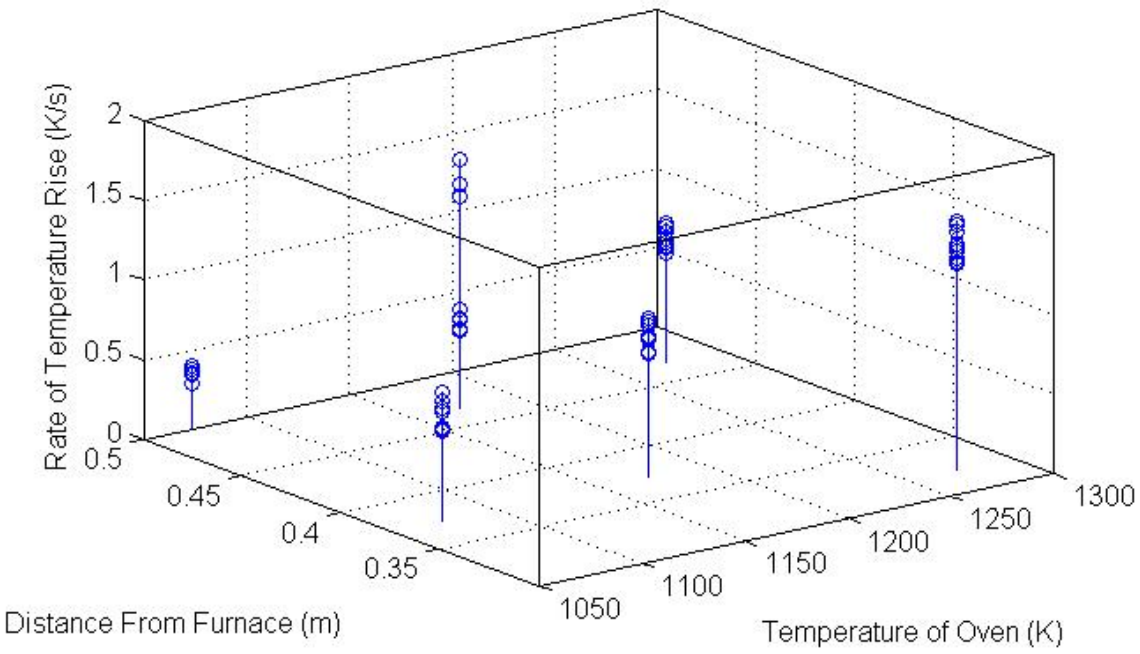

Figure 6.4: Showing the relationship between the temperatures of the oven, distance between the oven and thermocouples and the subsequent temperature rise of the thermocouple

In general, it was found that the rate of temperature rise increased positively with the temperature of the oven and increased negatively with the distance between the oven and the thermocouple, as shown in Figure 6.4. This is caused by an increase in the radiation power from the oven as the temperature of the oven increases and a decrease in the view factor with distance respectively (see Figure 6.5). Three points do not follow this trend (highlighted in red) these points refer to three thermocouples exposed to the oven simultaneously to one another. It is thought that during this particular repeat a nearby oven may have been opened, causing the temperature to rise.

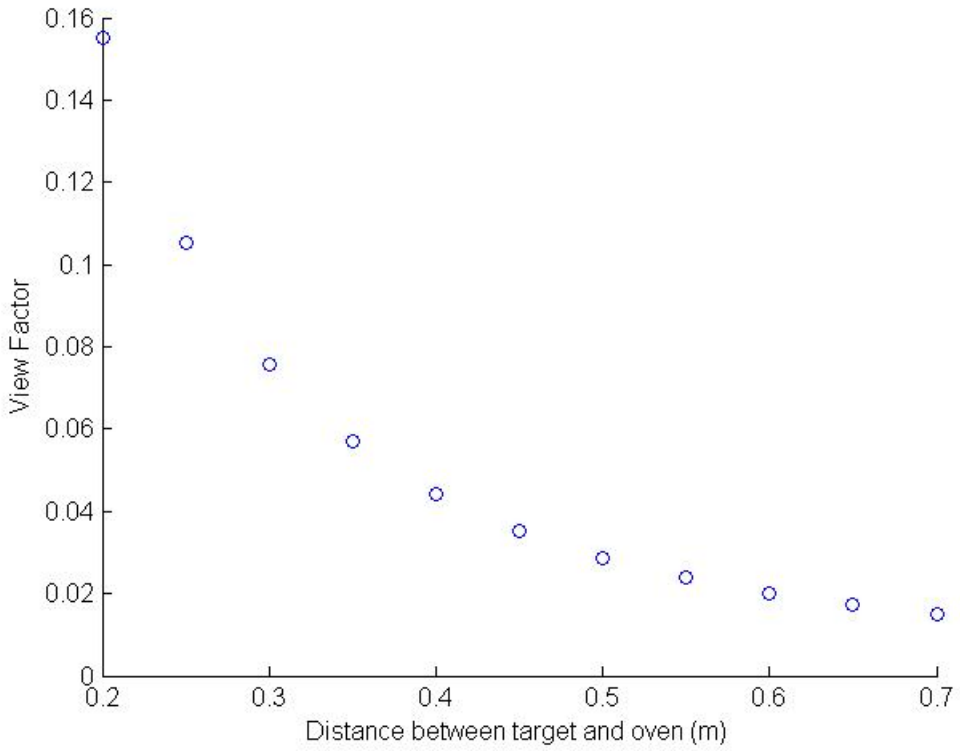

Figure 6.5: View Factor vs. Distance from furnace.

NB: The view factors are low (on average 8% of the total view factor) as the target is realtively small in comparison to the room.

This experiment works on the basis that the target is heated solely by radiation (i.e. does not come into contact with any hot gas from the furnace). To test whether this was achieved, a control target was set up that had a metal 'shield' placed in front of it to block any radiation (shown in Figure 6.1 as a dark grey square). It was found that the control target had an average temperature rise over the whole trial of 0.025 K/s, significantly lower than the temperature rise for non-covered thermocouples of 0.82 K/s (Table C-1, Appendix C and Table 6.1(below)).

Table 6.1: Calculation of constants for different oven Temperatures

Temperature (˚C)	**800**	**900**	**1000**	**All**
Average dT/dt	0.51	0.86	1.10	0.82
Average $(\varepsilon_T A)/(m_T C_p)$	1.86E+03	1.96E+03	2.52E+03	2.19E+03
Standard Deviation	268.7453361	525.4803383	232.7491363	372.0318708

Interestingly, as shown in Table 6.1, the thermocouple constants change with temperature. This is likely to be caused by a change in the temperature dependent variables (i.e. an increase in the value of ε). In addition to this, each thermocouple (three were tested in all in addition to the 'control' thermocouple) had separate constants calculated for them to account for differences in each thermocouple.

6.2.6 Plasma Furnace Radiation Experiment

Using the constants found from the furnace, it is possible to apply the same principle to the plasma furnace, where the temperature and radiation power is unknown. The plasma furnace differs in one particular way to the preliminary experiment, as the plasma furnace cannot be opened whilst it is on. Although the temperature of the furnace remains high after the torch has been turned off, radiation is no longer being emitted. Therefore the thermocouple had to be placed inside the furnace, making setting up a bit more complex.

In addition, the size of the furnace (approximately 1m in diameter) is much smaller than the room in which the preliminary experiment was carried out. As a result, the hot gas quickly fills the area surrounding the target, affecting the temperature measured by the thermocouple and not allowing the effect of radiation to be accurately measured. To minimize the effect of the hot gas heating effect, the thin circular metal disc was placed in a tube of ceramic material, as shown in Figure 6.6 and Figure 6.7. By doing this it may be assumed that the majority of changes in heat experienced by the metal 'target' are as a consequence of heat transfer from the torch via radiation (i.e. Q can approximately be equated to the radiation flux on the target).

Unlike the sensors trial, the plasma torch is initially struck close to the button and then raised to its full height (16 cm). The tube is pointed at the centre of the plume when it is at its full height. The experiment is also repeated at the same height when the tube is covered and when it is at 90° to the plume. For this set-up it was assumed that no radiation from the arc makes contact with the thermocouple and any heat rise is due only to contact with the atmosphere.

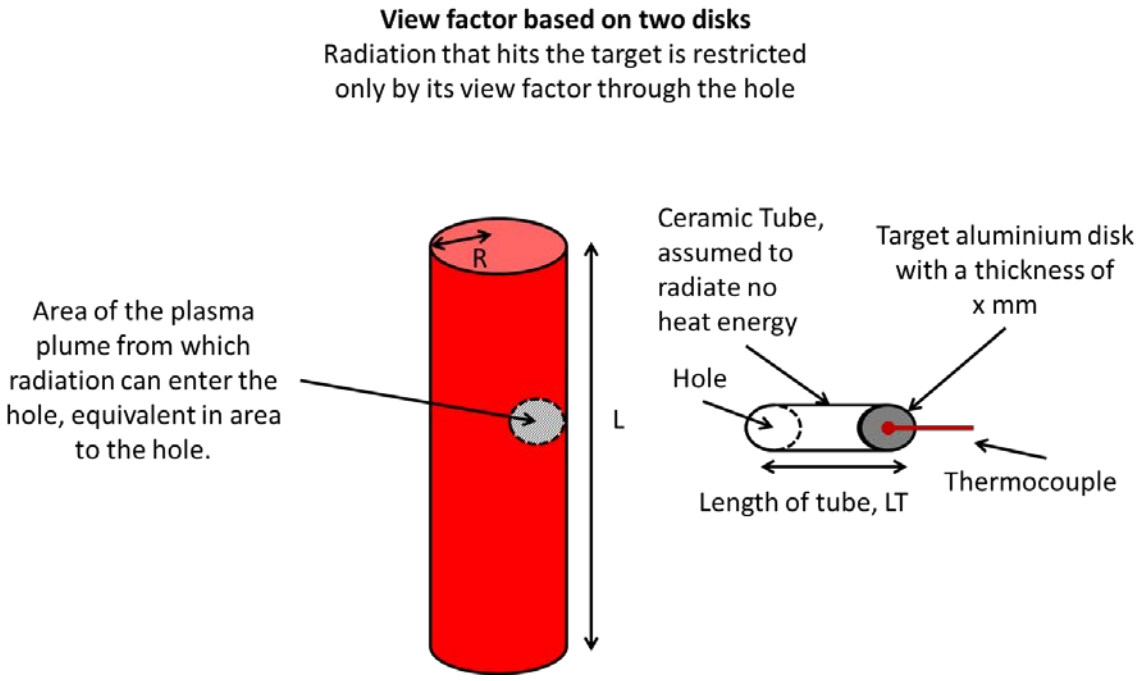

Figure 6.6: View of the plasma plume from a target in a ceramic tube

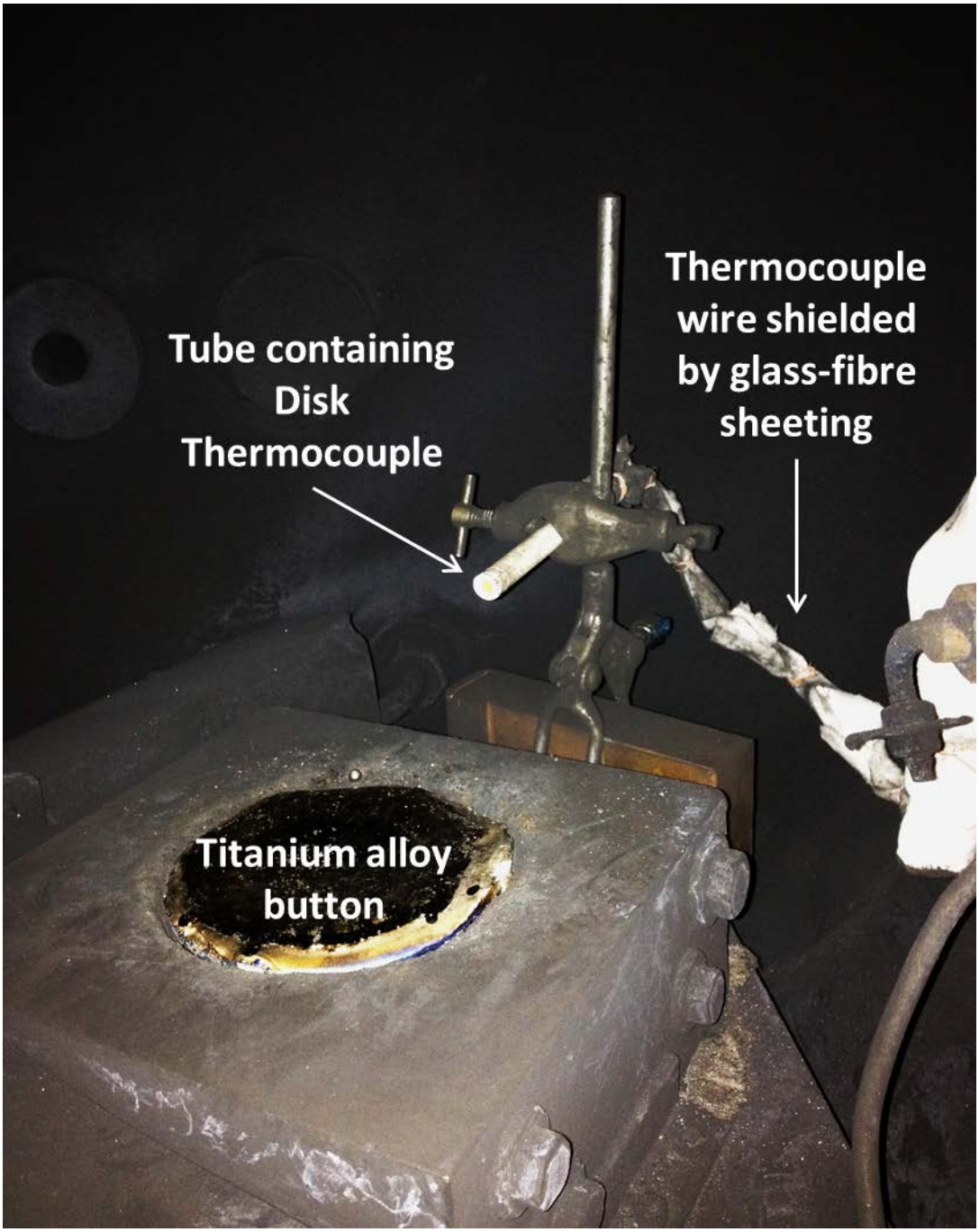

Figure 6.7: Set-up of the tube in the furnace when it is pointing towards the plume

6.2.7 Numerical Model of view factor in a tube

Before any further experiments were carried out, a numerical model was needed to assess the effect of the length of the tube on the rate of temperature change and ensure it was measurable.

It was assumed that the arc power was 100 KW (this is based on the calculated torch power for the furnace used as described in a previous section) and that the fraction of this that can be accounted for by radiation is 10%. This is a fair assumption as previous research showed a relationship between radiation power, P_R and input power, P, to be $P_R=1.629x10^{-3}P^{1.55}$[43], at the P suggested this would give a P_R of $9.16x10^4$ (approximately 10% of P).

By assuming the plume is cylindrical, as done previously, the radiation power density (W/m^2), P_{rd}, can also be calculated. In this case, the view factor of interest is between the target and the hole at the front of the tube. From Figure 6.8 it can be suggested that a distance of 0.1 m would lead to the temperature rise being sufficient (over 0.05 K/s).

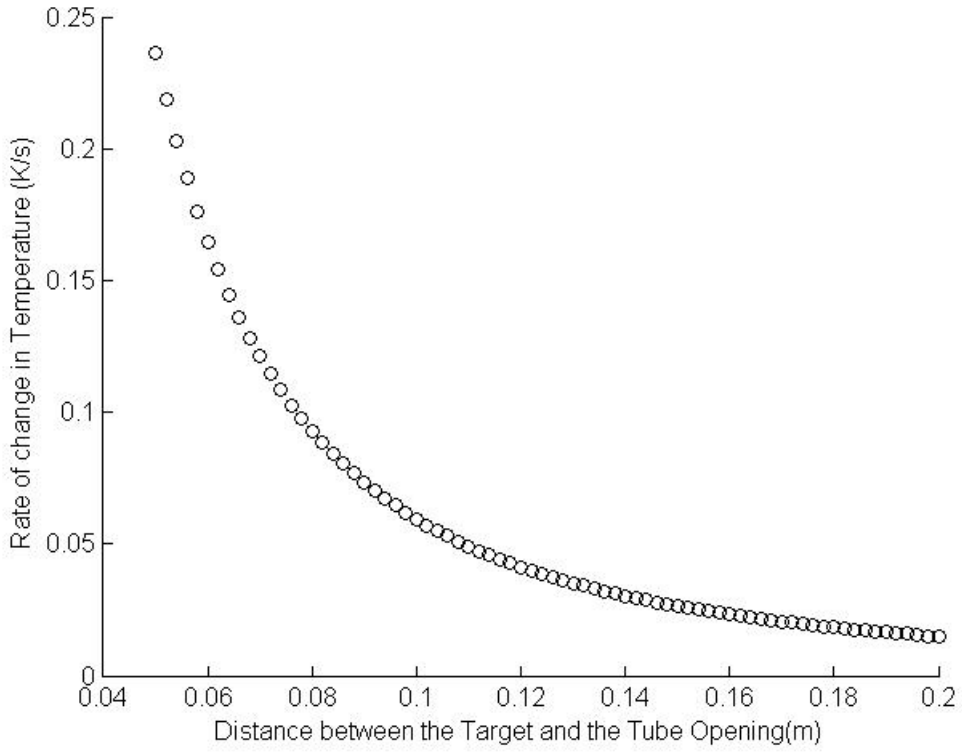

Figure 6.8: Change in temperature increase with distance between the target and the end of the tube

However, if the target is placed too near the front of the tube it may come into contact with the hot gases from the plasma, leading to heat transfer to the target via conduction and convection.

The next step was to calculate how much of the plume the target sees. The equations only estimate the average heat flux and it is necessary to understand what percentage of this is made up of the high temperature plume and how much is the cooler furnace. If it sees a lot of the furnace, the measurements will underestimate the actual radiation power of the plume.

To do this, the effect of the position of a point on a target in a tube on the distance it views outside of the tube was examined. The ratio of plume to furnace that will be seen by the target was then calculated to find the distance down the tube at which the target only sees plume. Only 2D was considered at this stage to give an idea of what is occurring, while reducing computational time. The full derivation of Equations 6.6 and 6.7 can be seen in Appendix E.

$$\boldsymbol{DA = y\left(D2 * \frac{Dt}{D1}\right) + x\left(D2 * \frac{Dt}{D1}\right) + Dt} \qquad \textbf{Equation 6.6}$$

As y + x =1 Equation 6.6 can be generalised as shown below,

$$\boldsymbol{DA = D2 * \frac{Dt}{D1} + Dt} \qquad \textbf{Equation 6.7}$$

6.2.7.1. Checking the Equations

Figure 6.9 shows a scale image of the tube facing the plasma plume. The top view shows a scaled version of Figure 6.6, from which DA/2 (the distance between the centre line and the view line from the target centre) is measured as 0.69 cm. This is comparable to DA/2 calculated from Equation 6.7 using the same dimensions, found to

be 0.63 cm. For this example the plume is assumed to have a radius of 0.005 m, so the target is shown to see beyond the sides of the plume (i.e. it sees some of the furnace).

L=8.2 cm
Dt=0.625 cm
D2=12.4 cm

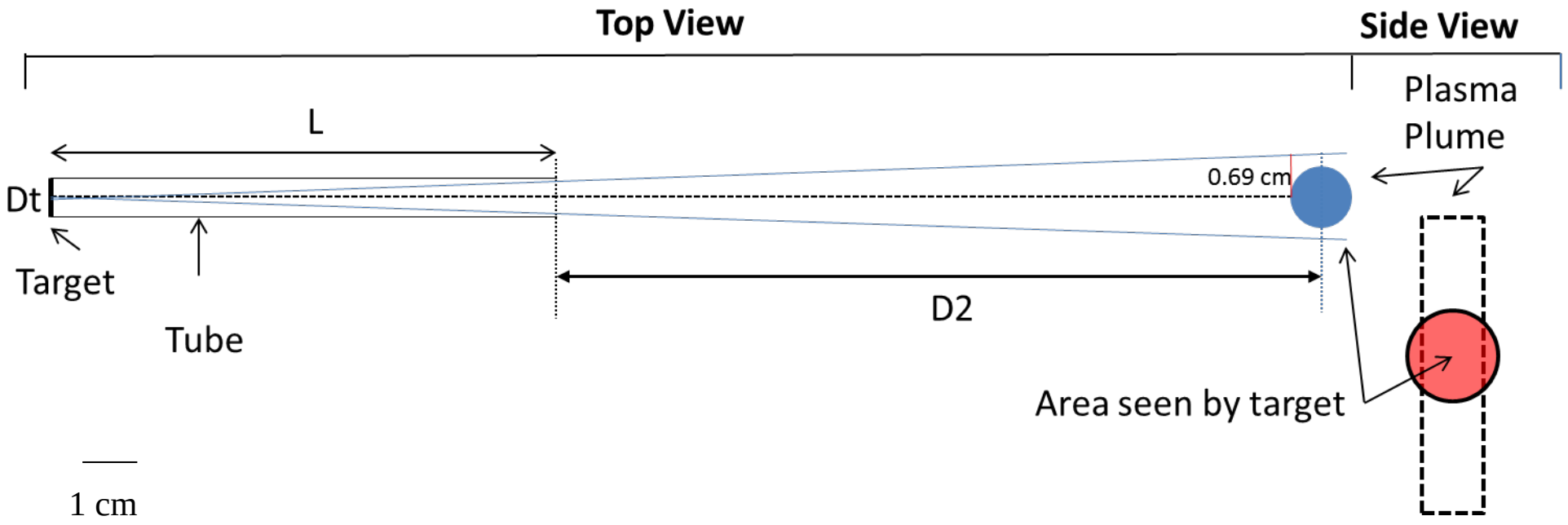

Figure 6.9: Image of the tube facing the plasma plume drawn to scale

6.2.7.2 Using the Equations

It was assumed that Dt is a constant, dependent on the diameter of the target (6.25 mm) and D2 is restricted. This is as it was found that if the tube was placed too close to the plasma plume (less than 10 cm away) it fractured, due to the high temperatures. Therefore D1 is the only independent variable and DA is the dependent variable in these calculations.

These Equations can be used to look at two aspects:

1. **How much of the plasma plume is seen by the target?**

   The ratio of plume to furnace was calculated, using the assumption that the target sees the plume as a rectangle with a width equivalent to the diameter of the plume and a height DA.

2. **How accurate is the parallel disk view factor?**

   When the target is in the tube it is assumed that the target does not receive or lose any radiative energy to the tube. Therefore, in theory the radiative energy it is receiving can be expressed as a fraction of the amount of radiation entering the hole, which can be calculated using the view factor between two parallel disks. However, this assumption decreases in accuracy with proximity of the target to the hole.

6.2.7.2.1 How much of the plasma plume is seen by the target?

The area of that seen that includes the plume, $A_{Covered}$, was calculated using the approximated equation:

$$A_{Covered} = r_p^2 + (d_p * r_p)$$ **Equation 6.8**

The approximation is applied below on three situations. In each case the area is slightly overestimated or underestimated by this equation, however overall it makes a good enough approximation to be useful. To verify this, the percentage area covered by the plume $(A_{Covered}/A_{Seen})*100$, where A_{Seen} is DA^2 was calculated by drawing a scale image and measuring the number of pixels for each area, using an image processing software and the equations above. For both calculations the dimensions from Figure 6.7 were used. The Percentage area covered by the plume was found to be 77% and 78% respectively, giving an error approximately of 1%. Although this assumes that all of the plume within that area contributes equally to the radiation felt by the target. This assumption is discussed in the next section.

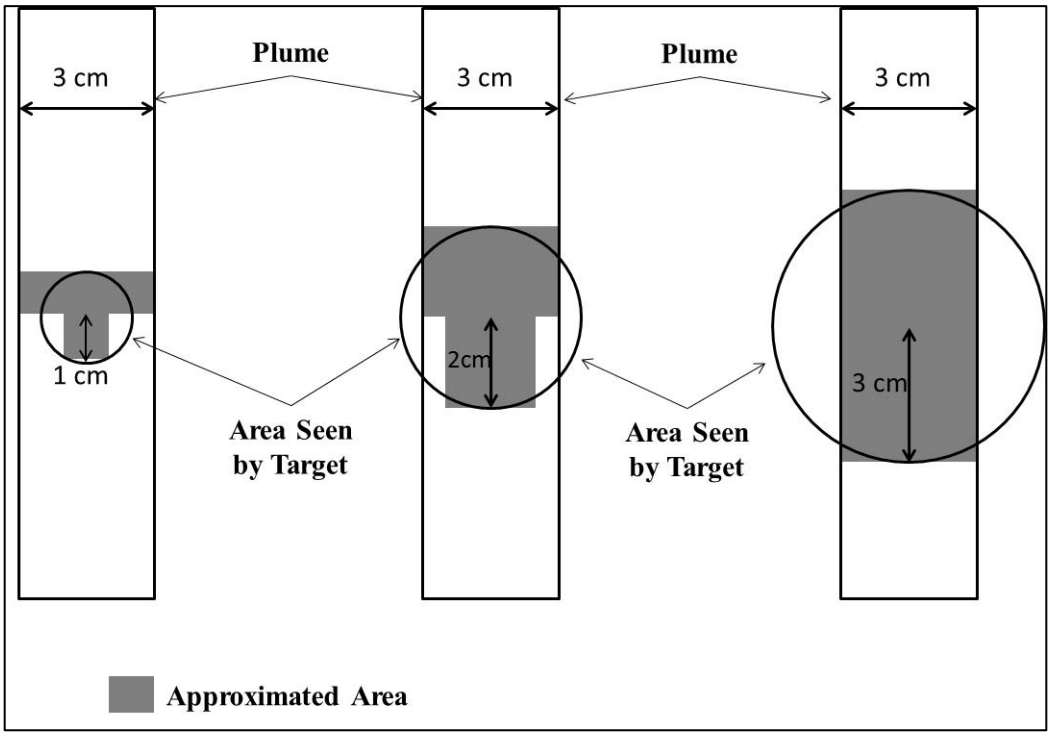

Figure 6.10: A to-scale diagram comparing the approximated area verses the actual area of the area seen that contains plume

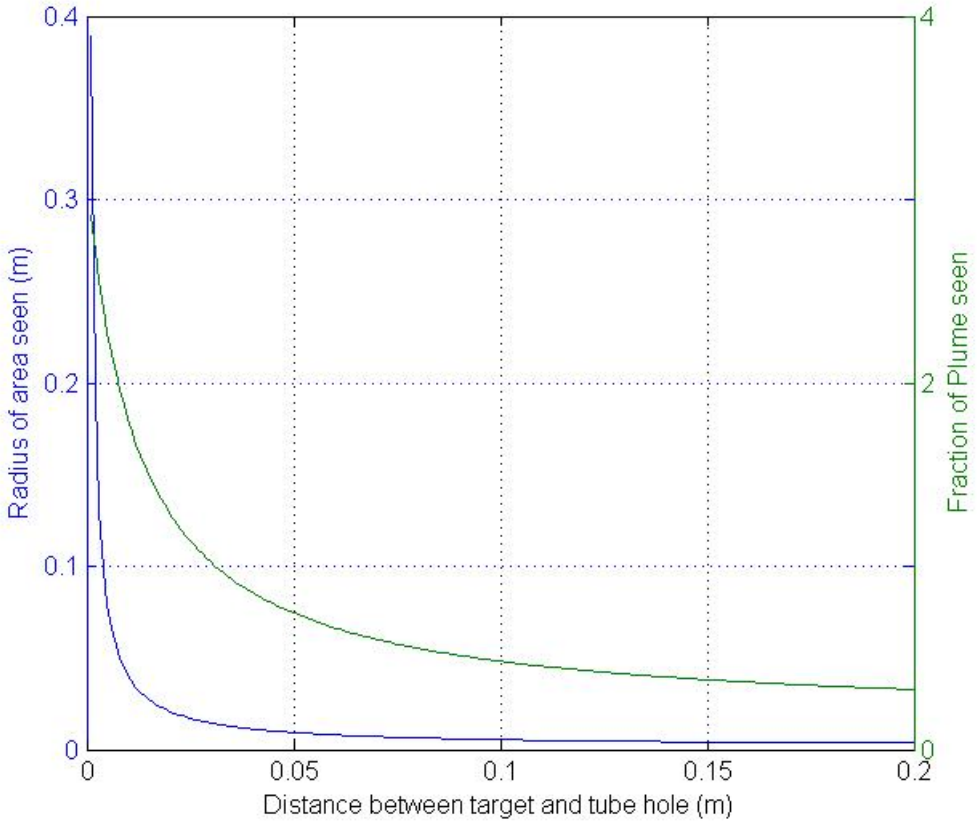

Figure 6.11: Change in the radius of the area seen by the target at different positions in the tube and the amount of the plume it views

Figure 6.11 assumes the plume has a diameter of 0.03 m, d_p, (based on the plume being 1 cm at the top and 5 cm at the bottom – taken from the radius calculation in section 5.5 Discussion: Temperature in Plate) and $A_{Covered.}$ This graph illustrates how, when the target is far down the tube it does not see the entirety of the plume. However when it is close to the front of the tube, the amount of the plume it sees is approximately ¼ of the total area seen. This shows that for the entire plume to be seen it must be less than 0.03 m from the front of the tube.

6.2.7.2.2 How accurate is the parallel disk view factor?

Figure 6.12 shows how as the thermocouple reaches the front of the tube it sees beyond the edges of the hole to a greater extent. Consequently the assumption that the view factor can be calculated using two parallel disks becomes less accurate and consequently would give an underestimate of the actual View factor between the tube and plume.

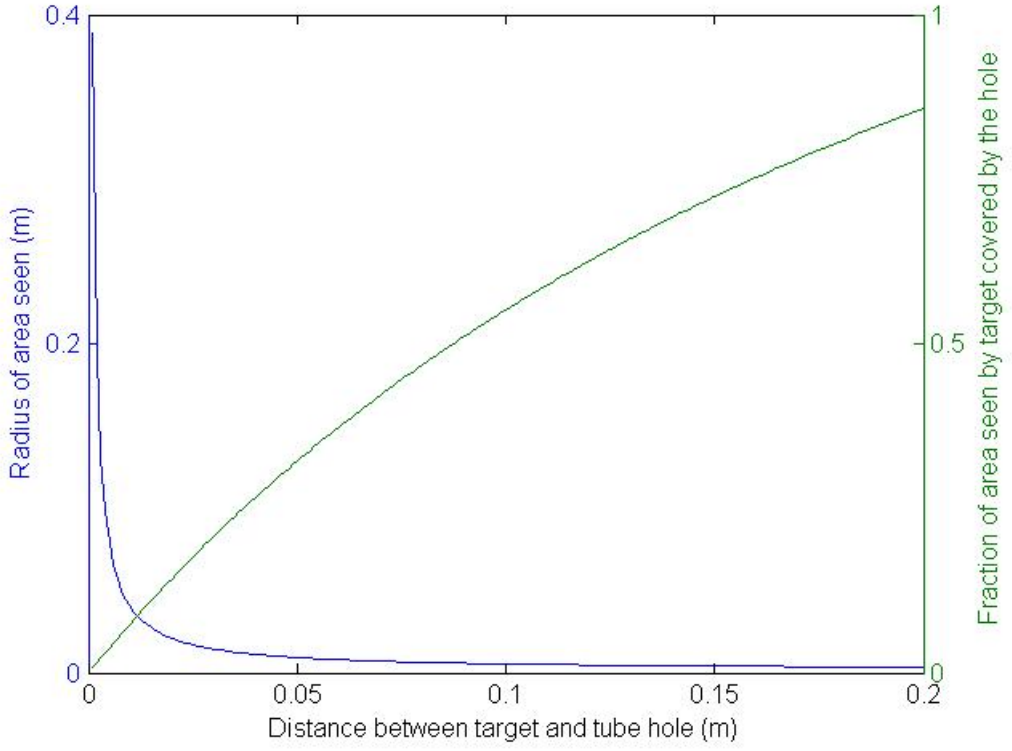

Figure 6.12: Two axis graph showing the effect of the distance of the target in the tube on how much of the tube hole it sees

Even if the target sees only plume there is still an additional error in using the parallel disk model. The centre of the area seen by the target contributes radiation to 100% of the target. However once pass the central area (a circle with a diameter of Dt) the amount of radiation contributed drops until it reaches 2DA-Dt (see Appendix E). This can be seen in graphical from in Figure 6.13 below. The graph suggests that the

closer in value Dt is to DA, the less of an error the assumption is that a circle of radius DA acts like a parallel disk to the target.

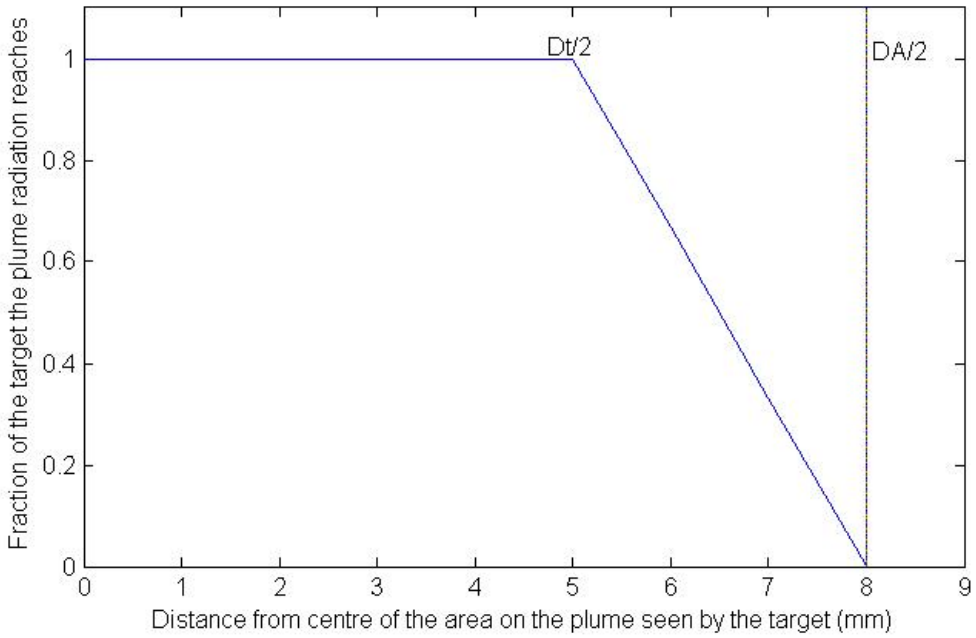

Figure 6.13: The fraction of target seen by the plume in relation to distance from the centre of the area seen

A better way of calculating view factor in this situation may be to use a 3-D model of the situation that takes into account the view factor between the target and the plume with the tube acting as a block to some of the radiation. Unfortunately, due to time constraints this could not be done here however should be included in the future work of this project.

6.3 Results

Initial observations of the data show a difference between the temperature rise for the thermocouple in Position A than Position B. The suggestion is that is that by pointing the tube towards the centre of the plasma plume, Position A (see Figure 6.15), the thermocouple receives radiation from it. When pointing away (i.e. being at right

angles to the plume-Position B) radiation should be blocked by the ceramic tube leading to the lower temperature rise seen in Figure 6.14.

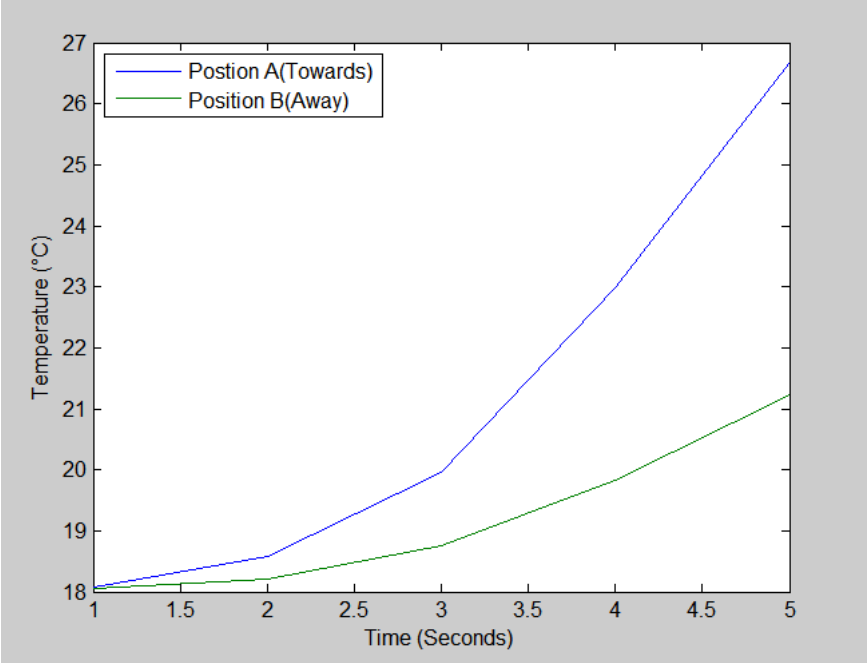

Figure 6.14: Plot of the change in Temperature with Time for a Thermocouple whilst the torch was on

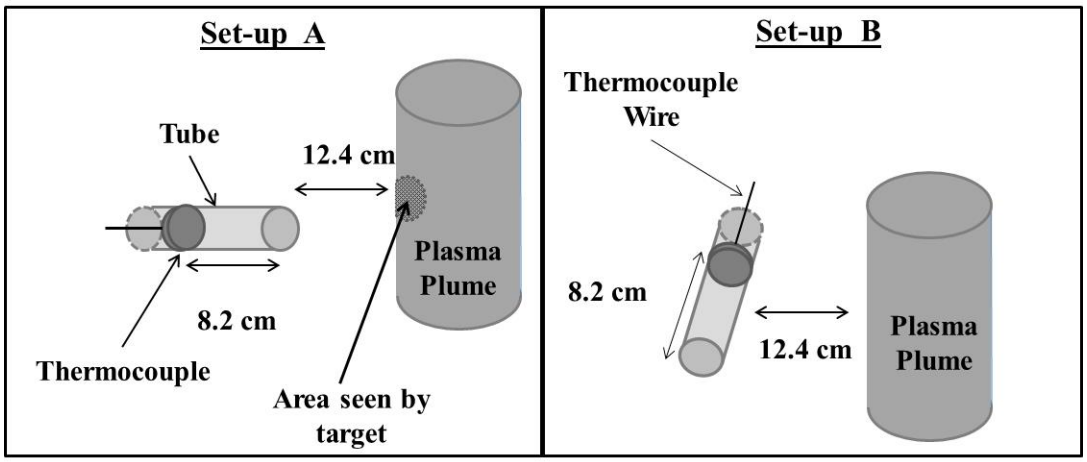

Figure 6.15: Different orientations of the target relative to the tube and the plasma plume

The raw data from the radiation experiments were recorded at a rate of 1000 per second. As there were variations in how long the data acquisition software was recording before the plasma plume was successfully struck, the start times and temperatures for each trial

had to be aligned with one another and an arbitrary end time was assigned. The results from which can be seen below in Figure 6.16 and Figure 6.17, showing the temperature rise of the thermocouple both when it is pointing towards and perpendicular to the plume.

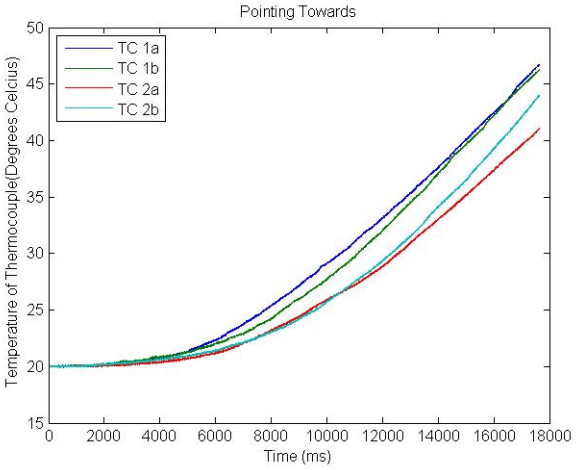

Figure 6.176: Raw data showing the temperature of the disk thermocouple with the tube pointing towards the plasma plume

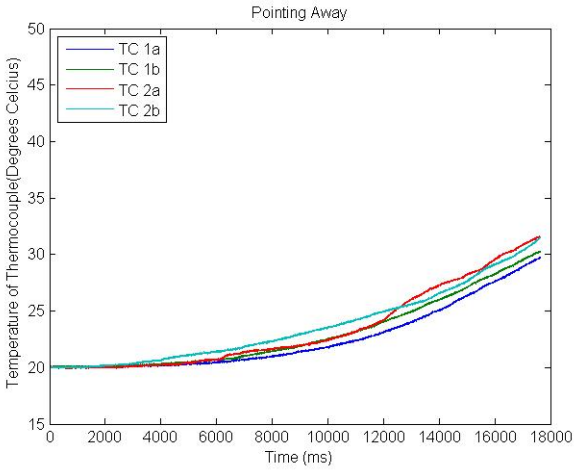

Figure 6.167: Raw data showing the temperature of the disk thermocouple with the tube perpendicular to the Plasma Plume

From this the rate of change of temperature can be caluclated and the data can be decimated to reduce the number of data points, as shown in Figures 6.18 and 6.19.

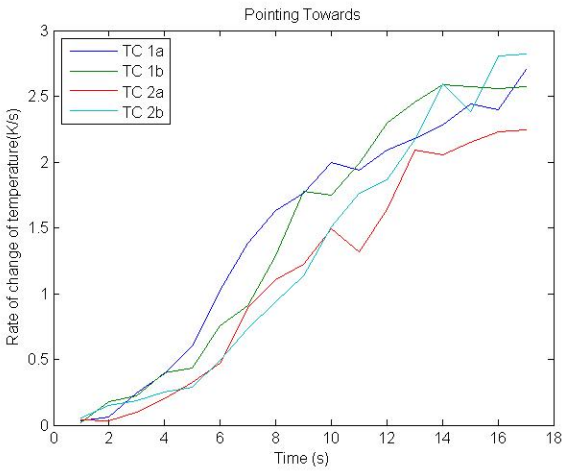

Figure 6.18: Rate of Change of Temperature Pointing Towards

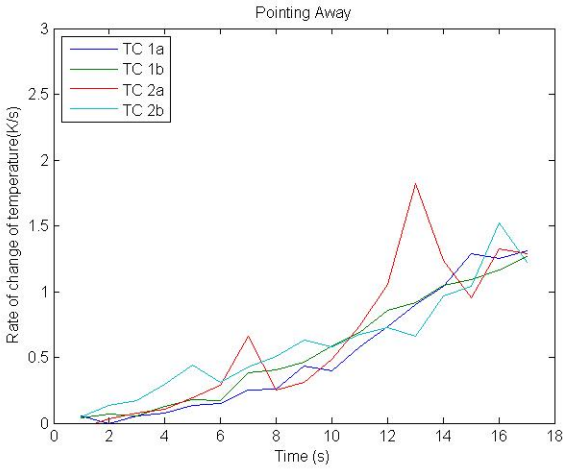

Figure 6.19: Rate of Change of Temperature Pointing Away

It is assumed that when the disk thermocouple is facing the plasma plume it is exposed to radiation from the plasma plume. Originally, it was assumed that the tube kept the hot gas from direct contact to the thermocouple and therefore the effect of convection (or conduction) from the gas can be ignored. However, as seen from the results when the thermocouple in not exposed to radiation from the plume, there is still a notable temperature rise caused by convection. This suggests that even with the presence of the tube, the thermocouples temperature rise is caused by the convective heat transfer and the radiative heat transfer from the plume.

i.e.

$dT/dt_{(Radiation)} = dT/dt_{(Convection\ and\ Radiation,\ Pointing\ Towards)} - Average\ dT/dt_{(Convection,\ Pointing\ away)}$

Where dT/dt is the rate of temperature rise in K/s.

As a result it is possible to separate the effects of radiation and convection, as shown in Figures 6.20 and 6.21.

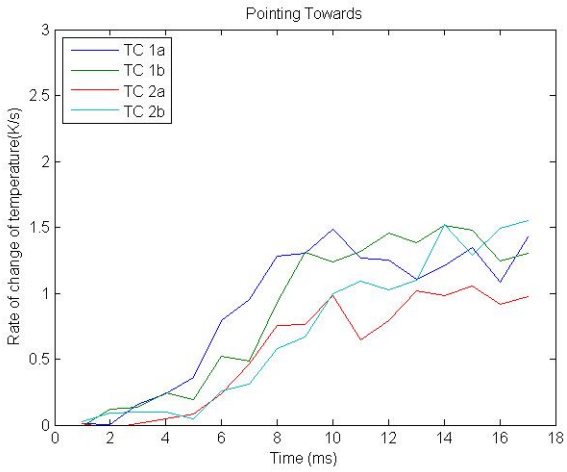

Figure 6.20: Rate of temperature rise caused by Radiation from the Plasma Plume

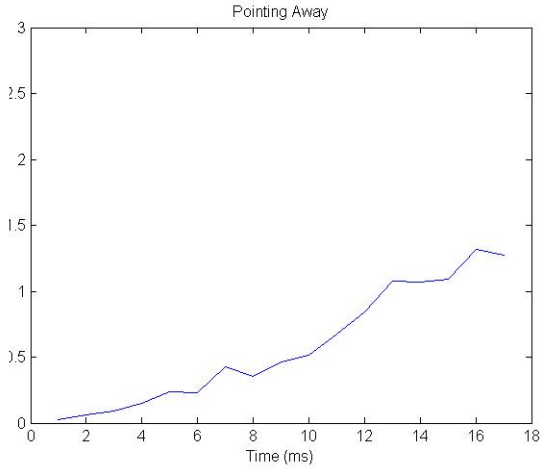

Figure 6.21: Average Rate of temperature rise caused by convection from the plasma gas

Finally, an average value for the rate of the temperature rise due to radiation is needed. As described in the method section, the plasma torch is initially struck close to

the button and then raised to the required height. This can be seen in Figure 6.20, where dT/dt steadily increases as the thermocouple is exposed to more of the plume. Therefore, the average temperature rise is taken from the last five seconds of the trial, as shown in Table 6.2.

Table 6.2: Results for two thermocouples showing the average rate of temperature rise for each repeat

	Thermocouple 1		Thermocouple 2		
Repeat	**A**	**B**	**A**	**B**	**Average**
dT/dt (K/s)	1.24	1.40	0.96	1.33	1.23

6.4 Discussion

From the dT/dt, Pr can be calculated by combining equations 6.1-6.3. From this the temperature of the plasma plumes can be calculated. Although these temperature measurements are not as useful for this work as Pr, (due to the many unknowns in their calculations) they give a good indication to whether the Pr values are realistic.

6.4.1 Temperature Calculations

For temperature calculations the emissivity is a commonly identified error for any calculation of temperature estimation using radiation. Therefore any temperature discussed in this work is the apparent and not 'true' temperature of the plume. For this experiment the emissivity of the plume was assumed to be 1 (i.e. a black body). As radiation is proportional to temperature to the fourth power, errors in this assumption can be directly related to errors in the final output. The differences in the final Plume Temperature estimations dependent on the emissivities are shown in Table 6.3.

Table 6.3: Results showing the average Radiation Power and Plume Temperature for different Emissivities

	Thermocouple 1		Thermocouple 2		
Repeat	**A**	**B**	**A**	**B**	**Average**
Pr, Heat Flux (W/m^2)	1.70E+06	1.92E+06	1.54E+06	2.14E+06	1.82E+06
Apparent Temp, ε=0.1	4160	4287	4056	4405	4227
Apparent Temp, ε=0.3	3161	3258	3082	3347	3212
Apparent Temp, ε=0.5	2782	2867	2713	2946	2827
Apparent Temp, ε=1.0	2339	2411	2281	2477	2377

The results suggest that the apparent temperature of the plume is between 2400-4200 K, lower than the expected value suggested by the literature. To look at this temperature range in more detail, a high melting point alloy was used to gain a lower limit for the temperature range, narrowing the range quoted above.

The melting point of tungsten is commonly accepted to be highest of all metals (3673.15 K (3,400˚C)). An experiment was carried out in which a tungsten wire was placed over a button in the furnace (as shown in Figure 6.22). The torch was then struck off, raised, and allowed to run for approximately 2 seconds. Ideally, the wire would be placed in the middle of the torch plume at a similar position to the positioning of the thermocouple. However, this would interfere with the strike-off procedure, in which the torch must be close to the button (between 1 and 2 cm). Measuring the exact distance that has been melted by the torch (defined as 'X' in Figure 6.22) is difficult as once broken the wire springs back, although it was possible to ascertain that this is approximately 10 cm.

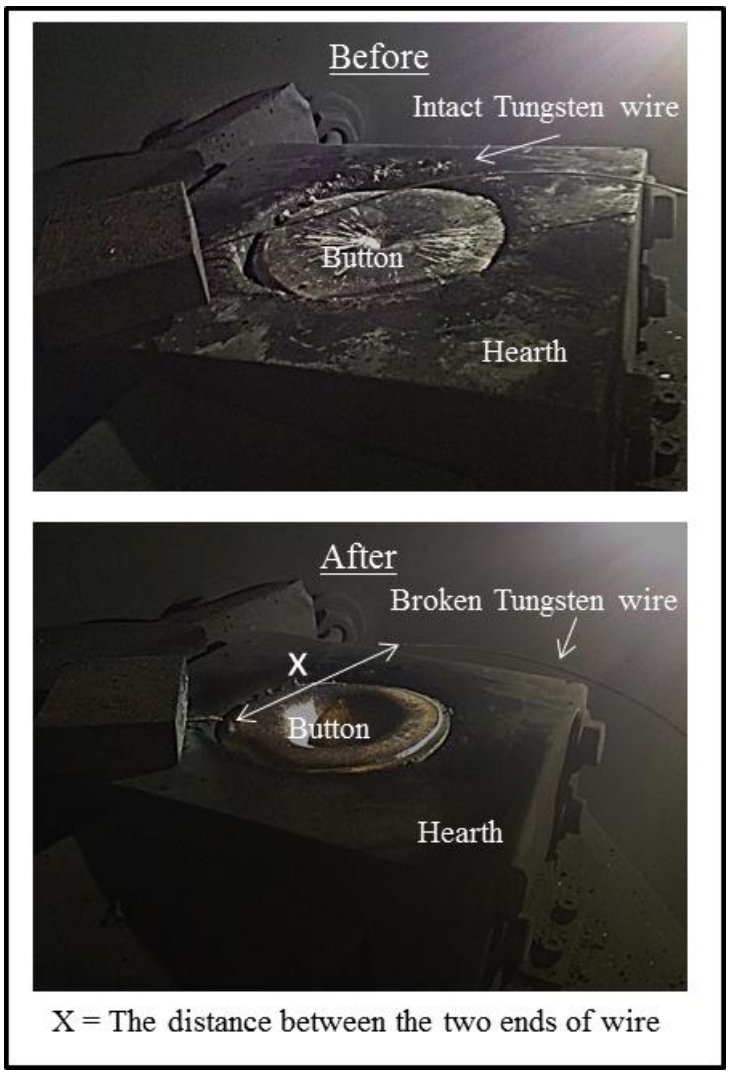

Figure 6.22: Photographs of the tungsten wire before and after the plasma torch was applied

From this is can be concluded that a large proportion of the bottom of the plasma plume reaches 3673.15 K. This suggests that the temperature range is more likely to be at the upper end of that calculated (i.e. the emissivity is between 0.3 and 0.1).

However it is difficult to pin point exactly what the emissivity (or more likely a range of emissivities) truly were. In other literature, more high-tech thermal imaging cameras are often discussed as measuring an 'apparent', rather than 'true', temperature as emissivity effects the amount of radiation energy given off from a surface [113]. A Spectro-pyrometer could be used for such applications, as it measures the temperature

and emissivity simultaneously [114]. For this work copper was used to allow all possible wavelengths to be observed, as there is no window to block some wavelengths and it is not influenced by the range of a detector.

This work has shown that there are limitations to this technique also: despite the tube, there is hot gas flowing around which may cause errors, the temperature rises are small and it is hard to mount everything precisely in the furnace, Also, the plasma plume is not instantly at its full length, as the torch rises fairly slowly.

6.4.2 Radiation Flux Density Calculations

The calculation of the radiation flux density does not rely on knowing the emissivity of the plasma plume and it is this value that was of most interest in this report.

Two things of particular interest can be calculated from the Pr, shown in Table 6.3:

1. The percentage of input Power that is lost as Radiation to the furnace,
2. The Radiation Flux on the surface of the Hearth.

6.4.2.1 The percentage of input Power that is lost as Radiation to the furnace

To address statement one the Radiation Flux must be converted to a Radiation Power, by multiplying it by the surface area of the plasma plume.

$$\boldsymbol{PR = \mathrm{Pr} * A_p = \mathrm{Pr} * 2\pi r_p * H} \qquad \textbf{Equation 6.9}$$

Where PR (W) and Pr (W/m^2) are the radiation power and radiation flux from the plasma plume respectively, A_p (m^2) is the Area of the plume, r_p (m) is the radius of the plasma plume and H (m) is the height of the plume.

The value for H can be worked out from the torch height, in this case was found to be 16cm, however r_p is harder to measure. A sensible estimate would be that r_p is in the range of 1-5 cm, calculated from a range of PAM melt videos (using image processing software). This would result in a range of A_p between 0.005-0.0503 m^2 and PR between $9x10^3$ -$9x10^4$ W.

The plume Radius, $r_{p,}$ is hard to verify however a closer estimate is possible using the equation derived by T.Iwao and T.Inaba in 2002, which was used in their work to calculate Current Density of a torch with a given radius and current input.

$$J = \frac{I}{\pi {r_p}^2} \qquad \textbf{Equation 6.10}$$

By using the average current density calculated in the previous section (90,000 A/m^2) and the current used for the radiation experiment (Approx. 500 A), it was possible to estimate r_p as being 0.04 m (4 cm). Based on this the Ap would be 0.0402 m^2 and the subsequent PR is $7x10^4$ W. It is felt by the author that this radius is potentially an over estimate (it would give a plume diameter of 0.08 m), although is possible. It seems high when compared to the track width calculated previously of 5.5 cm. However the Current Density peak is shown to be between 0 and 5 cm from the plume centre, and given previous research finding a peak at 3.6 cm for their conditions, it is possible this is the same for those shown here also (more points could prove or disprove this).

The percentage radiation can be easily worked out from here. Given that the total power is 110,000 W (based on recorded values of 220 V and 500 A), the percentage radiation power is approximately between 8-80% (this would be 65% using the r_p of 4cm).

6.4.2.2 The Radiation Flux on the surface of the Hearth

The radiation flux on the hearth surface, $P_{rH,}$ is worked out directly from P_r using the view factor, $F_{p\rightarrow h}$, between the plasma plume and the hearth. The view factor in this case is based on a cylinder (the plume) and a point (the hearth) at its base, a radial distance from the edge of the cylinder. The formulation of this view factor and the equations used are included in Appendix B and is used to calculate the radiation flux on the hearth surface as shown below:

$$\boldsymbol{P_{rH} = P_r * F_{p\rightarrow h}(r)} \qquad \textbf{Equation 6.11}$$

(i.e. the Radiation flux at the hearth is equal to the radiation flux from the plume multiplied by the view factor between the plume and hearth as a function of radius from the plume edge.)

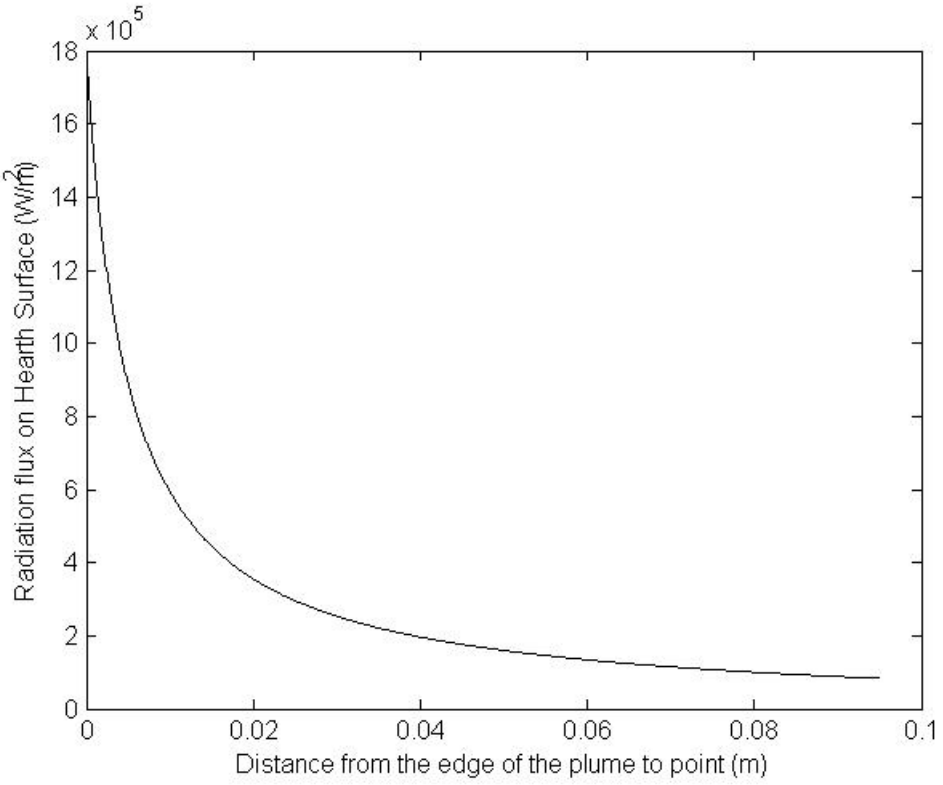

Figure 6.23: Radiation Flux on the Hearth Surface from the plume edge

Figure 6.23 shows how the radiation flux on the surface of the hearth decreases fairly significantly with distance from the edge of the plume. These results suggest that the assumption that all heat input into the melt pool is via conduction or convection made by most models is fairly inaccurate, as even at the edge of a skull the radiation flux is $1x10^5$ W/m^2.

6.4.2 Possible Experimental Errors

In addition to previous errors mentioned, the type-K thermocouples used should not be considered to be error free, as there are recognised errors in using a thermocouple that are inherent in the device itself. In general most type K thermocouples have an error of ±2.22˚C at most, assuming there are no additional reasons for errors to occur; for example inhomogeneities in the thermocouple material (a good summary of these are given by M.Capari and S.Garribba[115]).

During the experiment the wires connecting the thermocouple to the data acquisition box were wrapped in glass fibre. The hope was to shield them from temperatures that would cause the coating on the wire to melt and stop any miss-readings caused by the wires heating up. However, it is still possible that whilst the torch was on the wires heated up.

Finally, reports have suggested that for some instances temperatures lower than expected may be measured. This has been put down to radiation losses from the thermocouple to the surrounding environment [116, 117]. However, these reports focus on measuring hot gas from forest fires where the difference between the surrounding temperatures and the thermocouple are significantly higher.

7) Conclusions and Future Work

7.1 Conclusions

- The effect of the variables in the hearth are fairly complex, although at this stage some conclusions can be made:
  - Torch Current (given a constant voltage) was found to be directly proportional to melt pool size and energy within the melt pool. There was no evidence to show that the efficiency of the torch varied with torch current.
  - An optimum Torch Height seems to be apparent, looking at both the estimated energy and measured area of the melt pool formed. This was explained in part by the torches energy efficiencies. By looking at the melt pool energy it was found that the short arc length was the most efficient in the early stages (100 seconds) and the least efficient in the latter stages (800 seconds). In addition that the converse was true for the 'long' arc length.
  - There is a noticeable increase in melt pool size and energy with the use of insulation in the early stages for Ti-6-4. However it was seen to be less for TiAl possibly due to higher thermal conductivity of this alloy. This research could suggest the use of insulation in the hearth may not be as effective as previously thought, although it is suggested that this is due to only the bottom of the skull, and not the sides, being insulated.

- It was shown that voltage difference measurements can be taken and used to examine the current densities in a plasma plume.

- From this it was seen that most of the current enters the plate in approximately 25 mm from the plume centre and the resultant Lorentz Force was shown to be close to that of the buoyancy force.
- Examination of the beta transus isotherms and optimisations of parameters using equations formulated by Grong and a CFD model, suggested the radius of the plasma plume when it meets the anode is approximately 5.5 cm.
- The comparison of these models with measured melt pool dimensions also provided a basis for depth estimations to be carried out.
- In regards to energy losses from the plume, radiation was shown to be a fairly significant form of thermal energy loss from the plume (between 8-50% of the input power, dependent on plume dimensions). However it is also a contributing factor for heat input on the ingot surface and it is suggested that it is included in future models.

7.2 Future Work

7.2.1 Pre-treatment of plate

Before applying the torch in future sensor experiments in the furnace, a surface treatment could be carried out on the plate. For instance, one group of researchers polished the surface of their plate with emery paper before removing any further material on the surface with 3%HF+35%HNO_3 prior to being welded[52]. This is a common practice for titanium welding to remove any grease from the surface to help prevent reaction and hence the formation of brittle phases. If done immediately before being put in the furnace, this may also to a certain extent serve to remove the oxide layer on the surface.

7.2.2 Increase the number of voltage points in plate

As discussed in the results for the voltage trial, for the current density to be more accurately calculated, there needs to be as many voltage data points with distance as possible. The results show a fairly steep gradient in the voltage difference in the centre of the plate compared with the outside edge (See Figure 5.12). Therefore for future experiments it would be worthwhile concentrating on the voltage wires near the torch centre, particularly between 0 and 5 cm from the plume centre, thus getting a higher density of readings in this region.

7.2.3 Fluid Flow

As many of the PAM furnaces across TIMET, and the titanium industry as a whole, operate with large variations in torch power, it would be interesting to see how that affects the Lorentz force. So, in addition to more voltage points, repeats with different torch currents would be appropriate to look at. Especially in order to assess whether the distribution of current in the torch is the same at high and low torch currents.

7.2.4 Depth Measurements

The depth of the melt pool would be a useful measurement to have in order to more accurately measure the volume and hence energy within a melt pool. Although attempts have been made to estimate it using models and measurements further validation would be worthwhile with further experiments.

7.2.5 Multiple Thermocouples

The addition of more thermocouples placed at different points along the height of the plasma plume would allow for multiple, directly comparable, sets of data. If possible these would be housed within one container, in replacement to the ceramic tube. This is particularly important for an experiment such as this where repeats are difficult due to there being limited access in the furnace to accurately measure distance between the plume and target for each repeat.

7.2.6 Accurate 'Control' thermocouple readings

Numerous reports suggest errors in temperature readings are reduced when aspirated thermocouples are used [116], however this is because they remove the effect of radiation [118]. As a result they would not be useful for radiation measurements. However, they could allow the temperature of the gas close to the tube to be measured, and so acting as a control. In which case it may be possible assess the radiation effect with more certainty.

8) References

1. G.Li, J.S.Chou., X.Huang, K.M.Kelkar and Y.Pang. *Modeling of a Reversed-Polarity Plasma Torch in Titanium Hearth Melting Process*. in *CTC*. 1999.
2. X.Huang, J.S.Chou., and Y.Pang, *Modeling of plasma arc cold hearth melting and refining of Ti alloys*, in *Liquid Metal Processing and Casting*, M.B. Alec Mitchell. Lisa Ridgway, Editor 1999: Santa Fe, New Mexico. p. 224-243.
3. Hub, P. *Topic guide to: Tourism*. 2006; Available from: http://www.statistics.gov.uk/hub/people-places/people/tourism.
4. Airbus. *Navigating the Future* 2012; Available from: http://www.airbus.com/company/market/forecast/?eID=dam_frontend_push&docID=25773.
5. Kilroy, C. *Special Report: United Airlines Flight 232* 2013 [cited 2013 20/06/2013]; Available from: http://www.airdisaster.com/special/special-ua232.shtml.
6. TIMET. *TIMET: First in Titanium Worldwide*. 2013 11/11/2013]; Available from: http://www.timet.com/.
7. S.Seong, O.Younossi., B.W.Goldsmith, *Titanium*, in *Industrial Base, Price Trends, and Technology Initiatives*2009, RAND Corporation. p. 128.
8. Boulos, M.I., *Thermal plasma processing.* Plasma Science, IEEE Transactions on, 1991. **19**(6): p. 1078-1089.
9. Venkatramani, N., *Industrial plasma torches and applications.* CURRENT SCIENCE-BANGALORE-, 2002. **83**(3): p. 254-262.
10. VFE. *Plasma Arc Melting*. The Ultimate in Vacuum, The Ultimate in Service 2013 04/11/13]; Available from: http://www.vfe.co.uk/Products/Melting%20%26%20Casting/plasmaarcmelting.html.
11. Bakish, R., *The state of the art in electron beam melting and refining.* JOM Journal of the Minerals, Metals and Materials Society, 1991. **43**(5): p. 42-44.
12. Blackburn, M.J. and D.R. Malley, *Plasma arc melting of titanium alloys.* Materials & Design, 1993. **14**(1): p. 19-27.
13. Ward, R.M., *Sensing and Controlling the Plasma Arc Cold-Hearth Refining Process*, in *Metallurgy and Materials* 1999, University of Birmingham p. 205.
14. Xu, X., et al., *Simulation of Temperature Field Distribution in Melting TiAl Alloy by PAM Process.*
15. Consarc, *Vacuum Arc Remelting Furnaces*, 2013.
16. Bellot, J.P., et al., *Dissolution of hard-alpha inclusions in liquid titanium alloys.* Metallurgical and Materials Transactions B, 1997. **28**(6): p. 1001-1010.
17. Zhang, Y., et al., *An Investigation on Electron Beam Cold Hearth Melting of Ti64 Alloy.* Rare Metal Materials and Engineering, 2008. **37**(11): p. 1973-1977.
18. Akhonin, S.V., et al., *Mathematical modeling of aluminum evaporation during electron-beam cold-hearth melting of Ti-6Al-4V ingots.* Metallurgical and Materials Transactions B, 2003. **34**(4): p. 447-454.
19. Sparks, N., et al., *Plasma arc remelting of steels and nickel-based superalloys.* Le Journal de Physique IV, 1993. **3**(C7): p. 7-7.
20. K.O.Yu, F., P.Spadafora, J.M.Hjelm, B.Matin, S.Fellows and M.Jacques. *Plasma Arc melting of Titanium Alloys for Non-Rotation Component Applications*. in *Liquid Metal Processing and Casting*. 2001. Santa FE, new Mexico.

21. Kothari, K., R. Radhakrishnan, and N.M. Wereley, *Advances in gamma titanium aluminides and their manufacturing techniques.* Progress in Aerospace Sciences, 2012. **55**(0): p. 1-16.
22. Bowen, P., R.A. Chave, and A.W. James, *Cyclic crack growth in titanium aluminides.* Materials Science and Engineering: A, 1995. **192–193, Part 1**(0): p. 443-456.
23. Yang, Z.-j., et al., *Numerical simulation of temperature distribution and heat transfer during solidification of titanium alloy ingots in vacuum arc remelting process.* Transactions of Nonferrous Metals Society of China, 2010. **20**(10): p. 1957-1962.
24. G.Reiter, W.S., P.Wurzinger, S.Zinner. *Optimization and Detailed Validation of VAR Model*. in *LMPC*. 2005. Santa Fe.
25. R.S.Minisandram, M.J.Arnold and R.L.Williamson., *VAR Pool Depth Measurement and Simulation for a Large Diameter Ti-6Al-4V Ingot,* in *LMPC*. 2005. Santa Fe. p. 1-6.
26. F.Zanner, R.Williamson., R.Erdmann. *On the Origin of Defects in VAR Ingots*. in *LMPC*. 2005. Santa Fe.
27. R.L.Williamson, G.J.Shelmidine., J.P.Maroone. *Current Profiles During VAR of Ti-6Al-4V*. in *LMPC*. 2005. Santa Fe.
28. Kondrashov, E., et al., *Calculation of the molten pool depth in vacuum arc remelting of alloy Vt3-1.* Journal of Engineering Thermophysics, 2007. **16**(1): p. 19-25.
29. Davidson, P., X. He, and A. Lowe, *Flow transitions in vacuum arc remelting.* Materials science and technology, 2000. **16**(6): p. 699-711.
30. Nair, B.G. and R. Ward, *An analysis of the use of magnetic source tomography to measure the spatial distribution of electric current during vacuum arc remelting.* Measurement Science and Technology, 2009. **20**(4): p. 045701.
31. Biamino, S., et al., *Electron beam melting of Ti–48Al–2Cr–2Nb alloy: Microstructure and mechanical properties investigation.* Intermetallics, 2011. **19**(6): p. 776-781.
32. Hernandez, J., et al., *Microstructures for Two-Phase Gamma Titanium Aluminide Fabricated by Electron Beam Melting.* Metallography, Microstructure, and Analysis, 2012. **1**(1): p. 14-27.
33. Bertram, L., et al., *The macroscale simulation of remelting processes.* JOM, 1998. **50**(3): p. 18-21.
34. J.J.Beaman, et al., *Vacuum Arc Remelting Pool Power Control*, in *LMPC*, A.M. P.D.Lee, J-P Bellot and A.Jardy, Editor 2007: Nancy France
35. Williamson, R.L., et al., *Modern control strategies for vacuum arc remelting of segregation sensitive alloys.* Superalloys 718, 625, 706 and Various Derivatives, 1997: p. 37-46.
36. Mitchell, A., *The electron beam melting and refining of titanium alloys.* Materials Science and Engineering: A, 1999. **263**(2): p. 217-223.
37. Lee, P.D., P.N. Quested, and M. McLean, *Modelling of Marangoni Effects in Electron Beam Melting.* Philosophical Transactions: Mathematical, Physical and Engineering Sciences, 1998. **356**(1739): p. 1027-1043.
38. Chu, S.C. and S.S. Lian, *Numerical analysis of temperature distribution of plasma arc with molten pool in plasma arc melting.* Computational Materials Science, 2004. **30**(3–4): p. 441-447.
39. Aithal, S.M., et al., *Numerical model of a transferred plasma arc.* Journal of Applied Physics, 1998. **84**(7): p. 3506-3517.

40. Chen, X. and H-P. Li, *Three-dimensional flow and heat transfer in thermal plasma systems.* Surface and Coatings Technology, 2002. **171**(1–3): p. 124-133.
41. Hur, M., et al., *Numerical analysis and experiments on transferred plasma torches for finding appropriate operating conditions and electrode configuration for a waste melting process.* Thin Solid Films, 2001. **390**(1–2): p. 186-191.
42. Iwao, T. and T. Inaba, *Plasma length on characteristics of DC argon plasma torch arc.* Vacuum, 2002. **65**(3–4): p. 299-304.
43. Iwao, T., et al., *Radiation power emitted from Ar torch short plasma as a function of in-put power in several kW.* Vacuum, 2000. **59**(1): p. 88-97.
44. LLC, R.S. *Plasma Arc Melting (PAM)*. 2010; Available from: http://www.retechsystemsllc.com/EN/pam.html.
45. Max P.Schlienger, R., Inc., *Plasma Hearth Melting of Titanium and Titanium Alloys*, 2005.
46. K.B.Bisen, et al., *Computation and Validation of Weld Pool Dimensions and Temperature Profiles for Gamma TiAl.* Metallurgical and Materials Transactions, 2003. **34A**: p. 2273-2279.
47. ToolBox, T.E. *Thermal Conductivity of some common Materials and Gases*. The Engineering ToolBox 2013 12/11/2013]; Available from: http://www.engineeringtoolbox.com/thermal-conductivity-d_429.html.
48. Kruger, U. *Arc Welding Processes: TIG, Plasma Arc, MIG*. TALAT Lecture 1994 12/11/2013]; Available from: http://www.alueurope.eu/talat/lectures/4201.pdf.
49. Cremers, C.J. and E. Pfender, *Temperatures in a plasmajet.* International Journal of Heat and Mass Transfer, 1968. **11**(7): p. 1203-1206.
50. Grong, Ø. and D. Grong, *Metallurgical modelling of welding*. Vol. 2. 1997: Institute of materials London.
51. Leyens, C. and M. Peters, *Titanium and titanium alloys*2003: Wiley Online Library.
52. Wang, S. and X. Wu, *Investigation on the microstructure and mechanical properties of Ti–6Al–4V alloy joints with electron beam welding.* Materials & Design, 2012. **36**(0): p. 663-670.
53. TIMET. *TIMET Articles*. 14/11/2013]; Available from: http://www.timet.com/component/content/article/14-titanium-101/44-var-vacuum-arc-remelt-process.
54. T.J.Watt, E.M.Taleff., F.Lope, J.Beaman, R.Williamson, *Solidification Mapping of a Nickel Alloy 718 Laboratory VAR Ingot*, in *LMPC*, A.J. M.J.M.Krane, R.L.Williamson and J.J.Beaman, Editor 2013, Wiley: Austin, Texas. p. 261-270.
55. R.M. Ward, T.P.Johnson., M.H. Jacobs., *An Experimental Investigation of Heat Transfer in the Crucible and Ingot During PACHR of Inconel Alloy 718.* 1999.
56. Li, B., et al., *Two dimensional modeling of momentum and thermal behavior during spray atomization of γ-TiAl.* Acta Materialia, 1996. **44**(6): p. 2409-2420.
57. ASM Aerospace Specification Metals, i., *Titanium Ti 6AL 4V - AMS 4911*, 2014.
58. Boyer, R.F. and E. Collings, *Materials properties handbook: titanium alloys*1994: ASM international.
59. Azom.com. *Titanium Alloys - Physical Properties*. 2013 11/11/2013]; Available from: http://www.azom.com/article.aspx?articleid=1341.
60. Bartolotta, P.A. and D.L. Krause. *Titanium aluminide applications in the high speed civil transport*. in *Second International Symposium on Gamma Titanium*

Aluminides(ISGTA) 1999 as held in conjunction with the TMS 1999 Annual Meeting. 1999.
61. Seshacharyulu, T., et al., *Hot deformation and microstructural damage mechanisms in extra-low interstitial (ELI) grade Ti–6Al–4V.* Materials Science and Engineering: A, 2000. **279**(1–2): p. 289-299.
62. Filippini, M., et al., *Defect tolerance of a gamma titanium aluminide alloy.* Procedia Engineering, 2011. **10**(0): p. 3677-3682.
63. Hénaff, G. and A.-L. Gloanec, *Fatigue properties of TiAl alloys.* Intermetallics, 2005. **13**(5): p. 543-558.
64. Yamauchi, S. and H. Shiraishi, *Homogeneity and mechanical properties of TiAl.* Materials Science and Engineering: A, 1992. **152**(1–2): p. 283-287.
65. Wang, H., G. Djambazov, and K. Pericleous, *Numerical study of crucial parameters in tilt casting for titanium aluminides.* Research & Development, 2011.
66. Godfrey, B. and M.H. Loretto, *Origins of heterogeneities in plasma melted ingots of γ-TiAl.* Materials Science and Engineering: A, 1999. **266**(1–2): p. 115-122.
67. Naka, S., *Advanced titanium-based alloys.* Current Opinion in Solid State and Materials Science, 1996. **1**(3): p. 333-339.
68. Nadella, R., et al., *Macrosegregation in direct-chill casting of aluminium alloys.* Progress in Materials Science, 2008. **53**(3): p. 421-480.
69. Gil, F., et al., *Formation of α-Widmanstätten structure: effects of grain size and cooling rate on the Widmanstätten morphologies and on the mechanical properties in Ti6Al4V alloy.* Journal of alloys and compounds, 2001. **329**(1): p. 142-152.
70. Reitz, J., C. Lochbichler, and B. Friedrich, *Recycling of gamma titanium aluminide scrap from investment casting operations.* Intermetallics, 2011. **19**(6): p. 762-768.
71. R.Knight, R.W.Smith., and D.Apelian *Application of plasma arc melting technology to processing of reactive metals.* International Materials Reviews, 1991.
72. Chinnis, W.R., *Plasma cold hearth melting of titanium in a production furnace.* Titanium 1990: Products and Applications., 1990. **2**: p. 830-835.
73. Mitchell, A., *Melting, casting and forging problems in titanium alloys.* Materials Science and Engineering: A, 1998. **243**(1–2): p. 257-262.
74. Shamblen, C. and G. Hunter. *Titanium base alloys clean melt process development*. in *Proceedings of the 1989 Vacuum Metallurgy Conference on the Melting and Processing of Specialty Materials*. 1989.
75. Goldstein, R.J., et al., *Heat transfer—A review of 2005 literature.* International Journal of Heat and Mass Transfer, 2010. **53**(21–22): p. 4397-4447.
76. Hatami, N., et al., *Modeling of hot tearing formation during solidification.* Journal of Materials Processing Technology, 2008. **205**(1–3): p. 506-513.
77. Malinov, S. and W. Sha, *Modeling thermodynamics, kinetics, and phase transformation morphology while heat treating titanium alloys.* JOM, 2005. **57**(9): p. 42-45.
78. Benard, C., D. Gobin, and A. Zanoli, *Moving boundary problem: heat conduction in the solid phase of a phase-change material during melting driven by natural convection in the liquid.* International Journal of Heat and Mass Transfer, 1986. **29**(11): p. 1669-1681.

79. Samarskii, A.A., et al., *Numerical simulation of convection/diffusion phase change problems—a review.* International Journal of Heat and Mass Transfer, 1993. **36**(17): p. 4095-4106.
80. Eskin, D.G., et al., *Structure formation and macrosegregation under different process conditions during DC casting.* Materials Science and Engineering: A, 2004. **384**(1–2): p. 232-244.
81. Powell, R.W. and R.P. Tye, *The thermal and electrical conductivity of titanium and its alloys.* Journal of the Less Common Metals, 1961. **3**(3): p. 226-233.
82. Wang, H.-X., et al., *Three-dimensional modeling of heat transfer and fluid flow in laminar-plasma material re-melting processing.* International Journal of Heat and Mass Transfer, 2006. **49**(13–14): p. 2254-2264.
83. R.M.Ward, D.M.Sevchenko., *Liquid Metal Pool Behaviour during the VAR of Inconel 718*, in *LMPC*, A.M. P.D.Lee, J-P Bellot and A.Jardy, Editor 2007: Nancy France. p. 25-36.
84. J.A.Elliott, *Plasma Kinetic Theory*. Plasma Physics, ed. R. Dendy1993.
85. M.H.Jacobs, R.M.W.a., *Electromagnetic Aspects of Plasma Melting* in *Electromagnetic Processing of Materials* 1997: Paris p. 197-202.
86. Lu, F., et al., *Modeling and finite element analysis on GTAW arc and weld pool.* Computational Materials Science, 2004. **29**(3): p. 371-378.
87. Boulos, M.I., P. Fauchais, and E. Pfender, *Thermal plasmas*. Vol. 1. 1994: Springer.
88. Trelles, J., et al., *Arc plasma torch modeling.* Journal of thermal spray technology, 2009. **18**(5-6): p. 728-752.
89. Jenista, J., J.V. Heberlein, and E. Pfender, *Numerical model of the anode region of high-current electric arcs.* Plasma Science, IEEE Transactions on, 1997. **25**(5): p. 883-890.
90. G.Li, J.S.Chou., X.Huang, K.M.Kelkar and Y.Pang. *Modeling of a Reversed-Polarity Plasma Torch in Titanium Hearth Melting Process*. in *Liquid Metal Processing and Casting* 1999. Santa Fe, New Mexico.
91. Ushio, M., D. Fan, and M. Tanaka, *Contribution of Arc Plasma Radiation Energy to Electrodes (Physics, Process, Instrument & Measurements).* 1993.
92. Lee, P.D., et al., *Multiscale modelling of solidification microstructures, including microsegregation and microporosity, in an Al–Si–Cu alloy.* Materials Science and Engineering: A, 2004. **365**(1–2): p. 57-65.
93. Kelkar, K.M., S.V. Patankar, and A. Mitchell. *Computational modeling of the electroslag remelting (esr) process used for the production of ingots of high-performance alloys*. in *Proceeding in International Symposium on Liquid metal Processing and Casting, Santa Fe, USA*. 2005.
94. K.T.Trinh, *On the Critical Reynolds Number For Transition From Laminar To Turbulent Flow.* 2011.
95. Paradis, P.F., T. Ishikawa, and S. Yoda, *Non-Contact Measurements of Surface Tension and Viscosity of Niobium, Zirconium, and Titanium Using an Electrostatic Levitation Furnace.* International Journal of Thermophysics, 2002. **23**(3): p. 825-842.
96. Hruby, V., et al., *Methane Arcjet Development.* Paper AIAA: p. 97-3427.
97. Gallimore, S.D., *Operation of a High-Pressure Uncooled Plasma Torch with Hydrocarbon Feedstocks*, 1998, Virginia Polytechnic Institute and State University.
98. Solonenko, O.P., *Thermal plasma torches and technologies*. Vol. 1. 2000: Cambridge Int Science Publishing.

99. O.Grong, *Metallurgical Modelling of Welding* Second Edition ed. Materials Modelling Series1994, 1 Carlton House Terrace, London, SW1Y 5DB: The Institute of Materials
100. Boivineau, M., et al., *Thermophysical Properties of Solid and Liquid Ti-6Al-4V (TA6V) Alloy.* International Journal of Thermophysics, 2006. **27**(2): p. 507-529.
101. Nair, B., H. Holst, Editor 2013.
102. Brewer, W.D., *Effect of Thermocouple Wire size and configuration on internal temperature measurements in a Charring Ablator.* NASA Technical Note, 1967.
103. R.M. Ward, T.P.J., M.H. Jacobs., *An Experimental Investigation of Heat Transfer in the Crucible and Ingot During PACHR of Inconel Alloy 718*, in *Liquid Metal Processing and Casting* L.R. A.Mitchell, M.Baldwin, Editor 1999.
104. Incropera, F.P., A.S. Lavine, and D.P. DeWitt, *Fundamentals of heat and mass transfer*2011: John Wiley & Sons Incorporated.
105. R.A.Person, H.Leuenberger., *Compliation of Radiation Shape Factors for Cylindrical Assembles.* The American Society of Mechanical Engineers, 1956.
106. Johnson, G.T. and I.D. Watson, *The determination of view-factors in urban canyons.* Journal of Applied Meteorology, 1984. **23**: p. 329-335.
107. Rea, S.N., *Rapid method for determining concentric cylinder radiation view factors.* AIAA Journal, 1975. **13**(8): p. 1122-1123.
108. Dozier, J. and J. Frew, *Rapid calculation of terrain parameters for radiation modeling from digital elevation data.* Geoscience and Remote Sensing, IEEE Transactions on, 1990. **28**(5): p. 963-969.
109. Dubayah, R. and P.M. Rich, *Topographic solar radiation models for GIS.* International Journal of Geographical Information Systems, 1995. **9**(4): p. 405-419.
110. Steyn, D.G., et al., *Determination of Sky View-Factors in Urban Environments Using Video Imagery.* 1986.
111. Lu, T., H. Stone, and M. Ashby, *Heat transfer in open-cell metal foams.* Acta Materialia, 1998. **46**(10): p. 3619-3635.
112. Weber, R.O., *Analytical models for fire spread due to radiation.* Combustion and Flame, 1989. **78**(3–4): p. 398-408.
113. Optotherm. *Emissivity in the Infrared*. 2014; Available from: http://www.optotherm.com/emiss-effects.htm.
114. Felice, R.A. and D.A. Nash, *Pyrometry of Materials With Changing, Spectrally-Dependent Emissivity–Solid & Liquid Metals.*
115. S.Garribba, M.C.a., *The Behaviour of Type K Thermcouples in Temperature Measurement: The chromel P Alumel Thermocuples.* Review of Scientific Instruments, 1971.
116. Shannon, K. and B. Butler. *A review of error associated with thermocouple temperature measurement in fire environments*. in *Second international wildland fire ecology an fire management congress and fifth symposium on fire and forest meteorology. American Meteorological Society, Orlando, FL*. 2003.
117. Walker, J. and B. Stocks, *Thermocouple errors in forest fire research.* Fire Technology, 1968. **4**(1): p. 59-62.
118. G.S.Campbell, *Measurement of Air Temperature Fluctuations with Thermocouples*, 1969: New Mexico.
119. Martinez, I. *Radiative View Factors*. 2013; Available from: http://webserver.dmt.upm.es/~isidoro/tc3/Radiation%20View%20factors.pdf.

Appendix A

One worry whilst carrying out the sensors experiment was that the voltage difference in the plate would lead to false readings for the thermocouples. The extent of this error was investigated by placing a 3.7 V battery between the thermocouples. The resultant change in temperature is approximately (3023) 7°C initially and 4.5°C after a period of a few seconds, as shown in the graph below. These results suggest that the effect of voltage can be safely discounted as having little effect for two reasons. Firstly the plasma torch produces a voltage in the plate in the region of tens of millivolts (almost 4000 times smaller than that produced by the battery) therefore the error caused will be much reduced. In addition the plasma torch produces temperatures of hundreds of Degrees Celsius; therefore an error below 10°C is relatively insignificant.

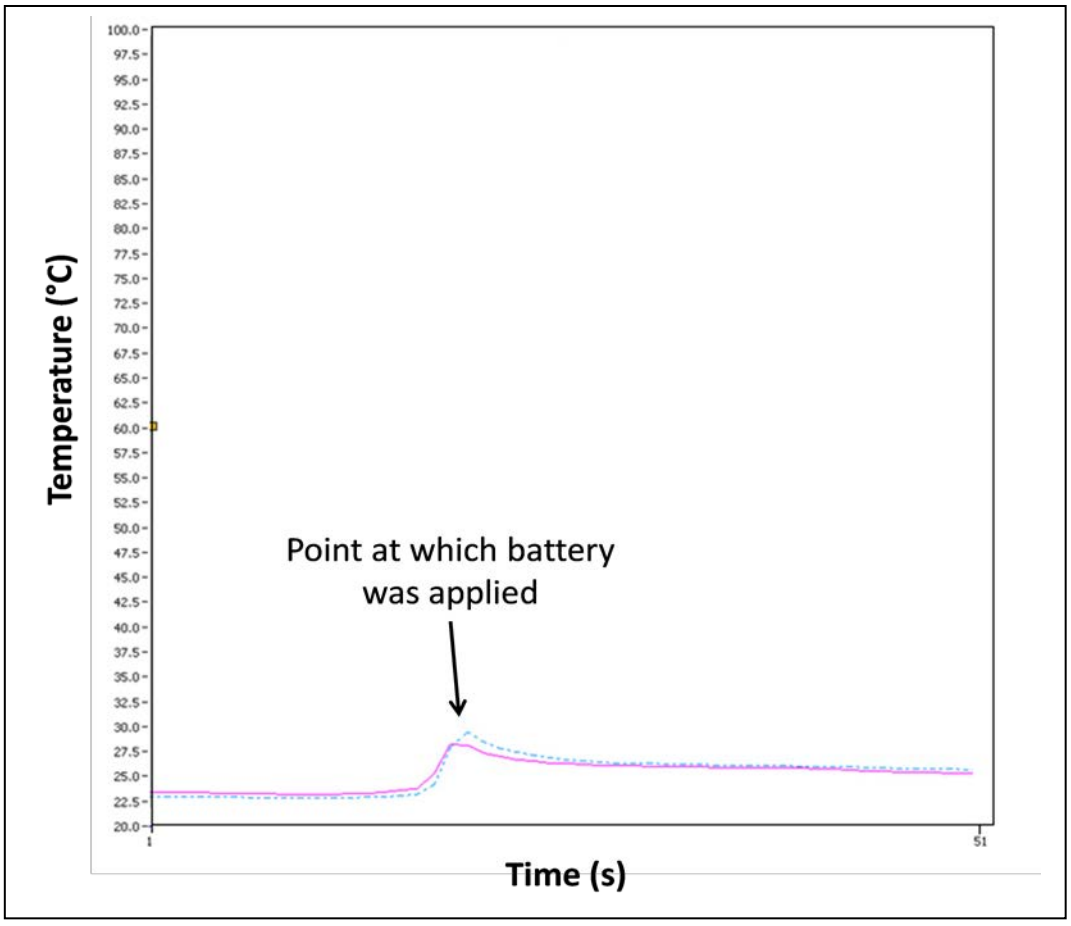

Figure A-1: Effect of voltage on temperature readings

Appendix B

The view factor describing the amount of radiation leaving the plume that hits a point on the melt pool is taken from H.Leuenberger and R.A.Person's [105] work. They compiled a number of radiation view factors for different cylindrical configurations. Of most interest for this research was that of a cylinder parallel to a plane. The View Factors are evaluated using integration of a strip 'a' along the plane using multiple differential elements of a, 'b' (Shown in Figure B-1). By looking at an element at the bottom of the cylinder (or top as the cylinder and plane are horizontally symmetrical), where $y \rightarrow 0$, the plane can be treated as a point.

This view factor is limited for use only when S is greater than r, (i.e. when the point is not directly under the plume) due to the use of $\cos^{-1}(x)$, where $x=R/S$. So that the results aren't complex, $-1<x<1$, therefore as neither R or S may be negative, $S>R$.

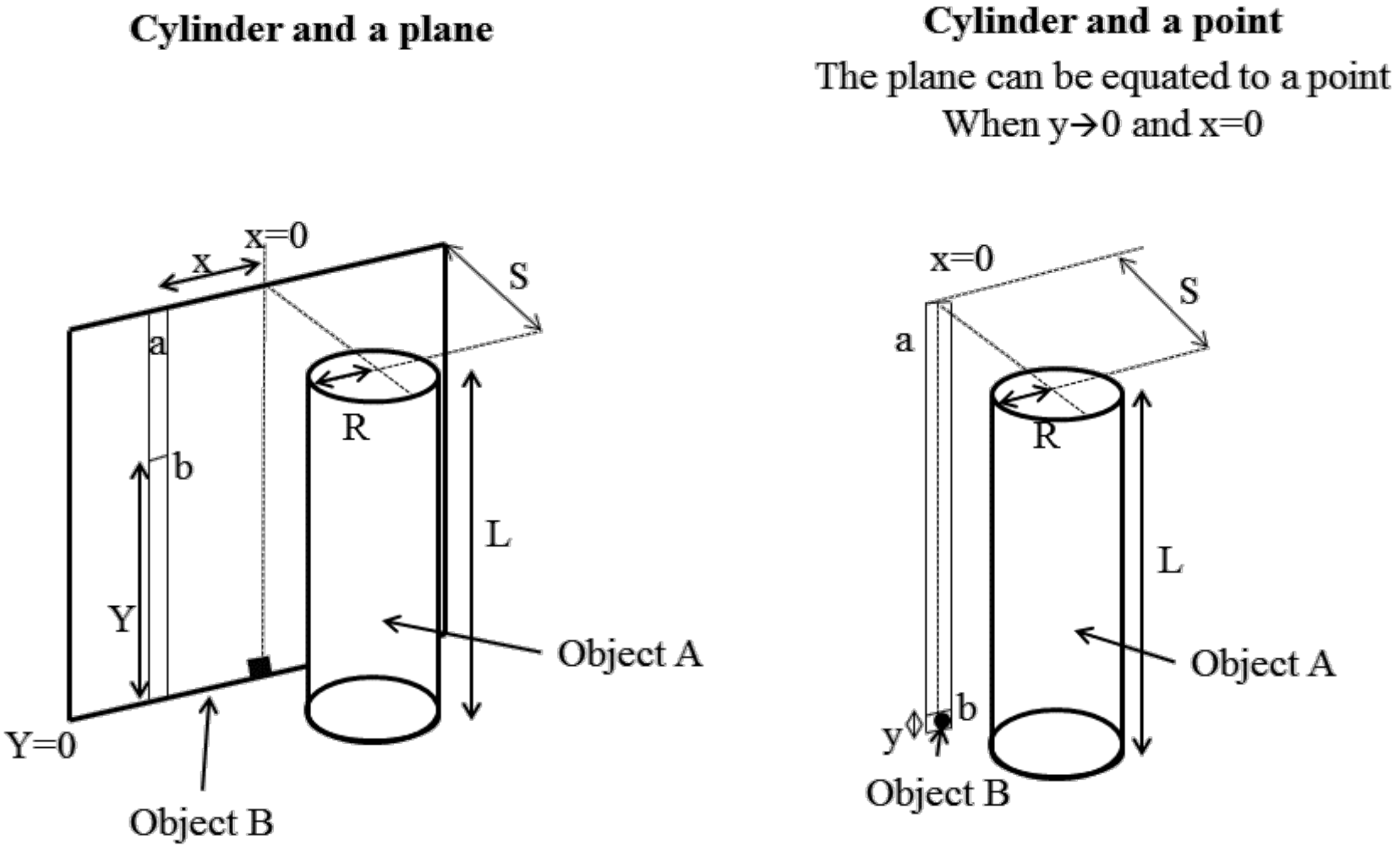

Figure B-1: Diagrams showing the dimensions for the calculation of the view-factor[51]

Appendix C

Table C-1: Showing the values for each repeat of the Furnace test where the thermocouples, distance between plume and thermocouple and furnace temperature were varied

TC	Furnace Temperature (°C)	Distance (cm)	View Factor*	Heating Rate (K/s)	Constants $(\varepsilon_T A)/(m_T C_p)$
1	800.00	50.00	0.0287	0.28	2.35E+03
2	800.00	50.00	0.0287	0.35	1.91E+03
3	800.00	50.00	0.0287	0.38	1.76E+03
1	800.00	50.00	0.0287	0.29	2.31E+03
2	800.00	50.00	0.0287	0.35	1.88E+03
3	800.00	50.00	0.0287	0.39	1.69E+03
1	800.00	50.00	0.0287	0.28	2.35E+03
2	800.00	50.00	0.0287	0.35	1.93E+03
3	800.00	50.00	0.0287	0.40	1.68E+03
1	800.00	37.30	0.0504	0.58	2.00E+03
2	800.00	37.30	0.0504	0.69	1.69E+03
3	800.00	37.30	0.0504	0.76	1.54E+03
1	800.00	37.30	0.0504	0.59	1.97E+03
2	800.00	37.30	0.0504	0.71	1.64E+03
3	800.00	37.30	0.0504	0.81	1.45E+03
1	800.00	37.30	0.0504	0.56	2.07E+03

2	800.00	37.30	0.0504	0.69	1.70E+03
3	800.00	37.30	0.0504	0.76	1.55E+03
1	900.00	37.30	0.0504	0.78	2.41E+03
2	900.00	37.30	0.0504	0.86	2.17E+03
3	900.00	37.30	0.0504	0.95	1.97E+03
1	900.00	37.30	0.0504	0.79	2.37E+03
2	900.00	37.30	0.0504	0.88	2.14E+03
3	900.00	37.30	0.0504	1.00	1.88E+03
1	900.00	37.30	0.0504	0.78	2.39E+03
2	900.00	37.30	0.0504	0.88	2.13E+03
3	900.00	37.30	0.0504	0.98	1.92E+03
1	900.00	46.80	0.0326	0.50	2.45E+03
2	900.00	46.80	0.0326	0.56	2.17E+03
3	900.00	46.80	0.0326	0.61	1.98E+03
1	900.00	46.80	0.0326	0.49	2.49E+03
2	900.00	46.80	0.0326	0.55	2.21E+03
3	900.00	46.80	0.0326	0.61	1.97E+03
1	900.00	46.80	0.0326	1.32	9.17E+02
2	900.00	46.80	0.0326	1.41	8.64E+02
3	900.00	46.80	0.0326	1.55	7.82E+02
1	1000.00	46.80	0.0326	0.73	2.54E+03
2	1000.00	46.80	0.0326	0.78	2.38E+03
3	1000.00	46.80	0.0326	0.85	2.17E+03
1	1000.00	46.80	0.0326	0.73	2.55E+03
2	1000.00	46.80	0.0326	0.78	2.37E+03
3	1000.00	46.80	0.0326	0.88	2.11E+03
1	1000.00	46.80	0.0326	0.69	2.68E+03

2	1000.00	46.80	0.0326	0.75	2.46E+03
3	1000.00	46.80	0.0326	0.83	2.24E+03
1	1000.00	32.10	0.0668	1.33	2.85E+03
2	1000.00	32.10	0.0668	1.41	2.68E+03
3	1000.00	32.10	0.0668	1.56	2.43E+03
1	1000.00	32.10	0.0668	1.30	2.92E+03
2	1000.00	32.10	0.0668	1.38	2.75E+03
3	1000.00	32.10	0.0668	1.49	2.54E+03
1	1000.00	32.10	0.0668	1.31	2.90E+03
2	1000.00	32.10	0.0668	1.39	2.72E+03
3	1000.00	32.10	0.0668	1.54	2.46E+03
				Average	2.19E+03
				Standard Deviation	3.72E+02

*Based on a furnace with the dimensions 0.18 m by 0.125 m and a parallel square to square view factor [119]

The rows highlighted in grey refer to the potential anomalies.

Table C-2: Dimensions of the oven and the thermocouple

Average Width of Furnace	0.1525
Diameter of Thermocouple	0.00625

The area of the circular thermocouple is equated to the area of a square, where the diameter is assumed to be equal to the width of the square.

Table C-3: Temperature rise of the control target over the time the door is open

Trial number	1	2	3	4	5	6	7	8	9
Rate of Temperature Rise (dT/dt)	0.030	0.070	0.008	0.027	0.014	0.037	0.022	0.017	0.004

Appendix D

View Factors derivations

For a Three Dimensional problem a solid angle is required to describe the area at a given distance from a point. This is similar to how an arc length S can be described by an angle and a given radius. This is demonstrated in Figure D-1 below.

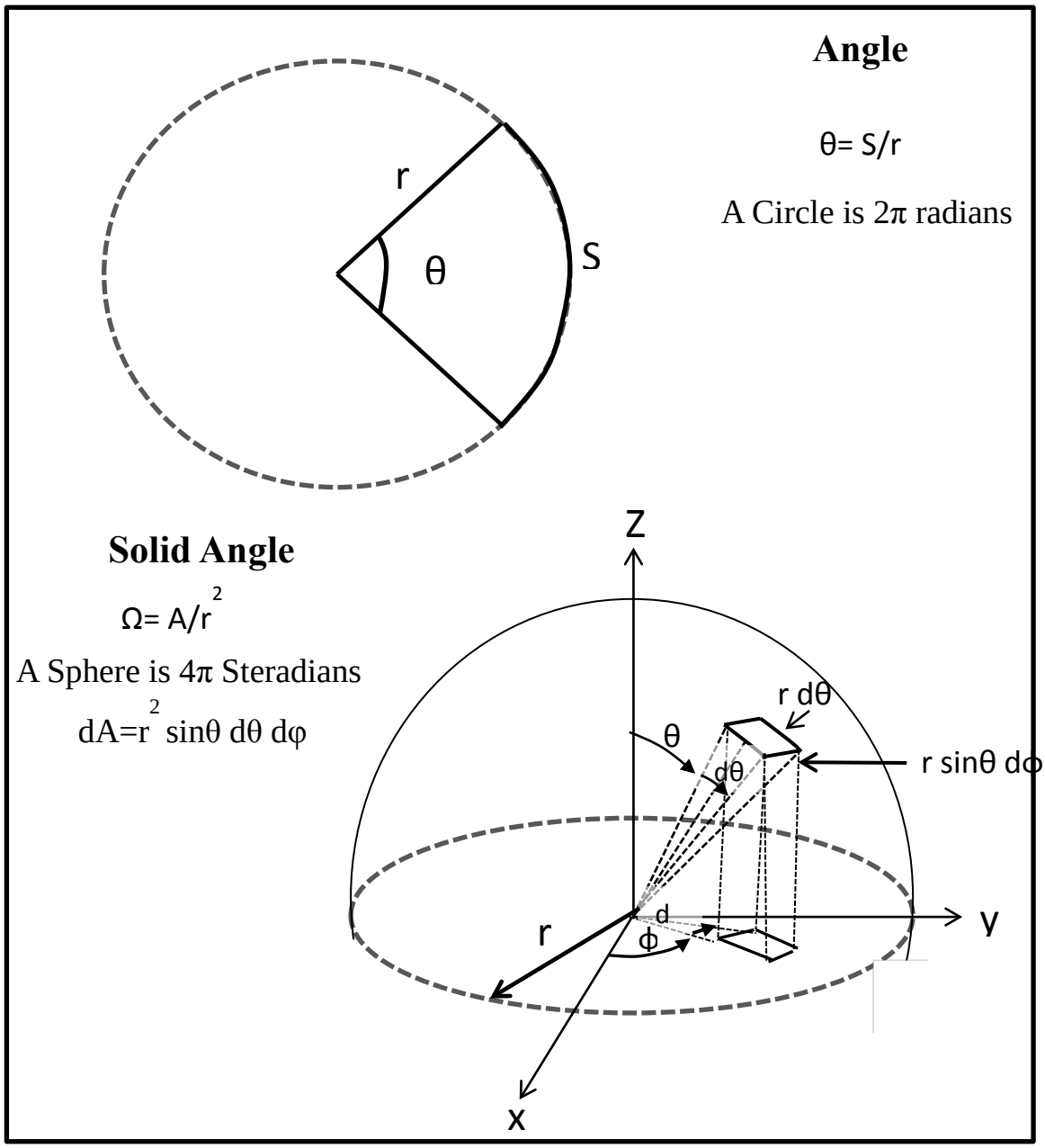

Figure D-1: The difference between an angle and a solid angle and the subsequential formulae

These solid angles can be used to calculate the view factor from one object to another by first calculating the radiation power intercepted by surface dA_2 coming from dA_1 (Figure D-2).

Radiation Intercepted = Radiance*Perpendicular area of dA_1*Solid Angle subtended by dA_2

$$= \varepsilon\sigma T^4 / \pi * \quad dA1\cos(\beta_1) \quad * \quad dA2\cos(\beta_1)/r_{12}^2$$

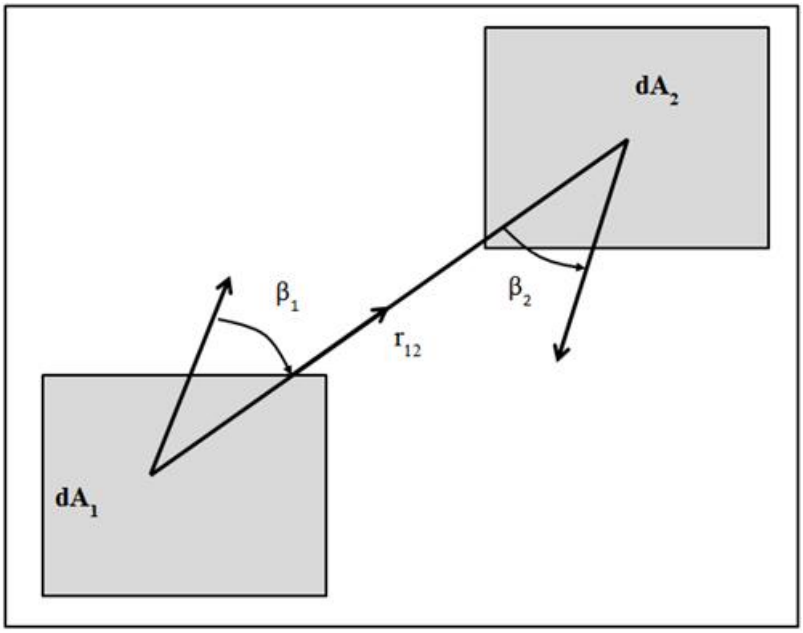

Figure D-2: Diagram showing the variables for calculating a general view factor

$$dF_{12} = \frac{Radiation\ Intercepted}{Total\ Radiation} = \frac{\cos(\beta_1)\, dA_2 \cos(\beta_1)}{\pi r_{12}^2}$$

For a set-up with two parallel disks, $dA_1 = dA_2 = \pi r_x^2$, $\beta 1 = 0$ and $r_{12} = L$ (the distance between two disks in m), therefore the above Equation becomes:

$$dF_{12} = \frac{r^2}{L^2}$$

This Equation only gives the view factor between two differential areas, however given the small area of the thermocouples in this case it provides a good approximation.

Using Tables of pre-calculated data a form for finite areas was found, the Equation for which is shown below. (Adapted from Equation in [119])

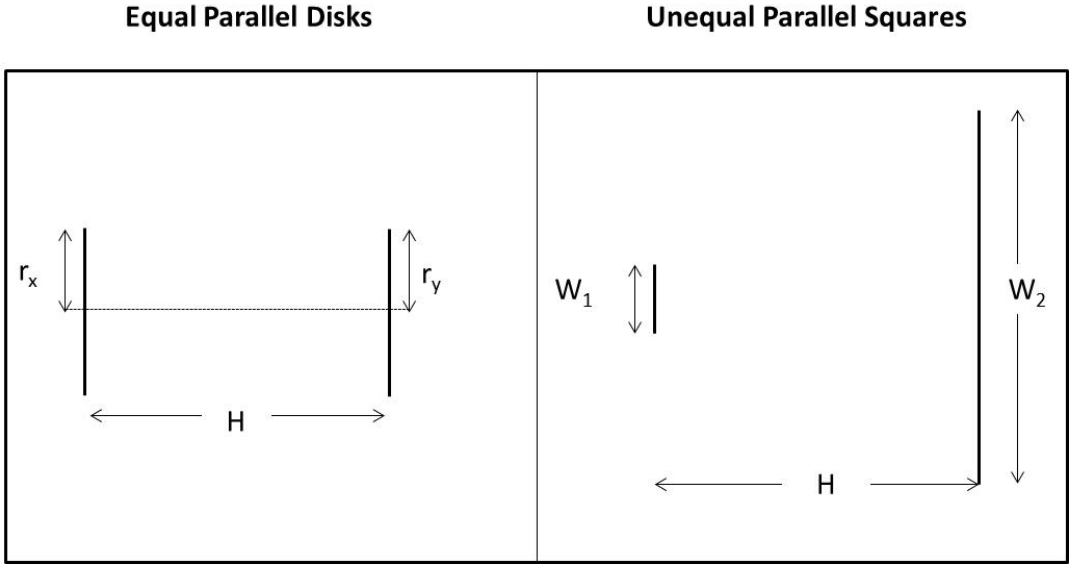

Figure D-3: Showing the geometries for the view factor calculations

$$F_{12} = \frac{2 + \left(\frac{1}{(r_x/L)^2}\right) - \sqrt{(2 + \frac{1}{(r_x/L)^2})^2 - 4}}{2}$$

Table D-1: Comparison of the results using both sets of Equations for Parallel Squares

Constants		L (m)	Differential View Factor	Finite View Factor
r_x	0.003125	**0.082**	0.001452	0.00144815
β	0	**0.078**	0.001605	0.001600000
dA	3.07E-05	**0.06**	0.002713	0.002698055

This simplification shown by Equation above also works to a certain extent for the view factor, used in *6.2.5 Preliminary Experiment*, where two parallel squares of different sizes were used to represent the thermocouple and the furnace.

The finite view factor in this case can be described using the following set of Equations [119]:

$$w_1 = \frac{W_1}{L}\ ; \qquad w_2 = \frac{W_2}{L}$$

$$x = w_2 - w_1; \quad y = w_2 + w_1$$

$$u = \sqrt{x^2 + 4}\,; \quad v = \sqrt{y^2 + 4}$$

$$q = (x^2 + 2)(y^2 + 2); \quad P = ({w_1}^2 + {w_2}^2 + 2)^2$$

$$S = u\left(xtan^{-1}\left(\frac{x}{u}\right)\right) - \left(ytan^{-1}\left(\frac{y}{u}\right)\right); \qquad t = v\left(xtan^{-1}\left(\frac{x}{v}\right)\right) - \left(ytan^{-1}\left(\frac{y}{v}\right)\right)$$

$$F_{12} = \left(\frac{1}{\pi {w_1}^2}\right)\left(\ln\left(\frac{p}{q}\right) + S - t\right)$$

Table D-2: Comparison of the results using both sets of Equations for Parallel Disks

Constants		L (m)	Differential View Factor	Finite View Factor
rx	0.1525	**0.5**	0.029611	0.028720097
β	0	**0.37**	0.054074	0.050401969
dA	0.023256	**0.46**	0.034984	0.032643275

The difference between the results from the differential and finite Equations is more noticeable for the furnace view factor than for the disks. This is due to the area of the furnace being larger, making the approximation of a differential area less accurate.

Appendix E

In order to formulate the Equations to calculate the distance seen by the target in the tube three situations were examined. For each set-up the distances D1, Dt and D2 remained the same. i.e. the target was always at the same distance down the tube, had the same diameter and was the same distance from the plume respectively.

For the first set-up the point of interest is at the outermost edge of the target, as shown by the blue circle in Figure E-1 below. The red lines represent the edges of the area seen by the target from that point. From this point in the target, one line can only see straight down the tube, however the furthermost side can see out of the tube at angle represented by α. X1 and DA represent the extra distance seen beyond the edge of the tube and the total distance seen by the point out of the tube respectively.

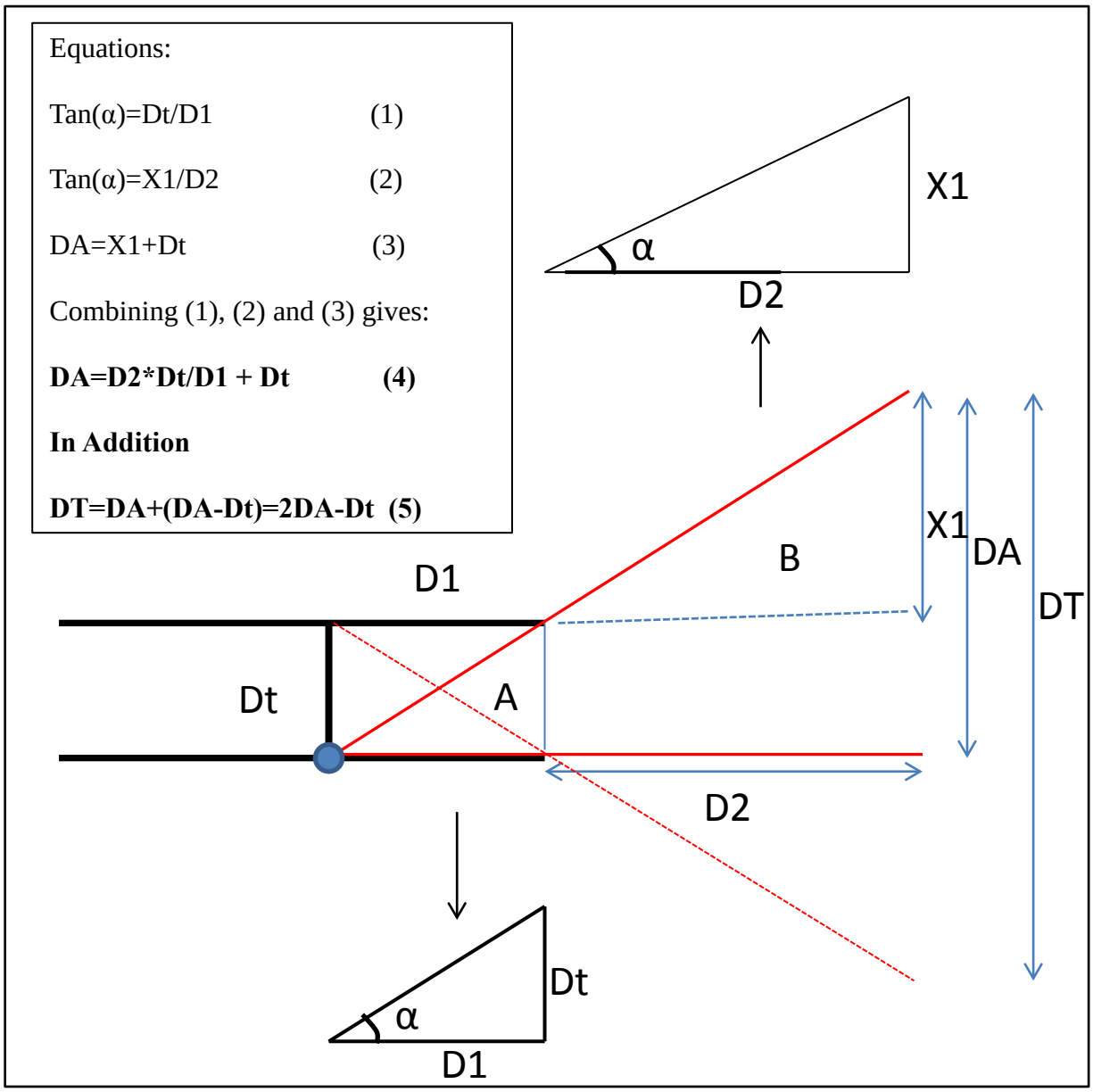

Figure E-1: Diagram showing the view of an edge point on the target to the plume and the corresponding Equations

The second set-up looks at how the Equations would look if the point on the target was moved to the centre of the target in stead of at the edge. In this case both red lines are at the same angle to the horzinatal and therefore 'see' the same distance out of the tube. From this it is shown that the same Equation can be used to describe both situations.

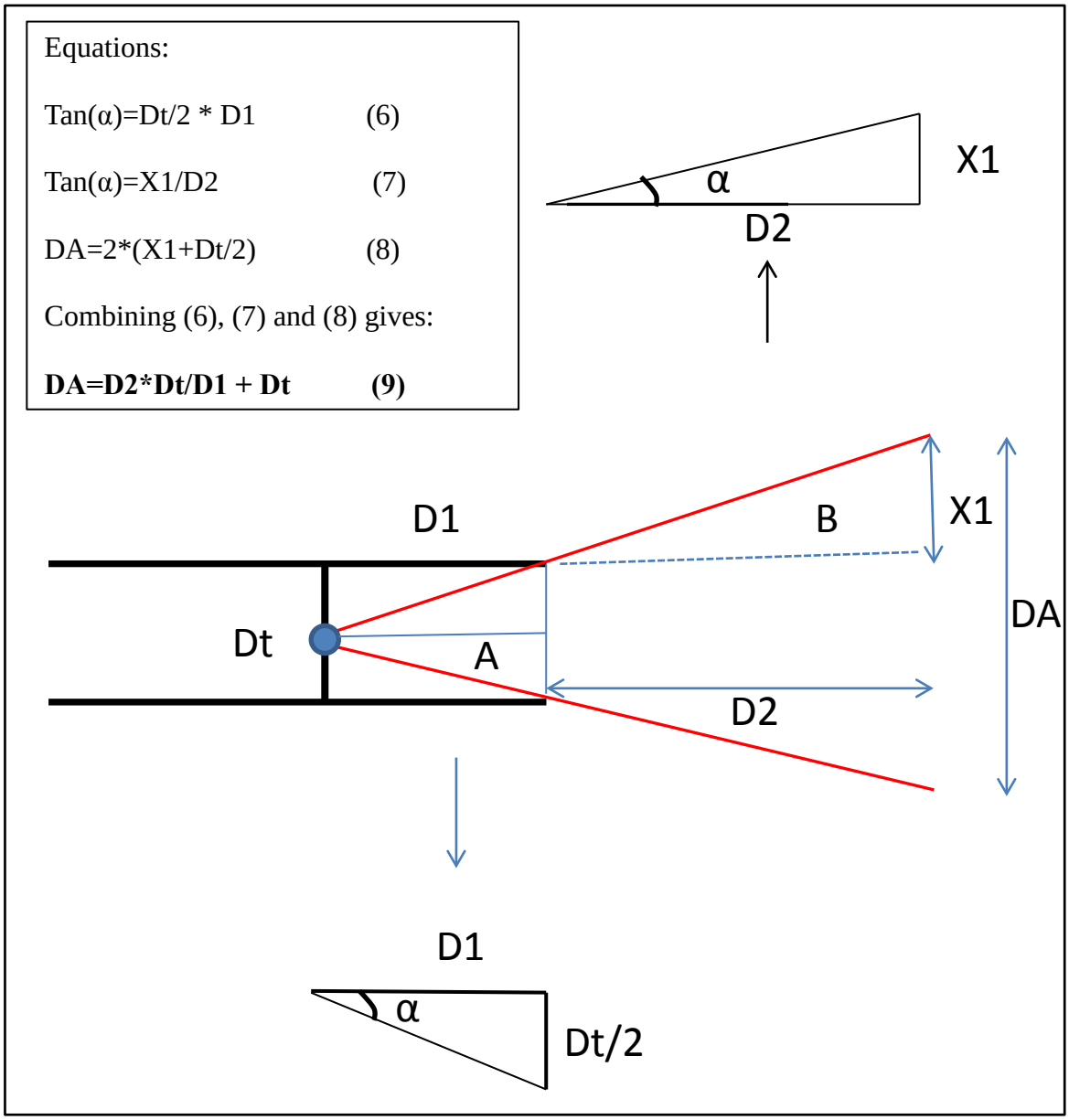

Figure E-2: Diagram showing the view of a central point on the target to the plume and the corresponding Equations

The Final Set-up looks at a more general case in which the point in the target is'x' distance from the of the tube and y distance from the bottom of the tube, where x and y are ratios of Dt and summate to unity.

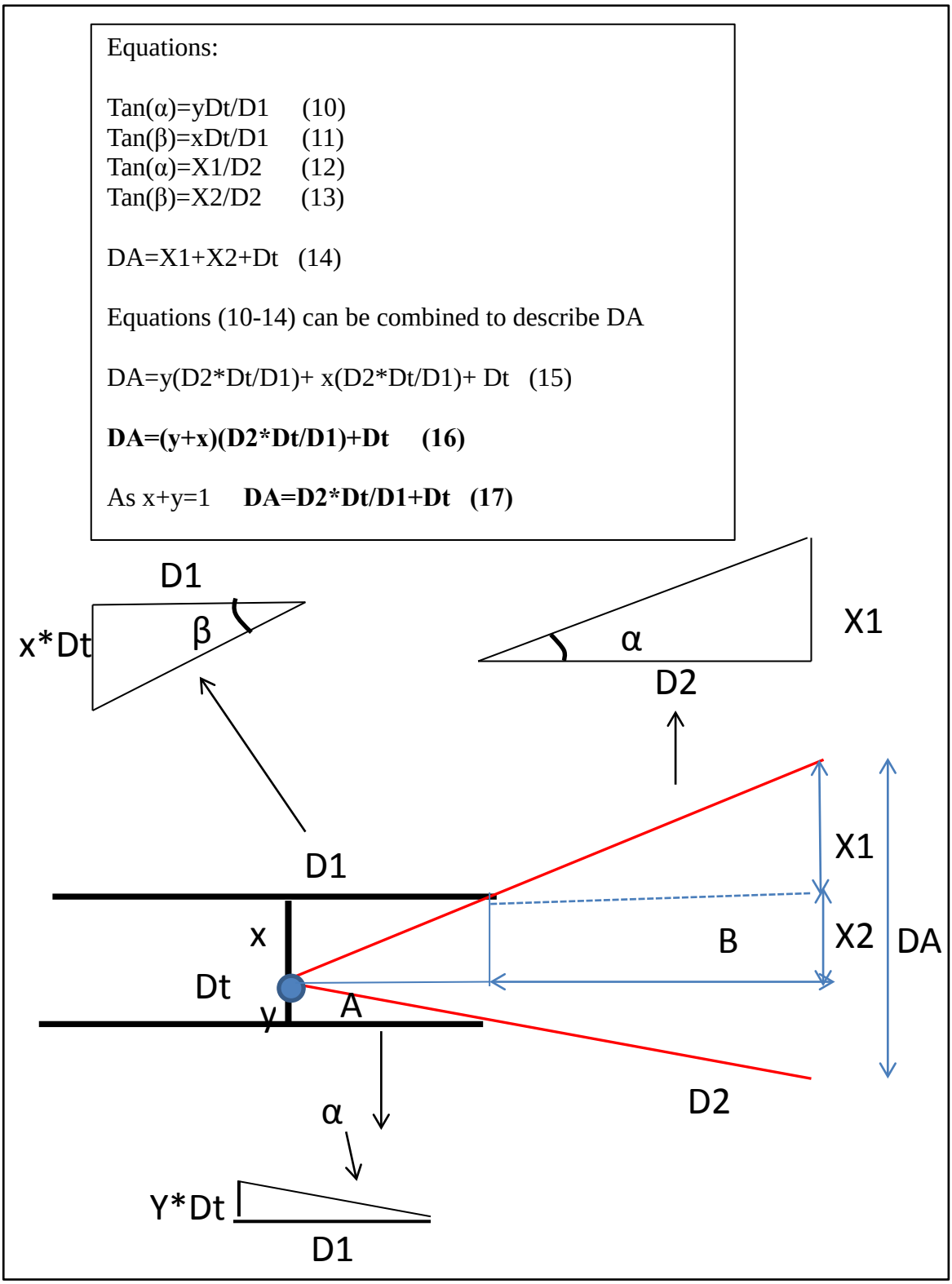

Figure E-3: Diagram showing the view of a random point on the target to the plume and the corresponding Equations